UNIVERSITÀ DEGLI STUDI DI TRIESTE

XXX CICLO DEL DOTTORATO DI RICERCA IN
Earth Science and Fluid Mechanics

LARGE EDDY SIMULATIONS OF
GRAVITY CURRENTS
OVER ERODIBLE BEDS

Settore scientifico-disciplinare: ICAR/01

Ph.D. Student	**Foteini Kyrousi**
Ph.D. Coordinator	**Prof. Pierpaolo Omari**
Thesis Supervisor	**Prof. Vincenzo Armenio**
External Advisor	**Dr. Francesca Zanello**
External Advisor	**Dr. Luca Falcomer**

ANNO ACCADEMICO 2016/2017

Author: Foteini Kyrousi

e-mail: kyrousifo@gmail.com

Affiliation: Doctoral School in
"Earth Science and Fluid Mechanics".

Dipartimento di Ingegneria e Architettura,
University of Trieste, Piazzale Europa 1,
I-34127 Trieste, Italy

Supervisor: Prof. Vincenzo Armenio

e-mail: armenio@dica.units.it

Affiliation: Dipartimento di Ingegneria e Architettura,
University of Trieste, Piazzale Europa 1,
I-34127 Trieste, Italy

External advisor: Dr. Francesca Zanello

e-mail: zanello@idrostudi.it

Affiliation: Idrostudi S.r.l., Loc. Padriciano,
I-34149 Trieste, Italy

External advisor: Dr. Luca Falcomer

e-mail: falcomer@idrostudi.it

Affiliation: Idrostudi S.r.l., Loc. Padriciano,
I-34149 Trieste, Italy

To my familly and my friends without whom none of my success would be possible.

"As a young man, my fondest dream was to become a geographer. However while working in the customs office I thought deeply about the matter and concluded it was far too difficult a subject. With some reluctance, I then turned to Physics as a substitute."

- Albert Einstein (Unpublished Letters)

Acknowledgements

to continue. Of course, I could not forget Santiago. I feel very lucky that coming to Trieste I had the opportunity to meet him. I would like to thank him for the nice moments that we shared during this period in Trieste, his support all these years that helped me to keep fighting and of course for his patient, especially the last period of the PhD (era una verdadera locura...).

Finally, I am particularly thankful to my family: my mother, my father, my sister and everyone else that make parts of it, for their love and care. They are always present in any step of my life and I would never arrived here without their help.

Trieste, 23 March 2018
Foteini Kyrousi

Abstract

Gravity currents are essentially horizontal flows driven by a density difference with respect to the ambient fluid. Such flows can trigger the transport of large amounts of sediment resulting in rapid deformations on the bed of rivers and reservoirs, causing important environmental issues. Despite the importance of such phenomena, the main mechanisms that lead to sediment entrainment in such flows are still poorly understood.

In this thesis a coupled hydro-morphodynamic model is presented in order to simulate sediment transport processes induced by the propagation of gravity currents over erodible-beds. The hydrodynamics of the flow is resolved using the LES-COAST model, that is based on the large eddy simulation method, and the topological changes due to erosion and deposition are tracked by the level-set method. The coupling between the two models is achieved through the immersed boundary methodology. The resulting hydro-moprhodynamic tool works in parallel environment that makes the simulation of real systems possible. This model is applied to the simulation of the ripple migration problem in order to test its capabilities. The obtained results are compared with data provided by a similar numerical study and indicate that the model is able to capture correctly the hydrodynamics of the sediment-laden flow and the related topological changes.

The focus of this work is on the sediment transport induced by Boussinesq compositional gravity-currents with high Grashof number. The geometric configuration used corresponds to the case of a lock exchange flow in an infinite channel in which part of the bottom boundary is considered mobile.Two different study cases have been studied, one with stationary boundaries and one with moving boundaries. In the first study case the sediment pick-up induced by gravity currents is simulated assuming stationary flow boundaries and the numerical results are validated by experimental data. The numerical setting considered in this case allows to identify the region of the flow with higher erosive capacity and determine the flow features which play a dominant role on the sediment entrainment. Moreover, the effect of the suspended sediment on the stability condition of the gravity current is examined, along with the influence of the latest on the suspended sediment distribution.

Finally, the developed hydro-morphodynamic model is used to simulate

the bed forms generated by such flows. It is worth-noting that the propagation of highly erosive gravity currents over loose beds can lead to considerable bed deformation that significantly influence the flow dynamics. For the first time, 3D numerical simulations of gravity currents flowing over a deformable beds are performed. The instantaneous evolution of the generated scour and deposition patterns is presented, providing a better insight on the flow-sediment and flow-bed interaction in buoyancy driven flows hence contributing to improve the understanding of this physical phenomenon, so relevant at real scale applications.

Sommario

Le correnti di gravità sono flussi prevalentemente orizzontali causati da variazioni di densità rispetto al fluido circostante. Tali flussi possono scatenare il trasporto di notevoli volumi di sedimenti provocando così rapide deformazioni del letto dei corsi d'acqua e dei bacini causando importanti problemi di natura ambientale. Nonostante la rilevanza di tale fenomeno, non è ancora ben compreso il meccanismo che causa la ri-sospensione dei sedimenti.

Un nuovo modello idro-morfodinamico viene presentato nel presente lavoro di Tesi al fine di simulare i processi di trasporto dei sedimenti indotti dalla propagazione delle correnti di gravità su fondo mobile. L'idrodinamica del flusso è risolta mediante il modello LES-COAST, che utilizza il metodo Large-eddy mentre i cambiamenti morfologici causati dall'erosione e dalla deposizione sono simulati mediante il modello level-set. L'accoppiamento dei due strumenti modellistici è realizzato attraverso la strategia dei confini immersi. Il modello numerico accoppiato è stato sviluppato in ambiente parallelo, che consente di simulare problemi a scala reale. Il modello è stato applicato alla simulazione della migrazione delle forme di fondo al fine di valutarne le capacità. I risultati ottenuti sono stati confrontati con i dati esito di un analogo studio numerico ed è emersa la capacità del modello di catturare correttamente l'idrodinamica dei flussi acqua-sedimento e i connessi mutamenti morfologici del fondo.

Questo lavoro è foccalizzato sul trasporto di sedimenti indotto dalle correnti di gravità composizionale mediante l'ipotesi di Boussinesq con un alto numero di Grashof. La configurazione geometrica utilizzata corrisponde al caso di un flusso di *lock-exchange* in un canale infinito in cui parte del fondo è considerato mobile. Sono stati studiati due casi diversi, uno con confini fissi e l'altro con confini mobili. Nel primo caso di studio, la sospensione di sedimenti indotta dalle correnti di gravità viene simulato assumendo confini di flusso stazionari e i risultati numerici sono convalidati da dati sperimentali. Le impostazioni numeriche adottate in questo caso permettono di indentificare la regione del flusso con maggiore capacità erosiva e determinare le condizioni del flusso che dominano la dinamica della sospensione dei sedimenti. Inoltre, è stato approfondito l'effetto dei sedimenti sospesi sulla condizione di stabilità della corrente di gravità nonché l'influenza di tale condizione sulla distribuzione dei sedimenti sospesi.

Infine, il modello accoppiato idro-morfodinamico è utilizzato per simulare le forme di fondo generate da tale tipologia di correnti. È importante notare che la propagazione di correnti di gravità con elevato potere erosivo su fondi mobili può causare notevoli deformazioni del letto che a loro volta possono avere un effetto non trascurabile sulla dinamica del flusso. La parte finale della tesi è dedicata all' illustrazione degli esiti delle simulazioni numeriche 3D delle correnti di gravità che interessano letti deformabili, approccio mai presentato sino ad ora nella letterature di settore. L'evoluzione istantanea dei pattern di erosione e deposizione sono quindi presentati, fornendo così una conoscenza più dettagliata dell'interazione flusso-sedimenti e flusso-fondo in correnti di gravità e contribuendo a migliorare la comprensione di questo fenomeno fisico, così rilevante nelle applicazioni su scala reale.

List of Publications

Most of the results preseted in this thesis have been publiced in peer-reviewed journals, or in conference proceedings. These documents are listed below.

► **F. Kyrousi**, A. Leonardi, F. Zanello and V. Armenio, "Efficient Coupling between a Turbulent Flow and Mobile Bed by Means of the Level-Set Method and Immersed Boundaries.", in *The 26th International Ocean and Polar Engineering Conference. International Society of Offshore and Polar Engineers*, Rhodes, Greece, 2016

► **F. Kyrousi**, A. Leonardi, F. Zanello and V. Armenio, "Coupling of large eddy simulations with the level-set method for flow with moving boundaries.", in *River Sedimentation: Proceedings of the 13th International Symposium on River Sedimentation, ISRS*, Stuttgart, Germany, pp. 267, 2016

► **F. Kyrousi**, A. Leonardi, C. Juez, J. Zordan, F. Zanello, F. Roman, V. Armenio and M.J. Franca, "Numerical simulations of sediment entrainment by lock-exchange gravity currents.", in *XXXVII International Association for Hydro-Environmental Engineering and Research World Congress, IAHR*, Kuala Lumpur, Malaysia, 2017

► **F. Kyrousi**, A. Leonardi, F. Roman, V. Armenio, F. Zanello, J. Zordan, C. Juez and L. Falcomer, "Large eddy simulations of sediment entrainment induced by a lock-exchange gravity current", *Advances in Water Resources, 114, 102-118*, 2018

Contents

List of Figures

List of Tables

Introduction

Overview and motivation

The present research finds its motivation in the need for efficient prediction and modeling of sediment transport. Sediment transport is a ubiquitous phenomenon in nature and industry, which plays a vital role on Earth shaping and on the development of water and soil resources. Since the beginning of the mankind's history, man has studied the water motion in rivers or canals and had a notion of the importance of the particles movement in the flow. However, sediment transport became a science itself at the beginning of the previous century [40] and since then, it has concerned many scientists, civil and environmental engineers.

Figure 1: Floodwaters laden with suspended sediment during the peak discharge of Hurricane Isabel flood on the Potomac River at Great Falls, Virginia, September 2003. Credit: Paul Bierman, UVM

The main processes of sediment transport include erosion, transport and sedimentation of particles and in fluvial, estuarine, and coastal areas are able to produce new land or enhance existing one, providing both problems

and opportunities. For instance, the morphological changes, induced by the transport of sediment in those areas, are closely related to the amplification of floods and other inundation hazards (see Fig. 1). Moreover, sediment transport can pose serious problems, and is one of the main challenges that engineers have to face during the construction of hydraulic infrastructure [97]. A typical example is bridge scouring, the removal of sediments from around bridge abutments and piers, which is considered one of the main cause of bridge failure in USA and in Europe [107]. For instance, the consequences of this phenomenon led to the dramatic event of Schoharie Creek bridge collapse, on April 5, 1987. The collapse was caused by scouring beneath a concrete pier footing [135] and led to the death of ten people. Another well known engineering problem is the accumulation of sediments upstream of reservoirs which can reduce their storage capacity and affect the turbines and the mechanical equipment [119]. On the other hand, from an environmental engineering perspective, the infrastructures can cause sediment starvation downstream, with important consequences on plant and animal species [150].

In addition to the aforementioned examples, sediment transport plays also an important role in many other fields. Geologists are interested in such phenomena to understand the processes that shape the landscapes and lead to the creation of specific types of earth formations [5]. The Gran Canyon in USA constitutes a characteristic example of the impressive features that can be created by water erosion. The deposition of sediment in navigation channels leads to the necessity of frequent dredging operations, with great economical and environmental cost [1]. Furthermore, sediment transport influences the dispersal of contaminants induced by industrial activity [74], which in turn effect the quality of water, making it unsuitable for human consumption or industrial use. In fact, there is a big amount of public investment made every year on water treatment. Agricultural activities are also significantly affected by sediment transport. The erosion of the top soil, and the loss of nutrients and organic matter leads to the decrease of soil fertility, which has to be replaced by fertilizers, a considerable cost for the farmers. Such impacts have raised the awareness towards the topic, which in turns triggered a huge practical and scientific interest over the past decades.

Despite its importance and the wide range of studies dedicated to this problem, many sediment transport and bed morphodynamic phenomena are not yet completely understood. This is due to the fact that sediment transport is essentially two-phase flow that involves a fluid phase (water or air) and a solid phase (sediment). Furthermore, the particles that constitute the solid phase are not homogeneous with regard to their shape and size. This in-homogeneity plays an important role on particle packing and on the forces acting on them. Finally, sediment motion is characterized by geometric complexity and morphological changes due to erosion and deposition

processes.

So far, our main understanding on sediment transport is based on laboratory and field studies which are subjected to important limitations. It has been demonstrated that the particle motion is highly related to flow features developed in the viscous sub-layer [88, 73] and on forces exerted on the surface of the particles. These areas are usually restricted to small length scales, which are almost impossible to resolve with measurement instruments. Moreover, performing sediment transport experiments can be challenging as the particles can interfere with the measurement devices. To overcome the aforementioned limitations several numerical models have been developed to study sediment transport applications. The main advantage of such models lies in their ability to provide a detailed flow description over the whole domain even in the viscous sublayer of the flow. Nevertheless, it is known that, for what concerns the representation of the fluid flow, the Navier-Stokes and the continuity equations constitute a general accepted mathematical model. However, there is no comparable model that can describe adequately the flow-sediment and sediment-sediment interaction, the sediment pick-up, and the bed evolution [23]. In this quest, sediment transport remains still today a challenging topic of research, and improving the understanding and modeling of sediment transport is of primary interest.

Objectives

The development of a CFD model able to reproduce accurately and effectively all the physics involved in sediment transport processes is particularly challenging. The first attempts in this direction, during the 1990s, are based on the depth integrated approach combined with a simple equilibrium sediment transport formula [147]. The results obtained by such approaches are only valid in applications where the true local sediment transport is not so different than the local equilibrium transport. The increase of computational power, over the past years, has led to the development of more and more sophisticated models, able to reproduce the unstable three-dimensional flow velocities and sediment concentration. However, the range of application of those models is extremely diverse and depends on the level of details and the scales that is aimed to solve as well as on the questions that need to be addressed.

As mentioned above, the sediment-laden flows consists of a fluid and a solid phase. The most commonly used numerical approaches that can be employed to simulate the fluid phase, ordered by decreasing computational cost, are: (1) The Direct Numerical Simulations models (DNS), which resolve all the relevant scales of the flow, (2) the Large Eddy Simulations models, where the scales of the flow are resolved and the isotropic scales are modeled, and (3) The Reynolds Averaged Navier-Stokes models (RANS),

which are the least expensive, but require a turbulence closure model. The solid phase can be treated based on the single-phase approach where the flow and the sediment are considered a mixture or the two-phase approach. In this work, the choice has fallen on the LES methodology combined with the single phase approach for the sediment. This choice is based on the effectiveness and the required computational cost.

The aim is to study the dynamics of sediment-laden flows and understand more in depth the flow-sediment interaction, in particular in case of buoyancy driven flows. Thus an in-house code, LES-COAST [111], has been modified so that: a) it is possible to reproduce bed material entrainment and deposition, induced by turbulent flows and b) deal with the bed deformations resulting from such processes. In this model, the transport of suspended sediments is simulated using an Euler-Euler single-phase approach, and the sediment entrainment using empirical formulas. The settling velocity of the particles is taken into account reducing the vertical velocity component in the advective term of the scalar transport equation [21]. It is worth noting that, in this work, only suspended sediment transport has been considered and the bed-load transport is neglected. The main changes made to the existing model are two. Initially, the modification of the boundary conditions applied to the transport equation to represent the fluxes due to erosion and deposition processes. Second, the implementation of the moving boundaries by means of the level-set method [93]. The level-set is a numerical approach designed to track the evolution of 2D or 3D boundaries between two different regions. This technique is coupled with the hydrodynamic model and the immersed boundary methodology, already implemented in LES-COAST, in order to reproduce flows with moving boundaries. In this model, the treatment of the moving boundaries makes an optimized use of information already presented in the level-set which makes the implementation of the moving immersed boundaries easier. The implementation of the level-set methodology has been assessed by simulating the suspended sediment transport above a ripple and the ripple migration. These results have been compared with similar studies available in literature.

The developed model is used to study the sediment entrainment and the bed forms generated by gravity currents. However, it may also be used for other sediment transport applications. In summary, the main objectives of the present work are:

▶ Investigating the main flow features that influence the bed material entrainment in buoyancy-driven flows and study in depth the flow-sediment interaction

▶ Quantifying the rate of bed material entrainment generated by the propagation of salinity currents over a mobile bed

▶ Investigation of the bed forms created by gravity currents flowing over

a mobile bed

The gravity currents studied are Boussinesq compositional gravity-currents with high Grashof number, generated by the lock-exhange configuration. Specifically, the numerical set-up consists of an infinite rectangular channel where part of the bottom boundary is considered mobile. The results presented in this thesis can be divided in two parts. The first investigates the bed material entrainment and the flow-sediment interaction in case of lock-exchange gravity currents. Specifically, the numerical results allow to study the main flow mechanisms that trigger sediment entrainment for such flows, as well as the influence of the entrained material in the stability conditions of the gravity currents. In this case, the bed deformation due to erosion and sedimentation processes is neglected and the boundary of the flow is considered stationary. The second part presents and analyzes the bed forms, due to scour and deposition processes, generated by the passage of a gravity current above a partially mobile bed. In both cases, the grain size of the sediments is considered small enough to be transported directly into suspension and the bed load is neglected.

Outline

The material in this thesis is structured as follows: Ch. 1 presents the physical phenomena studied in this thesis. The first part of the chapter is devoted to the processes of sediment transport along with a brief review of the numerical models used for their study. Then, the main characteristics of the gravity currents and the generated bed forms are described. The recent advances in this field and the main challenges with respect to the study of bed material entrainement induced by gravity currents are also presented. Ch. 2 contains the most common mathematical models used to describe sediment motion. Particular attention is given to the single-phase suspended transport and the pick-up functions used to describe the sediment exchange between the flow and the bed. Ch. 3 is devoted to the detailed description of the hydrodynamic model, LES-COAST, and the scalar equations necessary for the transport of suspended material. The morphodynamic model is described in Ch. 4. Specifically, the immersed boundary method (IBM), along with the level-set method used to track the evolution of a deformable bed and its implementation are presented. The hydro-morphodynamic coupling is also discussed. In Ch. 5 the developed hydro-morphodynamic model is assessed by simulating the suspended sediment transport above a ripple. The chapter includes an in-depth analysis of the results of the application of the model. In the last two chapters the focus is shifted to the simulation of the sediment transport processes induced by the gravity currents. Ch. 6 deals with the bed material entrainment over stationary bed and discusses the flow-sediment interaction. The numerical results are supported

by experimental data provided by the research group of Hydraulic Constructions Laboratory (LCH) in École Polytechnique Fédérale de Lausanne. The hydro-morphodynamic model is then used to simulate the bed forms generated by similar flows on erodible beds (Ch. 7). Finally, conclusions are drawn in Ch. 8 and an overview of possible further research is given.

Chapter 1

Physical phenomena

1.1 Sediment Transport

The field of sediment transport embodies the motion of two-phase flows, in which one phase is fluid and the other is solid. The fluid phase may consist of any type of fluid, however, in geophysics the main fluids considered are water and air. The solid phase consists of sediment grains. According to its size, sediment is classified into gravels, sand, silt, and clay (see Fig. 1.1).
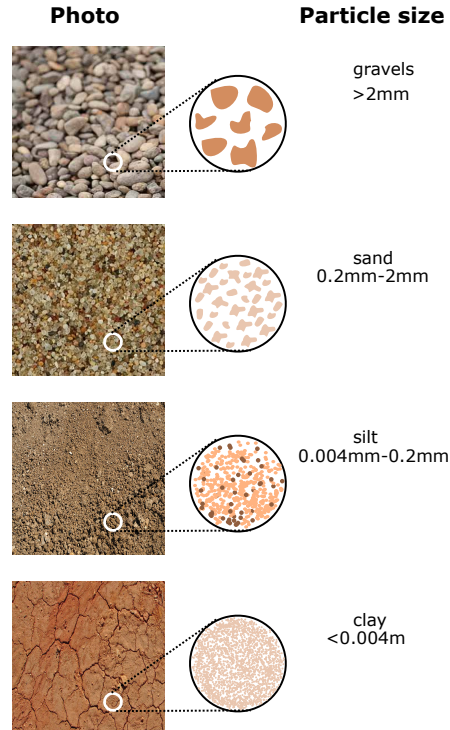
Figure 1.1: Sediment classification according to their size.
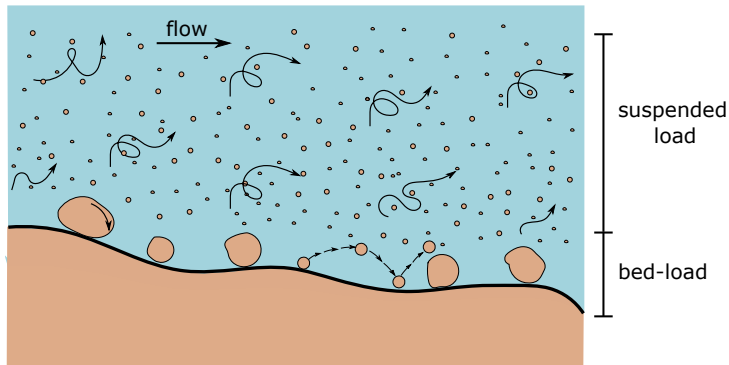
Figure 1.2: Schematic view of the different types of sediment load (bedload and suspended load) carried in a flow.

In nature, the sediment cycle includes three natural processes: 1) erosion 2) particle entrainment and transport and 3) sediment deposition [150]. Erosion is defined as the process of detachment and removal of rock particles due to the action of water, wind, or other natural agents such as avalanches, landslides. Once the particles have been detached, they can be entrained and transported by the flow, where the term "flow" alludes to the motion of water or air. Depending on the nature of the flow, sediment transport can be distinguished in fluvial transport or aeolian transport, respectively. When the flow conditions are not anymore able to transport the particles, deposition occurs [150].

Sediment transport can be divided in two different modes: suspended load and bed load transport (see Fig. 1.2). Even if there is not a clear boundary in nature between these two modes, this separation is important for the mathematical representation of the process. The mode in which the sediment will be transported depends on the particle characteristics (e.g., shape, weight) as well as on the forces exerted on them by the flow. The condition of initiation of motion corresponds to the moment when the bed shear stress exceeds a critical value and the particles start moving close to the bottom by rolling, sliding or saltation. These particles consist in the so-called bed-load. Then, if the bed shear velocity exceeds the fall velocity of the sediments, the particles can be lifted in the outer region of the flow and remain into suspension due to the upward turbulent forces [143].

Interest in sediment transport problems related to irrigations channel dates back to ancient China, Mesopotamia, Egypt, and in Roman Empire. Nonetheless, it was not until 1734 when the hydraulic engineer DuBuat (1734-1809) started studying the problem of sediment transport both analytically and experimentally and the first description of sediment particle motion was given by Hagen (1797-19884) in Germany and Dupuit (1804-1866) in France. Serious experimental studies on this field started by Engels

(1854-1945) in Germany and by Gilbert (1843-1918) in USA [148]. A significant contribution related to the initiation of motion of sediment transport was made by Shields who introduced the Shields curve for the estimation of the bed shear stress [124]. Since then, a significant amount of work have been done to understand the mechanics of sediment transport. A detailed review of the advancements in the field of sediment transport can be found in the text books of Vanoni [150], Van Rijn [148], García [32].

It is worth noting that the fundamental on sediment transport processes were established by field observations and laboratory experiments. However, the advancement of computer science in the end of 19th century made the numerical modeling of sediment transport processes in time and space increasingly common. The development of such numerical models managed to provide a better insight in the dynamics of sediment-laden flows and the flow-sediment interaction, and complement the knowledge obtained by experimental studies.

1.1.1   A review of the sediment transport numerical models

Due to the three-dimensional and time dependent nature of sediment transport phenomena, the mathematical formulations (see Ch. 2) are almost impossible to be solved analytically. Therefore, a numerical approach is necessary to reproduce sediment-laden flows. This section presents the advances of the scientific community on the numerical modeling of sediment transport, focusing on the most widely used computational models. Along the years, many sediment transport models have been developed. A comprehensive review of the various sediment transport models can be found in [32]. The numerical models can be classified according to different criteria as:

- ▶ suspended load versus bed load

- ▶ one-dimensional, two-dimension or three-dimensional models

- ▶ steady versus unsteady models.

The first sediment transport models which have been developed since early 1980s are 1D models formulated, except of some exceptions, in rectilinear coordinates. These models solve the conservation equations of mass, momentum (or energy) for the fluid, along with the advection-diffusion equation for the suspended sediment concentration. The majority of 1D models are able to predict the bulk velocity of the flow, the fluid surface elevation, the bed deformation, and the sediment transport load [98]. Representative examples of such models are HEC-6 by Thomas and Prashum [137], SEDICOUP by Holly and Rahuel [50], and 3STI1D by Papanicolaou et al. [96].

After a decade, another approach has been developed applying the depth averaged Navier-Stokes equations along with a simple equilibrium sediment

transport formula. These 2D models are applicable for unsteady flow conditions and they can provide information about the fluid depth and the bed elevation. Moreover, they can estimate the depth-averaged streamwise and spanwise velocity, and the total sediment load. Some of the most widely used 2D models are MIKE2 [24], FAST2D [81] and DELFT-2D [154]. It is worth noting that depth-averaged models have been also combined with morphological models to reproduce non-equilibrium transport conditions [10, 131]

More recently, with the increase of computational power 3D sediment transport models have become more popular. The 3D models solve the Navier-Stokes equations along with the advection-diffusion equation for sediment transport. Such models are able to reproduce sediment transport processes in purely 3D flows. Some of the most popular 3D models used for hydraulic applications are MIKE3 [24], FAST3D [64], DELFT3D [22], and TELEMAC-3D [151]. The majority of these models use the Reynolds average Navier-Stoke (RANS) approach to solve the governing equations. The main disadvantage of this approach is the use of turbulence models for the closure of the equations, which makes them ineffective for flows characterized by complex physics and geometries [2].

The majority of the existing sediment transport models for engineering purposes treat the suspended sediment and fluid flow as a mixed fluid. The disadvantage of this approach is that it disregards the interactions between the flow and the sediments and it is valid only for low sediment concentrations [84]. The last decades several attempts have been done to represent the sediment phase not as a continuum, rather as a collection of single grains. In those models the particle motion is resolved by a Lagrangian equation [87, 27, 132, 67]. However, this approach is computationally very expensive and can be employed only in small scale problems.

This thesis employs an updated version of the LES-COAST model, a 3D Navier-Stokes solver that makes use of the large eddy simulation methodology (LES) and is able to reproduce flows with moving boundaries. Between RANS and LES, the latter is more adequate for flows characterized by complex geometry, but also more computationally demanding. A detailed description of the updated LES-COAST model is given in Chs. 3 and 4. In this model, the flow and the sediment are considered as a mixture, whereas the sediment exchange between the flow and the bed is determined by empirical formulas imposed as boundary conditions. Bed-load transport is not considered in this work. The drawback of the numerical model resides on the empirical formulas used to define the initiation of motion and the erosion and deposition rates.

1.2 Gravity currents

In the field of sediment transport rivers constitute the prototype domain. However river motion is not the only agent of sediment transport. In a geophysical sense the same sediment transport processes can be encountered in various circumstances. In near-shore regions of lakes and oceans sediment transport processes are triggered by the action of waves. Moreover, dessert sand dunes constitute a characteristic example of aeolian sediment transport. In fact, one of the main agents of sediment transport on land, in lakes, rivres, and oceans are gravity currents [58].

1.2.1 General description

Gravity currents are essentially horizontal flows driven by pressure gradients due to density variations with respect to the ambient fluid. Such differences can be created by salinity or temperature variations or due to the presence of suspended sediment. The latests may also be refereed as turbidity currents. Gravity currents can be encountered in a large variate of circumstances in environment, caused by natural or anthropological factors [128]. Sea breeze storms, oceanic overflows, avalanches or airbone snow, volcanic eruptions, and sediment-laden river outflows, constitute some of the typical examples of such flows. Moreover, gravity currents are created due to release of water with high salinity from desalination plants, accidental release of a dense gas, oil spillages, pollutant discharge in water bodies or intrusion of salt water into a mass of fresh water [128, 6].

Figure 1.3: Sediment-laden outflow of the Rhone river into the Geneve lake. (Photo Credit: Rama, 2007, via Wikimedia)

Such flows have been subject of interest of the research community due
to their ability to erode and transport sediment as well as oxygen and pollu-
tants. Specifically, gravity currents are able to travel over long distances, up
to hundreds of kilometer. Their propagation has devastating consequences
on reservoirs, emissaries and cables, and submarine infrastructures. For in-
stance, many accidents on liquid fuel containers have been recorded world-
wide where the released gases, propagating as gravity currents, caused signif-
icant damages [127]. An other example of the catastrophic nature of gravity
currents is the creation of submarine high-speed turbidity currents, caused
by the Newfoundland earthquake of November 18, 1929, that cost important
damages on twelve trans-Atlantic telegraph cables in about 28 places [114].

Gravity currents are very complex and parameter-rich physical phenom-
ena that can be classified in different categories according to various cri-
teria [142]: a) constant/non constant volume, depending on whether the
initial volume of the dense fluid varies during the propagation of the current
b)Boussinesq/non Boussinesq, controlled by the initial density difference be-
tween the two fluids c)Homogeneous/stratified, with respect to the vertical
distribution of the ambient fluid density d)Gravity currents/intrusions, re-
lated to whether the currents propagates on the geometric boundaries or in-
side a stratified fluid e)two-dimensional/cylindrical geometry, f)rotating/non-
rotating frame, with respect to the vertical axes g)compositional/particle
driven, depending on whether the agent of the current is a dissolve mate-
rial, like salt and temperature, or suspended non-neutrally buoyant particles
such as sediments.

In nature there is a big variety of initiation mechanisms for the gravity
currents. However, in experimental and numerical studies the two predomi-
nant configurations are the finite initial volume and the constant discharge.
In particular, in case of the finite volume configuration, which is the one con-
sidered in this work, the lock-exchange set-up is mainly used. In this set-up,
the flume is divided into two volumes by a sliding vertical gate. One volume
contains the denser fluid and the other one the lighter fluid. Both fluids
are initially at rest. When the gate is removed, differences in hydrostatic
pressure produce a dense current which moves along the lower boundary,
while a neutrally buoyant current travels in the opposite direction along the
upper boundary.

The generated gravity current can be divided in three parts, the head,
the body, and the tail [72]. The head is the forward part of the current where
3D effects and intense mixing is taking place. This region has a dominant
role on the dynamics of the current and has been subject of extensive inves-
tigation. It is also assumed to play an important role on the erosion induced
by gracity current [58]. A detailed description of the head dynamics can be
found in [129]. The propagation of the head of the current leads to two types
of instabilities. First, the shear developed in the interface between the heav-
ier and the ambient fluid overcomes the stabilizing effect of stratification,
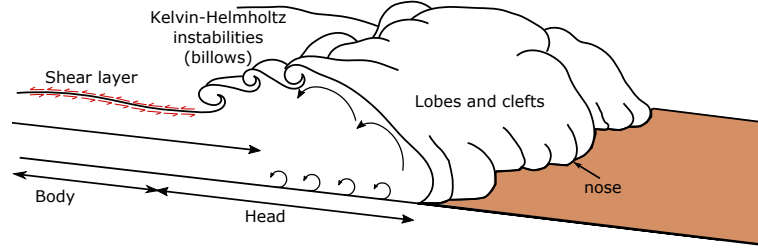
Figure 1.4: Schematic view of the shear layer between the dense and the lighter fluid. The different types of instabilities as well as the *nose* of the current are also presented

leading to Kelvin-Helmholtz instabilities (billows) [101]. These instabilities are ubiquitous in nature and are one of the major agent of mixing. Secondly, in the front part of the head, a buoyancy-induced instability is also developed, refereed as lobe and cleft [126, 128]. The foremost point of the head close to the bottom is called *nose* resulting from the non-slip condition on the boundary (see Fig. 1.4). The body of the current is separated from the head by the created billows. This part is thinner compared to the head and characterized by less dense mixed fluid and lower velocities [58]. Between the body and the tail, a further decrease in the concentration is observed and the velocity of the current are significantly reduced.

Furthermore, in unsteady gravity currents three different flow regimes can be observed during their propagation, depending on the dominant force [51]: 1) the slumping phase, where the buoyancy forces are balanced by inertia forces and the current propagates with constant velocity, 2) the self-similar phase in which the propagation of the current is still determined by the balance between the buoyancy and inertia, but the velocity of the front decreases with time ($U_f \sim t^{-1/3}$), and c) the viscous phase where the viscous effects are dominant and the velocity of the current decays faster ($U_f \sim t^{-4/5}$).

1.2.2 Literature review

The monitoring of gravity currents is a complex task due to their unpredictable nature and the difficulty of accessing the locations where these phenomena usually occur. Von Kármán [153] and Benjamin [6] were the first who dealt with the motion of gravity currents using the Bernoulli equations for an inviscid fluids. In particular, Benjamin [6] demonstrated the essential role of wave-breaking and the energy losses on the propagation of the front.

Additionally, he calculated the shape of the interface between the current and the ambient fluid. After them, there was a rapid increasing interest and a large body of literature has been created, concerning the various aspects of gravity currents. A detailed review of gravity currents in a broad rate of context can be found in [128]. In the past, the knowledge on such flows was mainly based on laboratory experiments [127, 112, 34, 45, 59, 89, 90, 95]. In the last decades, with the advent of computers, numerical studies started to gain relevance in the investigation of gravity currents. Initially, depth averaged models were used to reproduce the propagation of such flows [8, 99, 61]. However, as resulting by a detailed comparison between the results obtained with 2D and 3D simulations [85], the 2D simulations are loosing important features of the flow. In particular, Necker et al. [85] has observed that at the early stages of the gravity current propagation the 2D model can accurately predict the evolution of the flow. However, as the current advances the 2D model is not able to reproduce the kinetic energy decay due to breaking of the billows behind of the head. This limitation derives from the three-dimensional nature of the Kelvin-Helmholtz instabilities, which are not accurately resolved in the 2D simulations.

Depth resolving simulations, such as DNS and LES (see description in Ch. 3), constitute a more accurate approach to simulate the evolution of such flows. The first DNS simulation of gravity currents was performed by Härtel et al. [46] focused of the turbulent structures of the foremost part of the front of the current. Some years later, Necker et al. [86] investigated the mixing and dissipation in particle-driven gravity currents. Furthermore, Cantero et al. [11] have studied the turbulent structures and their influence on the dynamics of the flow. However, DNS models are very computational demanding and limited to gravity currents with low Grashof number. Thus, LES have recently emerged as an appropriate tool for the study of gravity currents with high Grashof number. Ooi et al. [92] has performed LES of high Grashof number compositional gravity currents with small initial volume of release. He has investigated the effect of the Grashof number on the near-bed flow structures and the bed friction velocity distribution, induced by the passage of a gravity current after the bore was formed. He also assumed that the sediment entrainment increases rising Grashof number of the current. Moreover, Gonzalez-Juez et al. [39] has investigated the influence of isolated obstacles on the structures of gravity currents, whereas Tokyay et al. [140] has studied the propagation of lock-exchange gravity currents over a periodic array of obstacles. A brief review on the recent advancements related to the LES of lock-exchange gravity currents can be found in [19].

In the literature, various studies [44, 86, 30, 90, 94] have focused on the ambient fluid entrainment on the mixing interface between the two fluids. However, the propagation of gravity currents over loose beds is closely tied to erosion and bed material entrainment [76, 92]. The turbulent flow fea-

Figure 1.5: Schematic view of the bed material entrainment induced by gravity currents

tures in the bottom boundary of the current are able to exceed the motion threshold of the bed material and transport the particles into suspension, or as bed load (see Fig. 1.5). These particles can be then deposited at long distance from its initial position leading to important topological changes. Moreover, the presence of bed material in the flow can influence the dynamics of the current by changing its density. In this respect, Parker et al. [99] has studied self-accelerating turbidity currents, Meiburg and Kneller [75] gives a detailed overview related to the deposits of turbidity currents, and Kneller and Buckee [58] provides an overview about turbidity currents from a geological prospective.

It is worth mentioning that Meiburg et al. [76] has made an interesting description of the main achievements and the remaining open questions in the field of numerical modeling of gravity currents. As he has mentioned, one of the aspects that still remains poorly understood in this field is the bed material entrainment induced by such flows. The majority of the studies which have been focused on gravity currents consider the flow dynamics over non erodible beds. Only few studies have been dedicated on the erosion induced by the gravity currents. Parker et al. [100] conducted laboratory experiments of turbidity currents flowing above an erodible bed which consists of sediment similar to that carried by the current itself. The velocity and concentration profiles were studied to evaluate the water and sediment entrainment coefficients of the governing equations. Furthermore, Blanchette et al. [7] has performed 2D numerical simulations of turbidity currents flowing down-slope over a mobile bed. He has studied the influence of the entrained bed material on the propagation velocity of the turbidity currents. Eames et al. [25] has proposed a resuspension parameter for 2D saline and particle-driven currents, based on dynamic characteristics of the currents available in literature and the knowledge on resuspension in channel flows.

Despite the aforementioned studies on the sediment exchange between the bed and the current, the main mechanisms that lead to entrainment in such flows are poorly understood. The bottom neck of the majority of the research dedicated to sediment entrainment, is that the agent of the current

is of the same nature as the bed material. Thus, it is difficult to estimate the net fluxes of entrained bed material. An acceptable alternative to overcome this problem is to represent weakly depositional turbidity currents by salinity currents, which are conservative with respect to the agent that drives the flow [20]. Garcia and Parker [34] has conducted pioneering experiments of salinity currents, flowing downslope over a mobile bed, to analyze the entrainment capacity. He observed that conservative currents with a large excess of density can entrain a large amount of bed material into suspension. Additionally, he reported an empirical relation for the entrainment of sediment in suspension, as a function of the bottom shear stress, grain size, and other parameters related with the flow dynamics and the characteristics of the bed material. However, in the best of our knowledge, there is a lack of numerical simulations related to this subject. High-resolution numerical simulations can provide an detailed space and time distribution of the velocity, bed shear stress, and of the turbulent structures formed in the flow. Moreover, they can capture the instantaneous evolution of the bed material fluxes. The combination of such information can lead to a deeper understanding concerning the flow-sediment interaction.

1.2.3   Gravity current bed forms

The study of sediment transport is directly realated to topological changes. In channel flows, particle motion triggered by the flow lead to the creation of a large variaty of structures on the river bed. The type and the size of these structures depend on the flow properties and on the sediment characteristics. Depending on the flow regime the bed forms are ussually classified into [149]:

- ▶ plane bed, ripples, and dunes in lower flow gerimws

- ▶ washed out-dunes in transitional regimes

- ▶ plane bed and antidunes in upper flow regimes

Ripples and dunes exhibit different geometrical characteristic. Specifically, the ripple height does not depent on the flow depth and is much smaller that the height of the dunes. On the other hand, the ripple length can be as large as the flow depth, whereas the dune length is much larger than the flow depth [149]. Moreover, ripples are mainly generated due to turbulent velocity fluctuations present in the vicinity of the bed interface whereas, dunes are caused by large-scale eddies [158]. The antidunes are wavy structures mainly observed in steep streams.

Despite the wide variaty of shapes all the bed forms resulting by scouring and deposition processes. In particular, bed material is scoured by the trough regions and is deposited in the crests. This process continues increasing the amplitude of the structures until the latest arrives in an equilibrium amplitude. The creation of bed structures modifies the hydraulic roughness

and depending on the size of such structures may have an important feedback on the dynamic of the flow. Specifically, it is observed that strong adverse pressure gradients are created in the lee slopes of the bed forms that lead to flow separation. As a consequence, at the downslope regions the pressure has lower values [32].

Gravity current flows with high erosive capacity can also interact with the bed material and create similar dynamic sedimentary patterns at the bed interface. Several cases have been reported in nature where large-scale bed forms have been created by gravity flows ([155, 105, 54]), having a considerable impact on morphological changes. In particular, high velocity turbidity currents are assumed to be one of the main responsibles for the submarine canyon scouring [53].

Despite the ubiquitous nature of those structures and their relevant importance few studies have investigated the bed forms induced by gravity current. Parker et al. [100] and Garcia and Parker [34] have reported bed forms created by the passage of saline and turbidity currents over a mobile bed. However, they have not evaluated their interaction with the flow field. Sequeiros et al. [122] observed the formation of bed forms due to bed-load transport induced by turbidity current. In this work, different types of bed formations are observed depending on the flow conditions and the sediment characteristic. The influence of the bed formations on the velocity and the density fields of gravity currents have been investigated in the work of Sequeiros et al. [121]. The bed forms observed in [122, 121] are presented in Fig. 1.6 and vary with the bed material characteristics. It is worth noting that these structures were recorded after the sequential action of multiple event. Furthermore, [133] have investigated the formation of wedge shape deposits associated with decelerating turbidity currents.

Apart of the aforementioned experimental studies, few numerical studies have been devoted on the investigation of the bed forms generated by gravity currents. Kubo and Nakajima [63] have employed a layer-averaged numerical model in order to investigate the sediment-wave formation of the bed induced by turbidity currents and Hoffmann et al. [49] studied the sediment wave formation induced by turbidity currents using two-dimensional direct numerical simulations. However, in the best of our knowledge there is not a numerical study that reproduce the instantaneous three dimensional bed structures generated by such flows.

In this thesis, a numerical model able to reproduce the sediment entrainment and the bed deformation due to erosion and deposition processes induced by gravity currents is presented. Specifically, the flow features that have a significant role on the bed material entrainement are identified and the generated patterns of scour and deposition are presented.
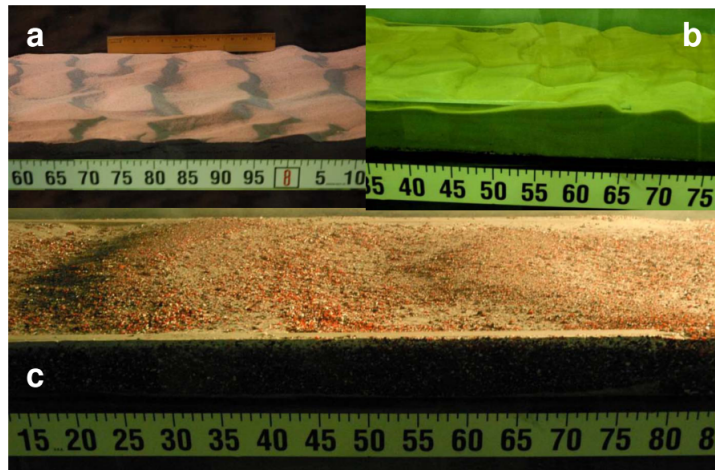
Figure 1.6: Several types of bed forms observed after the passage of gravity current over mobile beds [121].

Chapter 2

Mathematical modeling of sediment transport

Sediment transport modeling plays an important role in the understanding and prevention of many environmental problems linked to such phenomena. However, the multidimensional and multi-scale nature of sediment-laden flows makes their mathematical representation challenging. An accurate mathematical model should be able to reproduce both fluid and sediment motion as well as their interactions. Moreover, the description of the sediment exchange between the flow and the bed due to erosion and deposition processes is also required.

2.1 Rouse number

The modes of sediment transport are distinguished mathematically by the Rouse number, that expresses the ratio between the falling velocity of the particles and the shear velocity of the flow and is defined as,

$$\text{Rouse} = \frac{w_{\text{s}}}{\sigma \kappa u_*},$$

(2.1)

where w_{s} and u_* represent the settling velocity of the particles and the shear velocity of the flow, respectively. The formulation of the settling velocity and the shear velocity are shown bellow. κ is the von Karman constant [153] and σ is a coefficient that relates the sediment and momentum diffusion coefficients. The β coefficient is assumed to be equal to 1 [84]. Depending on the value of the Rouse number the mode of transport is classified as:

▶ Bed-load if Rouse > 2.5

▶ 50% suspended if 1.2 < Rouse < 2.5

▶ 100% suspended if Rouse < 1.2

19

To represent mathematically the incipient motion as well as the evolution of the two separate sediment modes different formulas are necessary. These formulas are shown in the following sections.

2.2   Initiation of motion

Before the detailed mathematical representation of the different modes of sediment transport, the concept of incipient motion should be presented. The ability of the flow to transport sediment depends on the balance of the forces acting on the particle. Those forces are the gravitational force, F_G, the drag force, F_D, and the lift force, F_L and they are presented in Fig. 2.1. When the fluid forces (F_D and F_L) exceed the gravitational force the grain starts moving. Despite the simplicity of this concept, the exact prediction of the incipient condition is a difficult task due to the sediment packing on the bed and the fluctuation over time of the fluid forces. Various efforts have been made over the years to develop a formulation that adequately estimates this threshold and a brief review can be found in [29].

If one considers the initiation of motion of a pack of particles with a certain distribution of sizes, the threshold that corresponds to incipient conditions becomes function of macroscale parameters. In literature, this threshold is mainly linked to the bed shear stress, τ_w. Shields [124] proposed a deterministic approach for the estimation of the critical condition that has proven to be the most prevailing one. In this approach the critical value of the bed shear stress τ_{cr} is given by the Shields diagram (see Fig. 2.2) and is related to the particle Reynolds number, Re_d, and to the dimensionless bed shear stress, θ. These quantities are defined as:

$$\theta = \frac{\tau_w}{[(\rho_s - \rho)gd]},$$ (2.2)

and

$$Re_p = \frac{u_* d}{\nu},$$ (2.3)

where ρ and ρ_s denotes the density of the fluid and sediment, respectively. ν is the viscosity of the fluid, g represents gravity, d is the mean particle diameter, and u_* is the shear velocity defined as:

$$u_* = \sqrt{\frac{\tau_w}{\rho}}$$ (2.4)

It is noteworthy to mention that the aforementioned graph (see Fig. 2.2) is based on bed-load experiments. Therefore, Vanoni [150] modified the Shields diagram in order to extend it to suspended sediment. More specifically, he introduced an extra dimensionless parameter V_s equal to:

$$V_s = \frac{d}{v}\sqrt{0.1sgd},$$ (2.5)
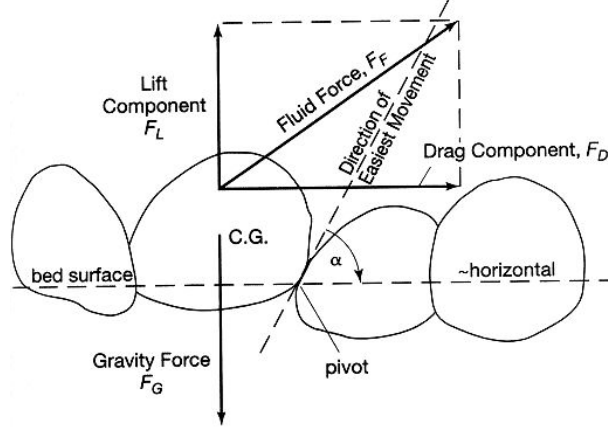
Figure 2.1: Forces exerted by the fluid on a single grain [79].

where $s = (\rho_s - \rho)/\rho$. The parameter V_s corresponds to a group of parallel inclined lines which were added to the original diagram. Each of those lines correspond to a different value of the V_s parameter. A specific flow/sediment configuration (depending on the value of V_s and Re_p) is represented by a point on one of those inclined lines. The value of the critical bed shear stress for this configuration corresponds to the intersection between this parallel line and the Shields curve. Additional, the distance of the point from the Shields curve indicates the flow potential to transfer sediment into suspension.

Moreover, the values of the critical shields parameter obtained from the diagram in Fig. 2.2 are not valid for sloped beds. In these cases the critical Shields number should be modified to take into account the influence of the local bed slope. The simplest approach to calculate the bed shear stress for an inclined bed is the one proposed by van Rijn [146], according to which the modified critical bed shear stress, $\hat{\tau}_c$, is equal to:

$$\hat{\tau_{cr}} = \tau_{cr} \frac{\sin(\beta + a)}{\sin(\beta)} \tag{2.6}$$

where a and β are the angles of the local bed slope and of the internal friction, respectively.

Finally, an additional disadvantage of the Shields criterion is that it has been developed within the RANS context. In other words, the Shields parameter is calculated based on the averaged quantities of the flow and does not take into account the turbulent fluctuations. To overcome this limitation, Zanke [164] proposed a model of the initiation of sediment motion that considers also the influence of turbulence. More specifically, he pointed out that the critical value should be reduced by the turbulent fluctuations of the bed shear stress as following:
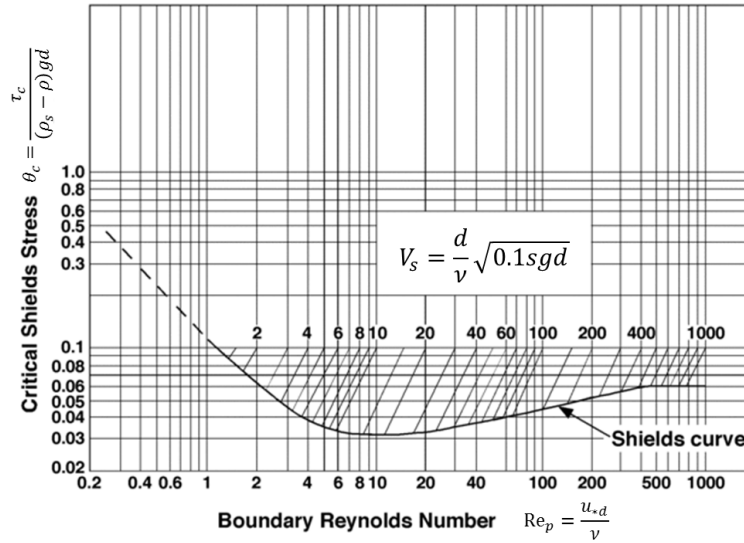
Figure 2.2: Shields diagram as modified by Vanoni [150].The inclined dashed lines represent the values of Vanoni's dimensionless parameter for each particle diameter.

$$\theta_{\text{eff}} = \theta_c - \theta', \tag{2.7}$$

where θ_{eff} is the new value of the motion threshold and θ' denotes the root mean square due to turbulent fluctuations of the wall shear stress.

2.3   Suspended sediment transport

The suspended transport is a key process in coastal and estuarine regions. One of the basic characteristics of this process is that the particle weight is counteracted by the upward diffusion due to turbulent fluxes during the entire motion. Nevertheless, when the flow conditions are not able to counteract their weight, the particle tends to settle.

2.3.1   Settling velocity

The settling or falling velocity of the sediment is one of the fundamental parameters used in the field of sediment transport. This velocity denotes the rate at which the floating particles falls in a still fluid and plays an important role on the transport of suspended sediments. Different formulas have been developed to estimate the settling velocity of suspended sediment depending on the properties of the particle (size, shape, density) and concentration. The settling velocity of a single particle in laminar flow conditions

is predicted by Stoke's law and is equal to,

$$w_{\mathrm{s},1} = \frac{(\rho_{\mathrm{s}} - \rho)gd^2}{18\mu}, \tag{2.8}$$

where μ stands for the dynamic viscosity of the fluid. However, this formulation does not hold true in case of concentrated solid suspension or in case of a bounded flows. The presence of walls as well as high suspended sediment concentration cause the decrease of the particle settling velocity due to hindering effects. By far the most popular formulation to express the hindered settling velocity is the empirical formulation proposed by Richardson and Zaki. [108],

$$\frac{w_{\mathrm{s},\mathrm{h}}}{w_{\mathrm{s},1}} = (1 - C)^{4.65}, \tag{2.9}$$

where C represents the sediment concentration. For low sediment concentration and for sediment size in the range of $100 - 1000$ μm the settling velocity can be computed using Zanke's approach [163]:

$$w_{\mathrm{s}} = \frac{10\nu}{d}[(1 + \frac{0.01sgd^3}{\nu^2})^{0.5} - 1]. \tag{2.10}$$

2.3.2   Suspended sediment models

The motion of the suspended sediment in the flow field can be treated with two different techniques: a) the Euler-Euler approach and b) the Euler-Lagrangian approach.

In the Euler-Euler approach, both sediments and fluid are treated mathematically as inter-penetrating continua [115, 70, 159, 21]. This methodology can operate on the assumption that the particles are fine enough so the inertial effect of the particles can be neglected. In the Euler-Lagrangian methodology the ambient fluid is treated as a continuum, whereas the suspended sediment is treated in a Lagrangian way. Specifically, the motion of the fluid is modeled via the Navier-Stokes equations and the motion of the suspended sediment is described by the Newton's equation of motion of each particle [87, 27, 132, 67]. The interaction between the two phases depends on the mass load of the solid phase.

Pertaining the models just described, the particle-particle interaction can be described by two different ways. In the Lagrangian description of the dispersed phase, inelastic collisions are represented via spring models, whereas, in the case the phase is treated as continuous, particle-particle interaction can be neglected [70, 68] or considered as a source term in the transport equation [159].

The behavior of the suspended sediment in a turbulent flow can be characterized by the dimensionless Stokes number (St_{k}). This number expresses the ratio between the characteristic time of the particle and the characteristic time of the flow field. The time scale of a turbulent flow is called

Kolmogorov scale and corresponds to the time scale of the smallest eddy. It is defined as:

$$\tau_{\mathrm{n}} = \left(\frac{\nu}{\epsilon}\right)^{1/2}, \tag{2.11}$$

where ϵ is the turbulent energy dissipation rate per unit mass. Depending on the size of the particles, the characteristic particle time, and respectively the Stokes number, can be defined in two different ways:

▶ if the particle diameter is smaller than the length scale of the smallest eddy (so-called Kolmogorov scale) $\eta = (\nu^3/\epsilon)^{1/4}$, the time scale of the particle is defined as:

$$\tau_{\mathrm{p}} = \frac{\rho_{\mathrm{s}}d^2}{18\rho\nu}, \tag{2.12}$$

and the Stokes number is equal to:

$$\mathrm{St}_{\mathrm{k}} = \frac{\tau_{\mathrm{p}}}{\tau_{\mathrm{n}}} = \frac{\rho_{\mathrm{s}}d^2}{10\rho\eta^2}. \tag{2.13}$$

▶ if the particle size is greater than the Kolmogorov scale, the time scale of the particle is defined as:

$$\tau_{\mathrm{p}} = \left(\frac{d^2}{\epsilon}\right)^{1/3} \tag{2.14}$$

and the Stokes number is:

$$\mathrm{St}_{\mathrm{k}} = \frac{\tau_{\mathrm{p}}}{\tau_{\mathrm{n}}} = \frac{\rho_{\mathrm{s}}}{10\rho}\left(\frac{d}{\eta}\right)^{4/3}. \tag{2.15}$$

According to the value of the Stokes number, the sediment can be divided into a) small Stokes number particles and b) large Stokes number particles [73]. In particular, sediment with Stokes number lower than 1 is considered to follow the flow closely. Under this conditions, the transport of suspended sediment can be described by the single-phase approach. On the other hand, for $\mathrm{St}_{\mathrm{k}} > 1$ the sediment detaches from the flow and the two-phase approach should do be used to described the sediment motion.

In the single-phase approach, the fluid and the sediment are considered as one continuous mixture where the suspended sediment concentration is modeled by means of the transport equation. The flow-sediment interaction can be either neglected, if the suspended sediment concentration is small enough [118], or considered as a body force in the momentum equation of the flow depending on the strength of flow stratification [130]. The particle-particle interaction is neglected in this approach. The two-phase models are based on the assumption that, each control volume contains a fraction of the comprising substances at all times. Similarly to the single-phase approach, the flow-sediment interaction is considered as a body force [42, 41].

2.3.3   Pick-up and deposition

The pick-up and deposition of sediment particles constitute an essential part of the mathematical representation of sediment transport processes. However, due to the complexity of the phenomena the mathematical representation of this process is based on empirical formulas, mainly obtained by experimental works performed in open channel flows [145]. Various studies have been focused on the pick-up of sediment transport changing the events. Here, three of the most prevalent formulas are presented.

Yalin [158] proposed that the erosion rate, E, is monotonically increasing with the shear velocity,

$$E = \alpha \rho_{\mathrm{s}} u_*, \tag{2.16}$$

while, Luque and Van Beek [71] assumes that the erosion rate is an exponential function of the sediment diameter, buoyant weight, and of the distance of the Shields parameter from its critical value,

$$E = \alpha \rho_{\mathrm{s}} (sgd)^{0.5} (\theta - \theta_{\mathrm{cr}})^{1.5}. \tag{2.17}$$

Van Rijn [145] after an extensive experimental work on open channel flows with different sediment sizes, he derived the following formula:

$$E = 0.00033 \rho_{\mathrm{s}} (sgd)^{0.5} T^{1.5} D_*^{0.3}. \tag{2.18}$$

Moreover, Van Rijn [145] in the same work concluded that the pick-up function proposed by Yalin [158] is rather poor, whereas the one proposed by Luque and Van Beek [71] provides good results for particle size $< 200 \mu$m.

The deposition rate of the suspended sediment is equal to:

$$S = w_{\mathrm{s}} C_0, \tag{2.19}$$

where C_0 represents the sediment concentration in the immediate vicinity of the sediment bed and w_{s} is the settling velocity.

2.3.4   Boundary conditions

The sediment exchange between the flow and the bed, due to the pick-up and deposition presented above, is represented mathematically by the imposed boundary conditions. The bottom boundary conditions can be classified in two categories:

▶ Dirichlet type boundary conditions, that impose the near wall sediment concentration, also called reference concentration C_{ref}, at a specific distance from the wall, z_{ref},

$$C_{\mathrm{sed}}|_{x_3 = z_{\mathrm{ref}}} = C_{\mathrm{ref}}. \tag{2.20}$$

Various empirical formulas can be found in the literature, to estimate the reference concentration and the reference level. However, the estimated reference level may not coincide with a grid point. In this case the sediment concentration can be extrapolated using the Rouse profile [113].

$$\frac{C_{\text{sed}}}{C_{\text{ref}}} = \left(\frac{h - y_1}{y_1} \cdot \frac{z_{\text{ref}}}{h - z_{\text{ref}}}\right)^{(w_{\text{s}}/\kappa u_*)}, \tag{2.21}$$

where h is the fluid depth, y_1 denotes the distance from the bed of the point that the concentration is imposed, and κ is the von Karman constant.

▶ Neumann boundary conditions, that aim to specify the net sediment fluxes at the bottom boundary. These fluxes are divided on upward fluxes (erosion, pickup) and downward fluxes (deposition).

$$\left(\kappa_{\text{sed}}\frac{\partial C_{\text{sed}}}{\partial x_2} + w_{\text{s}}C_{\text{sed}}\right) = S - \frac{E}{\rho_{\text{s}}}, \tag{2.22}$$

where S the sedimentation rate and E the erosion rate.

On the top boundary and at the lateral boundaries the most commonly used boundary condition is the Neumann zero flux condition where:

$$\left(\kappa_{\text{sed}}\frac{\partial C_{\text{sed}}}{\partial x_2} + w_{\text{s}}C_{\text{sed}}\right) = 0. \tag{2.23}$$

Reference concentration

As it was mentioned in the previous section, there are quite a few formulas to estimate the reference concentration. A comprehensive assessment of several different formulas can be found in [33]. Two of the most commonly used formulations are the one proposed by [130] and that of Van Rijn [144].

According to [130], the reference concentration is equal to:

$$C_{\text{ref}} = C_0 \frac{\gamma_0 T}{1 + \gamma_0 T} \tag{2.24}$$

where

$$T = \frac{\tau - \tau_{\text{cr}}}{\tau_{\text{cr}}}, \tag{2.25}$$

$C_0 = 0.65$ is the maximum permissible concentration, and $\gamma_0 = 2.4 \times 10^{-3}$ is a constant. In Smith and McLean [130] approach the reference concentration is calculated at a reference height which is equal to,

$$z_{\text{ref}} = \alpha_0 \frac{(\tau - \tau_{\text{cr}})}{(\rho_{\text{s}} - \rho)g} + k_{\text{s}}, \tag{2.26}$$

where α is a constant equal to 26.3 and k_s is the bed roughness.

The reference concentration in [144] is:

$$C_{\mathrm{ref}} = 0.015 \frac{d}{z_{\mathrm{ref}}} \frac{T^{1.5}}{D_*^{0.3}}, \tag{2.27}$$

where

$$D_* = d \frac{(\rho_s - \rho)g}{\nu^2}^{1/3}. \tag{2.28}$$

In this approach, the reference height is equal to the half of the bed-form height. In case that the bed-form height is not known, the reference height is assumed equal to the bed roughness.

Both aforementioned reference concentration formulations have been derived by channel flow experiments performed at small to moderated Shields parameters. However, the main difference between the two equations is the presence of the maximum concentration (C_0) at the approach proposed by Smith and McLean 197. This upper boundary of the reference concentration plays an important role for high values of Shields parameter and gives to McLean's approach [130] a theoretical advantage.

2.3.5 Sediment diffusion

After the pick-up of the bed material, particles move to the upper region of the flow due to the turbulent fluctuation of the vertical velocity component, that induces upward mixing. The averaged turbulent diffusive fluxes of the sediment can be estimated as [138]:

$$q_{\mathrm{v}} = -k_{\mathrm{sed}} \frac{\partial C}{\partial y}, \tag{2.29}$$

where k_{seds} denotes the sediment diffusivity. The sediment diffusivity is an important parameter for the suspended sediment distribution in the fluid column. This quantity is, the most of the times, related to the eddy viscosity of the fluid, ν_{t}, by the following relation [150]:

$$k_{\mathrm{sed}} = \sigma \nu_{\mathrm{t}}. \tag{2.30}$$

It should be mentioned that the eddy viscosity of the fluid represents the transfer of momentum caused by turbulent eddies. As mentioned at the beginning of this Chapter, the coefficient σ for fine sediment is usually assumed constant and equal to 1. However, in specific cases, different models have been developed that calculate σ as a function of the suspended sediment and the flow parameters. Some of those models are presented in the work of [138].

2.3.6   Stratification effects

The presence of suspended sediment in the fluid column can lead to important density variations in the vertical direction of the flow. In this case, the flow is called stratified and is considered as a) stably stratified when the density increases as depth increases or b) Unstably stratified when density decreases as depth increases. More precisely, in unstable stratified conditions, a heavier fluid is present above a lighter fluid. Thus, vertical mixing is provoked and convective motion is produced. On the other hand, stable stratification inhibits turbulent mixing and suppresses the dispersion of particles in a flow [141, 3].

In continuously stratified fluids a key parameter that defines the influence of stratification, is the gradient Richardson number Ri_g, which expresses the ratio between buoyancy and shear forces:

$$\text{Ri}_g = \frac{-\frac{g}{\rho_{\text{w}}}\frac{\partial\langle\rho\rangle}{\partial y}}{(\frac{\partial\langle u\rangle}{\partial y})^2}, \tag{2.31}$$

where $\langle\rho\rangle$ denotes the averaged density. The sediment concentration can be related to the density distribution by the following equation:

$$\rho = \rho_{\text{w}} + (\rho_{\text{s}} - \rho_{\text{w}})C, \tag{2.32}$$

where ρ_{w} stands for the reference density of the the fluid.

A critical threshold of Ri_g, usually called stability criterion, is required to defined the limit between stable and unstable conditions. Typically, this value is equal to $Ri_g = 0.25$. It should be mentioned here that stable stratification is guaranteed if $Ri_g > 0.25$, however $Ri_g < 0.25$ is not a sufficient condition to define unstable stratification.

For incompressible flows under the boussinesq approximation, the stratification effects should be taken into account as a body force term in the momentum equation (see Chapter 3). However, if Ri_g is very small, the stratification effects due to density variations can be neglected.

2.4   Bed load transport

Bed-load is the part of sediment transport that occurs in the vicinity of the bed and most of the times its rate is related to the bottom shear stress. Over the years, several deterministic and stochastic bed load rate formulas have been proposed and used. The majority of these bed-load formulas use empirical coefficients that have been calibrated according to the experimental conditions. Therefore, their applicability depends on the flow conditions and the sediment size. Two of the most common formulas are presented:

▶ The empirical formula of Meyer-Peter and Muller [78] based on a large number of experiments with a wider range of particle diameter (3-30 mm). In this approach the dimensionless bed load rate, $q*$, is computed as:

$$q* = \frac{q_{\mathrm{b}}}{\sqrt{sgd^3}} = (8(\theta - \theta_{\mathrm{cr}})^{3/2}), \qquad (2.33)$$

where q_{b} is the bed-load transport rate for flat a bed.

▶ The empirical formula developed by van Rijn [143] for particles between 0.2-2mm. In this approach the dimensionless bed load rate is:

$$q* = \frac{q_{\mathrm{b}}}{\sqrt{sgd^3}} = \frac{0.053}{d*^{0.3}}(\frac{\theta}{\theta_{\mathrm{cr}}} - 1)^{2.1}. \qquad (2.34)$$

Chapter 3

Hydrodynamic model - LES-COAST

In sediment-laden flows, as in many other physical flows in nature (such as flows at boar wakes, the smoke from an earthquake e.t.c.), turbulence is prevalent, and plays an important role in the pick-up and deposition of the sediment. An essential feature of the turbulent flows are the chaotic changes in the velocity and pressure fields, which increases their ability in transport and mixing compared to the laminar flows. In such flows, the fluid motion is governed by the nonlinear, time-dependent, and three-dimensional Navier-Stokes equations along with the continuity equation. However, due to the complexity of these equations, their solution is not an easy task apart from some simple cases. Thus, a numerical approach is necessary to reproduce turbulent flows like those that can be found when studying sediment transport processes. In this chapter, the numerical tool used in this thesis work to reproduce sediment-laden flows is described.

3.1 Numerical techniques

Turbulent flows are characterized by a large spectrum of scales (eddy size) [104] (see Fig. 3.1). The scale of the larger eddies in the flow is given by the integral scale L and the smallest eddies by the *kolmogorov* length η. The integral scale of the flow is constrained by the flow geometry, whereas the *kolmogorov* scale depends on the viscosity of the flow. These scales of motion are coherent and energy is transferred across such structures down to Kolmogorov scales, where ultimately energy is transformed into heat. Such process is known as eddy break-up [106]. In other words, the large eddies, which are unstable, break-up transferring kinetic energy to smaller eddies until this energy is dissipated by viscous motion. There are three main approaches (Direct Numerical Simulations (DNS), Large eddy simulations (LES), and Reynolds Averaged Navier-stokes (RANS)) used to numerically
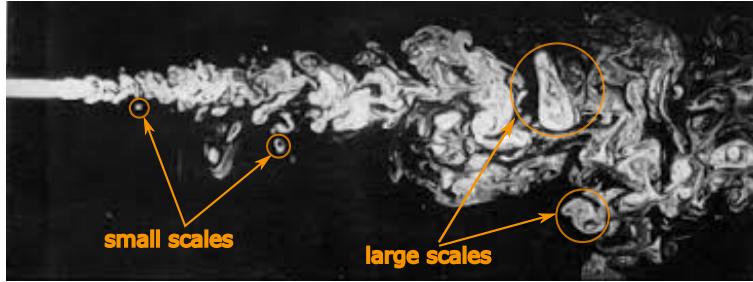
Figure 3.1: Visualization of the different scales in a turbulent flow.

confront turbulent flows. The difference between these approaches lies on the governing equations that they solve. Specifically, DNS solves the Navier-Stokes equations, the LES the filtered Navier-Stokes equations and RANS the time-averaged Navier-Stokes equations.

The most accurate numerical approach for studying turbulent flows is the DNS, which explicitly resolves all the scales of turbulence down to Kolmogorov scales. In this approach, the Navier-Stokes equations are discretized directly and solved numerically. Nevertheless, the main disadvantage of this approach is its high computational cost. In particular, in DNS, the size of the computational domain should be significally larger than the L and the required grid size has to resolve the Kolmogorov scale. Thus, the number of the grid points that are required in 1D for this type of simulations are $L/\eta \sim \text{Re}^{3/4}$, where Re is called the Reynolds number of the flow and is equal to UL/ν and η represents the Kolmogorov length scale. Indicatively, for 3D simulations the grid requirements increase with the Reynolds number as $Re^{9/4}$. Moreover, the time step of the simulations should be of the same order of magnitude of the time scales of the smallest eddy. This time scale is also propotional to the Reynolds number ($\sim \text{Re}^{1/2}$). Taking into account those restrictions, the computational cost for 3D DNS simulations increases with the Reynolds numer as Re^3 [104, 106]. Therefore, this method is impossible to use in engineering applications where the Reynolds number are usually high. However, DNS has been widely used to study sediment-laden flows at the laboratory scale [26, 12, 13, 14].

To decrease the computational cost, the RANS methodology has been developed and is the most popular methodology used in industrial computational fluid dynamics packages. This approach solves the statistically averaged equation system, and the turbulent quantities are evaluated using turbulent closure models. Thus, a relatively coarse grid and a larger time step is required for such simulations. However, the models used for the closure of the problem are based on tunable parameters and have many limitations. In the previous years, the majority of the sediment transport problems were simulated using RANS methodology. RANS provide a good
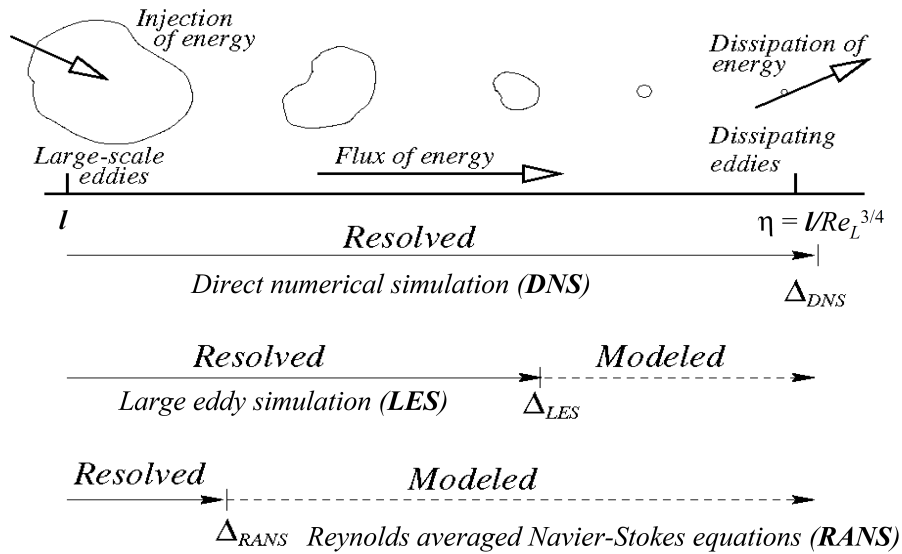
Figure 3.2: Schematic view of the differences between DNS, LES, and RANS methodologies. The figure above is from André Bakker's lectures: http://www.bakker.org/dartmouth06/engs150/10-rans.pdf

estimation of the global flow quantities such as mean streamwise velocity but is not able to predict the unsteady nature of the flow. Therefore, turbulent flows especially in case of high Reynolds number are poorly reproduced. Furthermore, RANS models suffer of important limitation in case of vortex shedding and flow seperation [109]. Finally, in case of sediment transport problems, it has been shown that RANS cannot reproduce correctly the coherent structures formed in the vicinity of the wall, which play an important role on the sediment entrainment and deposition [16].

A solution in between DNS and RANS is the LES methodology. The main difference between these three models is summarized in Fig. 3.2. LES is based on the principle that the large scales of a turbulent flow are strongly influenced by the boundary of the flow, whereas the small scales are more isotropic and do not depend on the geometry scales of the model [106]. Hence, the large scales of turbulence are resolved whereas the smaller scales are modeled using a Sub-Grid Scale model (SGS). The cutoff is determined by a low-pass filter (see Fig. 3.3). Under this assumption, LES models lead to less restrictive resolution requirments than those of DNS models and they can be used to study flows with much higher Reynolds numbers. The main differences between RANS and LES models lies on tubulent models: the LES tubulent models require fewer adjustments than the similar models for RANS [104], and are used only to model the small scales and not the entire flow. Therefore, LES is considered more accurate than RANS methodology.
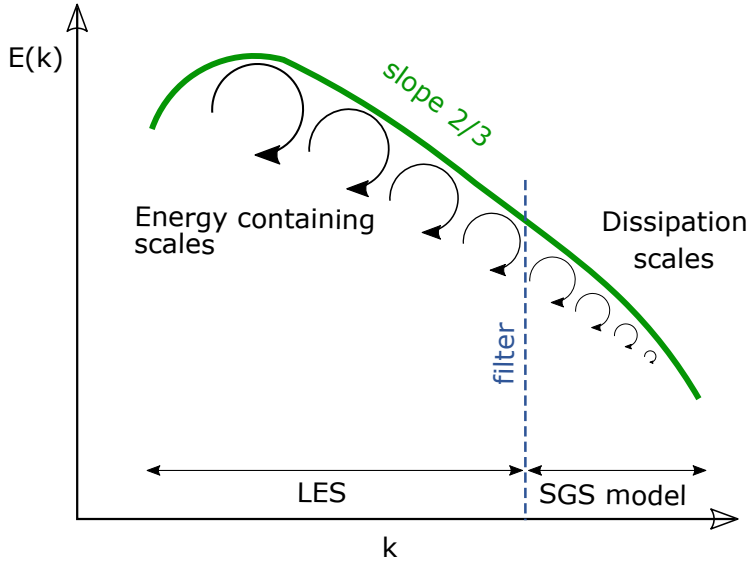
Figure 3.3: Conceptual model of the LES methodology.

Finally, the developement of new and more accurate SGS models, during the last decades, that allows the simulation of more complex configurations, has increased the popularity of the LES methodology in the Hydraulic community. In the field of sediment transport, LES numerical tools has been extensively used to study a large variaty of problems for various Reynolds numbers [18, 62, 120, 56, 21, 9].

In this thesis, the LES methodology is used to simulate sediment-laden flows. The numerical tool used is LES-COAST, an in-house code developed at the Department of Engineering and Architecture in University of Trieste. This model makes use of non-staggered grids and solves the filtered Navier-Stokes equations for incompressible flows under the Boussinesq approximation, along with the transport scalar equation. The code is written on Fortran 77/90 on parallel environment using MPI routines, and the complex geometries can be treated using curvilinear grids or the Immersed Boundary Methodology (IBM) [110]. LES-COAST has been widely used to study different industrial and environmental cases [95, 94, 162, 116]. Moreover, recently it has been applied to study sediment transport problems in channel flows over fixed beds [21]. The advancement of this thesis with respect to the work of Dallali [21] are twofold. First, the Neumman type boundary conditions (see Sec. 2.3.4) for the sediment have been implemented. These boundary conditions were tested in case of bed material entrainment induced by gravity currents; the results were validated with experimenta data and are presented in Ch. 6. Second, moving boundaries were implemented to simulate topological changes due to erosion and deposition processes. This

implementation has been assessed with respect to the work of Kraft [62].

3.2   Governing equations

In physics, the motion of compressible viscous fluids obeys the Navier-Stokes equations which in the Cartesian frame of reference are:

$$\frac{\partial \rho u_i}{\partial t} + \frac{\partial \rho u_j u_i}{\partial x_j} = -\frac{\partial p}{\partial x_i} + \rho g \delta_{i,2} + \mu \frac{\partial^2 u_i}{\partial x_j \partial x_j}, \tag{3.1}$$

where p and u_i denote the pressure and the velocity components in the x_i direction of the computational domain, ρ represents the density of the fluid, and μ is the dynamic viscosity of the fluid. The indexes i=1,2,3 correspond to the streamwise, vertical, and spanwise direction, respectively. These equations are solved along with the continuity equation:

$$\frac{\partial \rho}{\partial t} + \frac{\partial \rho u_i}{\partial x_i} = 0. \tag{3.2}$$

However, in hydraulic engineering, the considered flows are usually-considered incompressible which means that the density remains constant. Moreover, the majority of the times, the governing equations are solved under the Boussinesq approximation. The Boussinesq approximation states that, the density variations of the fluid can be considered equal to zero at all the terms of the Navier-Stokes equations apart from the buoyancy term ($\rho g \delta_{i,2}$), where the density variations are important. Thus, the buoyancy term can be written as $(\rho_w + \Delta\rho)g\delta_{i,2}$ where ρ_w is the reference density of the fluid. The simplified governing equations for incompressible fluids under the Boussinesq can be written as,

$$\frac{\partial u_i}{\partial x_i} = 0, \tag{3.3}$$

$$\frac{\partial u_i}{\partial t} + \frac{u_j u_i}{\partial x_j} = -\frac{1}{\rho_w}\frac{\partial p}{\partial x_i} + \frac{(\rho_w + \Delta\rho)}{\rho_w}g\delta_{i,2} + \nu\frac{\partial^2 u_i}{\partial x_j \partial x_j}. \tag{3.4}$$

As mentioned above, when the Boussinesq approximation holds true $\Delta\rho << \rho_w$, so in order to avoid round-off errors in the calculation of this term, the buoyancy and the pressure terms,$\partial p/\partial x_j + (\rho_w + \Delta\rho)g\delta_{i,2}$, are rearranged as $\partial P/\partial x_j + \Delta\rho g\delta_{i,2}$, where P is equal to $p + \rho_w gh$ and H stands for the flow depth. Hence, the final form of the governing equations for incompressible flows under the Boussinesq approximation is:

$$\frac{\partial u_i}{\partial t} + \frac{u_j u_i}{\partial x_j} = -\frac{1}{\rho_w}\frac{\partial P}{\partial x_i} + \frac{\Delta\rho}{\rho_w}g\delta_{i,2} + \nu\frac{\partial^2 u_i}{\partial x_j \partial x_j}. \tag{3.5}$$

In the framework of the LES methodology, the large scales of the flow are separated from the smaller scales through a filter operator. Specifically,

the turbulent variables (f) are divided in two parts, $f = \bar{f} + f'$. The $\bar{f}$ is the part related to large scales and is defined as,

$$\bar{f}(x) = \int_D f(x')G(x,x')dx', \tag{3.6}$$

where D is the domain, x is the Cartesian coordinate vector, and G is the filter function. On the other hand, f' is related to the modeled scales. The filter used in LES-COAST model is the so-called tophat filter, where

$$G(x) = \begin{cases} 1/\Delta, & \text{if } |x| < \Delta/2 \\ 0, & \text{otherwise.} \end{cases} \tag{3.7}$$

In this equation, Δ denotes the filter width. It should be mentioned that the grid spacing used in the numerical simulations is propositional to the filter width Δ. After the application of the aforementioned filter, the continuity and momentum equations for incompressible fluids under the Boussinesq approximations become:

$$\frac{\partial \bar{u}_i}{\partial x_i} = 0, \tag{3.8}$$

$$\frac{\partial \bar{u}_i}{\partial t} + \frac{\partial \bar{u}_j \partial \bar{u}_i}{\partial x_j} = -\frac{1}{\rho_w}\frac{\partial \bar{P}}{\partial x_i} + \nu \frac{\partial^2 \bar{u}_i}{\partial x_j \partial x_j} - \frac{\Delta \rho}{\rho_w}g_i\delta_{i,2} - \frac{\partial \tau_{ij}}{\partial x_j}. \tag{3.9}$$

The quantities $\bar{p}$ and $\bar{u}_i$ denote the filtered pressure, and the filtered velocity components in the x_i direction of the computational domain. In this thesis, the streamwise, vertical, and spanwise directions are also denoted by x, y, and z, respectively. Similarly, $\bar{u}_1$, $\bar{u}_2$, and $\bar{u}_3$ are referred as u, v, and w. The term τ_{ij} corresponds to the SGS scales modeled by SGS models and is described in details in the following sections.

3.3 Scalar transport

To calculate the Eulerian dispersion of scalars, in the LES-COAST model, the governing equations have been coupled with the filtered transport equation:

$$\frac{\partial \bar{M}}{\partial t} + \frac{\partial \bar{u}_j \tilde{M}}{\partial x_j} = \kappa_s \frac{\partial^2 \bar{M}}{\partial x_j \partial x_j} - \frac{\partial \lambda_j}{\partial x_j}. \tag{3.10}$$

This advection-diffusion equation can be used to simulate the transport of any scalar concentration, $\bar{M}$, and κ_s stands for the diffusivity of each scalar. The term λ_j represents the SGS scalar fluxes that will be described later. The density variations in the flow field due to the presence of scalars is considered in the filtered momentum equation by the buoyancy term (see Eq. 3.9). In environmental flows, these density variations are usually created by temperature, T and/or salinity, C_{sal} and are equal to:

$$\frac{\Delta \rho}{\rho_w} = \frac{\rho - \rho_w}{\rho_w} = \alpha_k(\bar{T} - \bar{T}_0) + \beta(\bar{C}_{sal} - \bar{C}_{sal}^1), \tag{3.11}$$

where T and $\bar{C}^1_{\text{sal}}$ are the reference temperature and salinity, respectively. Additionally, α_{k} is the coefficient of temperature expansion and β is the salinity contraction coefficient.

The scalars used in this thesis are a) salinity and b) sediment. In case that the single-phase Euler-Euler approach (see Sec. 2.3.2) is used, the transport equation for the suspended sediment concentration is written as:

$$\frac{\partial \bar{C}_{\text{sed}}}{\partial t} + \frac{\partial (\bar{u}_j - w_{\text{s}}\delta_{i,2})\bar{C}_{\text{sed}}}{\partial x_j} = \kappa_{\text{sed}}\frac{\partial^2 \bar{C}_{\text{sed}}}{\partial x_j \partial x_j} - \frac{\partial \eta_j}{\partial x_j}, \qquad (3.12)$$

where C_{sed} represents the suspended sediment concentration and, κ_{sed} is the diffusivity of sediment, presented in Sec. 2.3.5, and η_j stands for the SGS sediment fluxes. It is worth-noting that the velocity in the advection term of the Eq. 3.12 is reduced to take into account settling. Moreover, the density variations of the flow, due to suspended sediment concentration, are defined as:

$$\frac{\Delta \rho}{\rho_{\text{w}}} = \frac{\rho - \rho_{\text{w}}}{\rho_{\text{w}}} = s\tilde{C}_{\text{sed}}. \qquad (3.13)$$

3.4   SGS models

In LES methodology, the flow quantities are decomposed into a filtered (resolved) component and a residual component by a low-pass filter operation. In the filtered momentum equation the effect of the smaller scales is represented by the residual-stress tensor. The residual stress tensor is defined as,

$$\tau^R_{ij} = \overline{u_i u_j} - \bar{u}_i \bar{u}_j \qquad (3.14)$$

that includes an anisotropic and an isotropic part,

$$\tau^R_{ij} = \tau_{ij} + \frac{\delta_{ij}}{3}\tau_{kk}. \qquad (3.15)$$

The isotropic part is incorporated in the modified pressure field,

$$\bar{p} \equiv \bar{p} + \frac{\delta_{ij}}{3}\tau_{kk} \qquad (3.16)$$

while the anisotropic part is modeled, most of the times, using an eddy diffusivity model,

$$\tau_{ij} = -2\nu_{\text{t}}\bar{S}_{ij}, \qquad (3.17)$$

where ν_{t} is the eddy viscosity of the residual scales and $\bar{S}_{ij}$ the filtered rate of strain equal to,

$$\bar{S}_{ij} = \frac{1}{2}\left(\frac{\partial \bar{u}_i}{\partial x_j} + \frac{\partial \bar{u}_j}{\partial x_i}\right). \qquad (3.18)$$

Similarly to the residual-stress tensor, the residual scalar fluxes are also defined in Eq 3.10. These fluxes are modeled using the eddy-diffusivity assumption,

$$\lambda_j = \bar{u}_i \bar{T} - \overline{u_j T} = \kappa_{\text{t}} \frac{\partial \bar{T}}{\partial x_j}, \tag{3.19}$$

where κ_t is related to eddy viscosity by the SGS Schmidt number,

$$Sc_{\text{SGS}} = \frac{\nu_{\text{t}}}{\kappa_{\text{t}}}. \tag{3.20}$$

In case that Reynolds analogy holds true the Sc_{SGS} is almost unity [3].

3.4.1 Smagorinsky model

One of the simplest and most widely used eddy-viscosity models is the Smagorinsky model, where the eddy-viscosity, ν_{t}, is modeled as,

$$\nu_{\text{t}} = (C_{\text{s}} \Delta)^2 |\bar{S}|, \tag{3.21}$$

where C_{s} is the Smagorinsky constant and $|\bar{S}| = (2\bar{S}_{ij}\bar{S}_{ij})^{1/2}$ represents the contraction of strain rate tensor of the large scales. The main disadvantages of the Smagorinsky model are: a) the Smagorinksy constant is defined *a priori*, so the model is not able to represent correctly the different flow regimes and b) the Smagorinsky model appears to be very dissipative. Therefore, more elaborate SGS models have been developed. A characteristic examples constitute the Dynamic Smagorinsy [36] and the Dynamic Lagrangian model [77]. These SGS model are suited for inhomogeneous flows and are discussed in details below.

3.4.2 Dynamic models

The Dynamic Lagrangian model, proposed by Meneveau et al. [77], follows the same principles with the Dynamic model proposed by Germano et al. [36]. Specifically, in the dynamic approach the values of the Smagorinsky coefficient C_{s} are estimated locally as a function of space and time, directly from the resolved velocity field of LES. Thus, the dynamic models involve an additional test filter with width $\hat{\Delta} > \Delta$. In LES-COAST model, the test filter width is equal to $\hat{\Delta} = 2\Delta$. The residual stresses after the double filtering operation are called "subtest scale stresses" and are defined as:

$$T_{ij}^r = \widehat{\overline{u_i u_j}} - \widehat{\bar{u}}_i \widehat{\bar{u}}_j, \tag{3.22}$$

where the (ˆ) symbol denotes the test filter. Moreover, according to Germano identity [35] the resolved turbulent stresses, $\mathcal{L}_{ij}$, can be calculated as,

$$\mathcal{L}_{ij}^r = T_{ij}^r - \widehat{\tau}_{ij}^r = \widehat{\overline{u_i}\overline{u_j}} - \widehat{\bar{u}}_i \widehat{\bar{u}}_j, \tag{3.23}$$
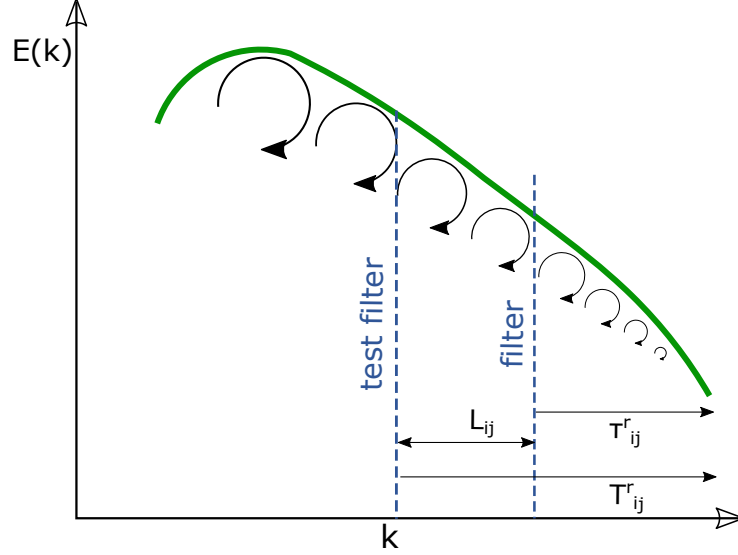
Figure 3.4: Conceptual model of the different stress tensors defined in the Dynamic Smagorinky model.

In the previous section mentioned that the anisotropic part of the residual-stress tensor can be modeled as,

$$\tau_{ij} = -2c_s\Delta^2|\overline{S}|\overline{S}_{ij}, \tag{3.24}$$

where the coefficient is now defined as c_{s} and $|\overline{S}| = (2\overline{S}_{ij}\overline{S}_{ij})^{1/2}$. In the same way, the anisotropic part of the subtest scale stresses can be defined as,

$$T_{ij} = -2c_{\mathrm{s}}\widehat{\Delta}^2\widehat{|\overline{S}|}\widehat{\overline{S}}_{ij}. \tag{3.25}$$

In these two equations, the coefficient c_{s} is considered uniform. Applying Eqs. 3.24 and 3.25 to Eq. 3.23, the anisotropic part of the resolved turbulent stresses is equal to

$$\mathcal{L}_{ij} = -2c_{\mathrm{s}}M_{ij}, \tag{3.26}$$

where

$$M_{ij} = \widehat{\Delta}^2\widehat{|\overline{S}|}\widehat{\overline{S}}_{ij} - \Delta^2\widehat{|\overline{S}|\overline{S}}_{ij} \tag{3.27}$$

Nevertheless, the above equations result in an error equivalent to

$$e_{ij} = \mathcal{L}_{ij}^r + 2c_{\mathrm{s}}M_{ij}. \tag{3.28}$$

To minimize the error, Lilly [69] proposed a least square method, where the Smagorinsky coefficient that minimizes the error is calculated to be equal

to,

$$c_{\mathrm{s}} = \frac{\left\langle \mathcal{L}_{ij}^{\mathrm{r}} M_{ij} \right\rangle}{2\left\langle M_{ij} M_{ij} \right\rangle} \qquad (3.29)$$

where the symbol $\langle \rangle$ denotes averaging.

The main difference between the dynamic and the Lagrangian dynamic model is that, the latest model calculates the required averages (see Eq. 3.29) along flow path lines instead of statistical homogeneous directions.

3.5 Scaling

To ease the definition of scales, the filtered Navier-Stokes equations presented in Sec. 3.2 can be written in dimensionless form. In this manner, the relative importance of each part of the equation becomes immediately clear. For the non-dimensionalization of the Navier-Stokes, a characteristic length, L, and a characteristic velocity, U, should to be chosen depending on the problem studied each time. Using this characteristic scales the dimensionless variables (illustrated by the symbol $(^*)$) can be defined as follow:

$$\bar{u}^* = \frac{\bar{u}}{\mathrm{U}} \qquad x^* = \frac{x}{\mathrm{L}} \qquad t^* = \frac{t\mathrm{U}}{\mathrm{L}} \qquad p^* = \frac{\bar{P}}{\rho_{\mathrm{w}}\mathrm{U}^2}$$
$$\tau^* = \frac{\tau}{\rho_{\mathrm{w}}\mathrm{U}^2} \qquad (3.30)$$

Replacing the aforementioned scaling parameters to the governing equations, the latest can written as:

$$\frac{\partial \bar{u}_i^*}{\partial t^*} + \frac{\partial \bar{u}_j^* \partial \bar{u}_i^*}{\partial x_j^*} = -\frac{\partial \bar{p}^*}{\partial x_i^*} + \frac{\nu}{\mathrm{UL}}\frac{\partial^2 \bar{u}_i^*}{\partial x_j^* \partial x_j^*} - \frac{\Delta\rho \mathrm{L}g}{\rho_{\mathrm{w}}\mathrm{U}^2}\delta_{i,2} - \frac{\partial \tau_{ij}^*}{\partial x_j^*}. \qquad (3.31)$$

In this dimensionless form of the governing equations, two dimensionless parameters appear. The Reynolds number, Re, and the bulk Richardson number, Ri, defined as:

$$\mathrm{Re} = \frac{\nu}{\mathrm{UL}} \qquad \mathrm{Ri} = \frac{\Delta\rho \mathrm{L}g}{\rho_{\mathrm{w}}\mathrm{U}^2} \qquad (3.32)$$

The relative importance of each term in the above dimensionless equations can be defined by comparing the order of magnitude of each dimensionless parameter. For instance, in flows that characterized by high values of Reynolds number the diffusivity term is becoming dominant. Furthermore, flows that have similar values of Reynolds are expected to exhibit a similar behavior. Following the same procedure for the transport equations, it is obtained:

$$\frac{\partial \bar{C}_{\mathrm{sal}}}{\partial t^*} + \frac{\partial \bar{u}_j^* \bar{C}_{\mathrm{sal}}}{\partial x_j^*} = \frac{1}{\mathrm{ReSc_s}}\frac{\partial^2 \bar{C}_{\mathrm{sal}}}{\partial x_j^* \partial x_j^*} - \frac{\partial \lambda_j^*}{\partial x_j^*}, \qquad (3.33)$$
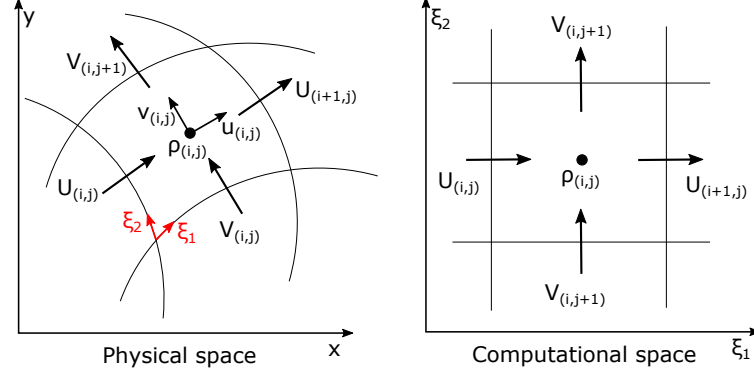
Figure 3.5: Non-staggered grid in the physical and computational domain.

$$\frac{\partial \bar{C}_{\text{sed}}}{\partial t^*} + \frac{\partial (\bar{u}_j^* - \hat{w}_{\text{s}}^* \delta_{i,2}) \bar{C}_{\text{sed}}}{\partial x_j^*} = \frac{1}{\text{ReSc}_{\text{sed}}} \frac{\partial^2 \bar{C}_{\text{sed}}}{\partial x_j^* \partial x_j^*} - \frac{\partial \eta_j^*}{\partial x_j^*}, \tag{3.34}$$

where the Schmidt numbers (Sc_{s} and Sc_{sed}) express the ratio of the viscosity of the fluid to the diffusivities of the scalars (k_{s} and k_{sed}).

3.6 Curvilinear coordinates

To reproduce complex geometries the governing equations are transformed to curvilinear coordinate system, where the discretization of the domain with curved boundaries is simpler. The resulting grid from the discretization locates the pressure, the cartesian velocity components, and the scalar quantities in the centroids, whereas the contravariant velocity fluxes are located in the cells' faces, as shown in Fig 3.5.

The governing equations (Eqs. 3.8 - 3.10), presented previously in the Cartesian frame of reference, can be transformed in the generalized curvilinear co-ordinate system by an invertible transformation. This transformation leads to the following equations:

the continuity equation,

$$\frac{\partial U_m}{\partial \xi_m} = 0, \tag{3.35}$$

the momentum equation,

$$\frac{\partial (J^{-1} \bar{u}_i)}{\partial t} + \frac{\partial (U_m \bar{u}_i)}{\partial \xi_m} = -\frac{1}{\rho_0} \frac{\partial}{\partial \xi} \Big(\frac{\partial J^{-1} \xi_m}{\partial x_i} \bar{p} \Big) + \frac{\partial}{\partial \xi_m} \Big(\nu G^{mn} \frac{\partial \bar{u}_i}{\partial \xi_n} \Big) - \frac{\Delta \rho}{\rho} J^{-1} \delta_{i,2} - \frac{\partial \tau_{ij}}{\partial \xi_m} \frac{\partial \xi_m}{\partial x_i}, \tag{3.36}$$

and the scalar transport equation,

$$\frac{\partial J^{-1}T}{\partial t} + \frac{\partial U_m T}{\partial \xi_m} = \frac{\partial}{\partial \xi_m}\Big(\kappa_s G^{mn}\frac{\partial T}{\partial \xi_m}\Big), \tag{3.37}$$

where ξ_m represents the curvilinear coordinates (ξ_1, ξ_2, ξ_3), J^{-1} is the inverse of the Jacobian that defines the volume of the cell, U_m denotes the volume flux normal to the surface of constant ξ_m, and G^{mn} is the mesh skewness tensor. These quantities are defined as,

$$J^{-1} = \det\Big(\frac{\partial x_i}{\partial \xi_j}\Big), \tag{3.38}$$

$$U_m = J^{-1}\frac{\partial \xi_m}{\partial x_j}u_j, \tag{3.39}$$

$$G^{mn} = J^{-1}\frac{\partial \xi_m}{\partial x_j}\frac{\partial \xi_n}{\partial x_j}. \tag{3.40}$$

3.7   Numerical methods

The numerical method used to resolve the governing equations is the fractional step method described in details, for curvilinear coordinates, in work of Zang [161]. The Adams-Bashforth technique is used for the time evolution of the convective terms, whereas the diffusive terms are treated implicitly with the Crank-Nicolson scheme. The space derivatives, in the curvilinear coordinate system, are discretized with a second-order centered scheme. In same cases, the advective terms of the scalar equation may discretized using a third-order accurate, upwind scheme (Quick [66]). The discretized equations are

$$\frac{\delta U_m}{\delta \xi_m} = 0, \tag{3.41}$$

$$J^{-1}\frac{\overline{u}_i^{n+1} - \overline{u}_i^n}{\Delta t} = \frac{2}{3}(C(\overline{u}_i^n) + D_\epsilon(\overline{u}_i^n) + B_i^{n-1}) - \frac{1}{2}(C(\overline{u})_i^{n-1} + D_\epsilon(\overline{u}_i^{n-1}))$$
$$+ R_i(\overline{p}^{n+1}) + \frac{1}{2}(D_I(\overline{u}_i^{n+1} + \overline{u}_i^n)), \tag{3.42}$$

$$J^{-1}\frac{\overline{T}^{n+1} - \overline{T}^n}{\Delta t} = \frac{2}{3}(C(\overline{T})^n + D_\epsilon(\overline{T}^n)) - \frac{1}{2}(C(\overline{T})^{n-1} + D_\epsilon(\overline{T}^{n-1}))$$
$$+ \frac{1}{2}(D_I(\overline{T}^{n+1} + \overline{T}^n)), \tag{3.43}$$

where $\frac{\delta}{\delta \xi_m}$ denotes the discrete finite difference operator in space and the superscripts (n, $n+1$, and $n-1$) represent the different time steps. C stands for the convective terms, D_ϵ and D_I are the explicitly treated off-diagonal diffusive terms and the implicitly treated diagonal viscous terms,

respectively, B_i stands for the body forces, and R_i denotes the operators for the pressure gradient terms. These quantities are defined as

$$C(\mu) = -\frac{\delta}{\delta\xi_m}(U_m\overline{\mu}_i), \tag{3.44}$$

$$D_I = \frac{\delta}{\delta\xi_m}\left(\nu G^{mn}\frac{\delta}{\delta\xi_n}\right) \quad m = n, \tag{3.45}$$

$$D_\epsilon = \frac{\delta}{\delta\xi_m}\left(\nu G^{mn}\frac{\delta}{\delta\xi_n}\right) \quad m \neq n, \tag{3.46}$$

$$B_i^n = -\frac{\Delta\rho^n}{\rho_{\mathrm{w}}}J^{-1}\delta_{i,2}, \tag{3.47}$$

$$R_i = -\frac{\delta}{\delta\xi_m}\left(I^{-1}\frac{\delta\xi_m}{\delta x_i}\right), \tag{3.48}$$

where μ represents each variable $(\overline{u}_i^n, \overline{T}^n)$.

3.7.1 Fractional step method

The fractional-step method, originally proposed by Chorin [17] and Teman [136], can proceed in different ways. The approach used in this thesis is the one described in work of Zang [161], where the time advancement is decomposed into parts. In the first part is called call predictor and is used to approximate the Eq. 4.25 by calculating an intermediate velocity u_i^{in} without taking into account the pressure terms in the Eq. 4.25,

$$\begin{aligned}(I - \frac{\Delta t}{2J^{-1}}D_I)(u_i^{in} - u_i^n) = \frac{\Delta t}{J^{-1}}\Big[&\frac{2}{3}(C(\overline{u}_i^n) + D_\epsilon(\overline{u_i^n} + B_i^n)\\ &- \frac{1}{2}(C(\overline{u}_i^{n-1}) + D_\epsilon(\overline{u}_i^{n-1}) + B_i^{n-1}) + D_I(\overline{u_i^n})\Big],\end{aligned} \tag{3.49}$$

where I is the identity matrix. In the second step, called corrector, the final solution of the velocity at the next time step is calculating by correcting the intermediate velocity using the pressure terms and enforcing continuity,

$$\overline{u}_i^{n+1} - u_i^{in} = \frac{\Delta t}{J^{-1}}\Big[R_i(\phi^{n+1})\Big], \tag{3.50}$$

where the variable ϕ satisfies the following equation,

$$R_i(p) = \left(J^{-1} - \frac{\Delta t}{2}D_I\right)\left(\frac{R_i(\phi)}{J^{-1}}\right). \tag{3.51}$$

Deriving the Eq. 3.50 for the contravariant fluxes U_m, the Poisson equation for pressure is obtained,

$$\frac{\partial}{\partial\xi_m}\left(G^{mn}\frac{\partial\phi^{n+1}}{\partial\xi_n}\right) = \frac{1}{\Delta t}\frac{\partial U_m^*}{\partial\xi_m}. \tag{3.52}$$

The multigrid technique is used for the solution of the Poisson equation [161].

3.7.2   Stability condition

As it has been clear in the previous sections, iterative techniques are used to solve the governing equations of the flow. However, these techniques may face stability or convergence problems depending on the different schemes that have been used. Thus, most of the times, the time step of the simulations should meet specific requirements to ensure stability.

It is noteworthy that the implicit schemes, although they are more complicated to implement, allow larger time steps compared to the explicit schemes. Thus, in LES-COAST model the viscosity stability limit can be removed since the viscous terms are solved implicitly. Nevertheless, the convective terms are treated explicitly so the time step of the simulations is restricted by the explicit stability limit known as the Courant-Friedrichs–Lewy (CFL) condition.

$$\max\{CFL\} < \hat{C}, \tag{3.53}$$

where $\hat{C}$ is a function of Reynolds number (~ 1). CFL is equal to,

$$
\begin{aligned}
CFL &= \Big(\frac{|u_1|}{\Delta x} + \frac{|u_2|}{\Delta y} + \frac{|u_3|}{\Delta z}\Big)\Delta t \\
&= (|U_1| + |U_2| + |U_3|)\frac{\Delta t}{J^{-1}},
\end{aligned}
\tag{3.54}
$$

where Δx, Δy, and Δz stand for the cartesian grid spacing in streamwise, vertical, and spanwise directions, respectively. According to this condition, the fluid particles should not travel more than one computational cell per time step.

Chapter 4

Morphodynamic model

Sediment transport problems are characterized by complex geometries and rapid morphological deformations. In the past, morphological changes were studied almost exclusively by laboratory experiments. However, thanks to the advances in computer science, in recent years it became possible to investigate the topological changes due to sediment transport also numerically. In this chapter the numerical simulation of the evolution of bottom boundaries by means of the level-set method combined with the Immersed Boundary Methodology (IBM) is discussed.

4.1   Numerical techniques for moving boundaries

The deformation of the bed can be reproduced numerically by decoupled or coupled hydro-morphodynamic models. Decoupled models calculate the flow field above stationary boundaries and then use the calculated flow quantities to evolve the bed interface independently [117]. In other words, in those models the flow field does not feel the moving boundaries. Such models are inherently incapable of simulating the interaction between the flow and the mobile bed and lead to inaccurate prediction of topological changes due to sediment transport processes. On the other hand, in coupled models the velocity field is solved simultaneously with the bed evolution [68, 57, 156, 70]. This means that, at each time step, the flow field is calculated based on the position of the boundaries at the previous time step and the calculated flow quantities are used to update the position of the boundaries. The new position of the bed is then used as boundary of the flow field at the next time step. It is worth-noting that such models require the implementation of a moving boundary technique, which increases their complexity and the computational cost.

   The most common technique used to reproduce flows over moving boundaries is the mesh deformation of the flow domain. This approach has been widely used to study the bed evolution induced by different sediment trans-

45
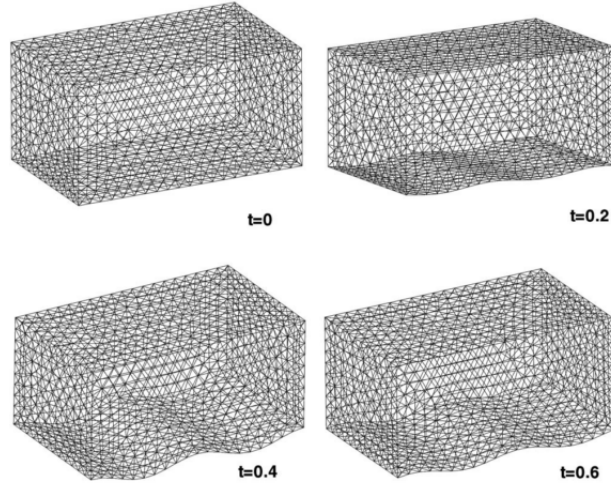
Figure 4.1: Mesh deformation of a vibrating flume bottom [70].

port problems such scouring, dune morphology, bed forms [70, 27, 139, 156]. The mesh deformation method uses body-fitted grids, which have to be dynamically deformed at each morphodynamic time step to follow the modified boundaries as shown in Fig. 4.1. Hence, re-meshing of the computational domain has to be applied every time that the bed changes shape. It is worthnoting that the applicability of this method is restricted to small local bed deformation, due to the creation of instabilities, as reported in [56, 156]. Additionally, it is characterized by immense computational cost [70].

A few years ago, Khosronejad et al. [57] proposed a new numerical method for simulating deforming beds. In this approach the flow is solved in a fixed curvilinear grid and the bed geometry is introduced as an immersed body. Furthermore, the immersed bed interface is meshed by an unstructured triangular grid. To calculate the evolution of the bed due to sediment transport the Exner–Polya equation is used and discretized on the triangular unstructured mesh of the bed interface. Specifically, at each time step the sediment flux at each grid point of the bed interface is calculated and the level of the bed grid is modified according to those fluxes. This method was used to simulate bed load transport as well as sand waves in turbulent channel flows [57, 56]. The main advantage of this method is that it does not suffer from the instabilities encountered with the mesh-deforming approach. Moreover, it should be mentioned that the complex bed geometries are easier to reproduce with the IBM than with body-fitted grids.

In our work, a relatively new method is implemented to treat the evolution of the bed surface. In this approach, the bottom boundary is also treated as an immersed body, but the evolution of the bed interface is tracked using the level-set method. The level-set method [93] is an implicit numer-

ical approach able to reproduce the propagation of 3D boundaries or 2D
interfaces, activated by an external generated velocity field. The combina-
tion of the level-set method with the IBM has the advantage that both the
flow and the bed interface are simulated on the same fixed grid. Moreover,
in this approach the numerical instabilities can be avoided due to the fact
that the boundary interface is reproduced by a smooth function.

In recent years, the level-set method has been widely used by the hy-
draulic community for the representation of the interface between two dif-
ferent phases and precisely for gas-liquid interfaces [134, 15, 52, 15, 160].
However, to the best of our knowledge, few studies have been done using
the level-set method for the representation of the bed interface. Kraft [62]
studied numerically the fully coupled problem of sediment transport in sus-
pension and the ripple migration by means of LES and the level-set method.
In this work both the flow field and the level-set are simulated in a Cartesian
grid and the position of the bed is updated at each time step. Similarly, [117]
investigated the scour and the deposition pattern around a pier using level-
set method along with a RANS model for the fluid motion. Specifically, the
level-set method is used for the representation of both free-surface and mov-
able sediment bed. However, [117] has fully decoupled flow and sediment
bed, which means that the boundaries of the flow are not updated due to
topological changes.

One of the main objective of this thesis is to present the implementation
of the level-set method for curvilinear coordinates and its combination with
the IB methodology for curvilinear grids presented in [110]. This model is
then validated with the coupled simulations of [62].In this chapter, the level-
set method and its implementation for curvilinear coordinates is described
in Sec. 4.2 along with the immersed boundary methodology in Sec. 4.3.
Additionally, in the last part of this chapter, the coupling procedure between
the hydrodynamic model and the mobile bed is presented.

4.2   Level-set method

The flow motion above a bed that consists of sediments can trigger the
transport of the bed material changing the shape of the flow boundaries.
Such changes in turn can affect the evolution of the flow. To reproduce
such phenomena numerically, a model able to capture the changes of the
geometry is necessary. In this work, the level-set method proposed by Osher
and Sethian [93] is implemented in the Navier-Stoke solver, LES-COAST,
to track the evolution of the bed. In this approach, the sediment surface is
represented by the zero level-set of an implicit function ϕ whose evolution
is calculated by the Hamilton-Jacobi equation,

$$\phi_t + V_{\text{ext}}|\nabla\phi| = 0, \tag{4.1}$$
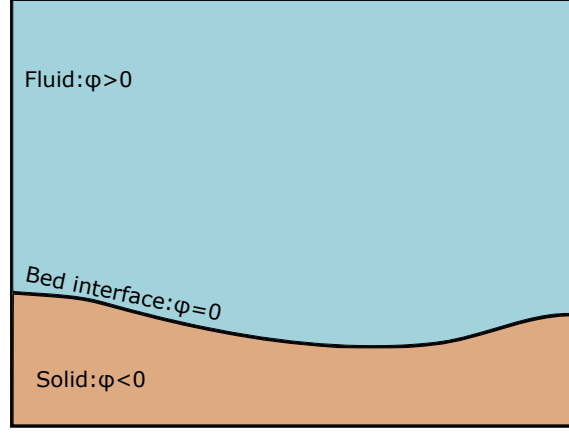
Figure 4.2: Definition of the computational domain in the concept of the level set approach, where the bed is defined as the zero level set of an implicit function ϕ.

where $\phi(\mathbf{x}, t)$ is the level set function. It is worth mentioning that the equation ϕ takes positive values in one side of the interface and negative on the other side (see Fig. 4.2). Moreover, V_{ext} represents an external generated velocity field normal to the sediments surface. This velocity field corresponds to the propagation velocity of the interface. It is obvious that, in Eq. 4.1, V_{ext} should be defined in the entire domain (Ω). However, in many practical applications this quantity is defined only on the interface (Γ). For instance, in sediment transport problems the propagation of the bed interface depends on the erosion and the sedimentation processes, present only at the vicinity of the bottom wall, and is defined as [62]:

$$V_{\text{ext}} = S(\mathbf{e}_2 \cdot \mathbf{n}) - \frac{E}{\rho_s}, \tag{4.2}$$

where $\mathbf{n}$ expresses the unit vector normal to the bed interface pointing in the fluid domain and $\mathbf{e}_2$ is the unit vector in the vertical direction. Thus, the extension of the V_{ext} from the interface to the whole domain is necessary (see Fig. 4.3). This extension is obtained based on the method of characteristics by solving the PDE [102],

$$(V_{\text{ext}})_t + S(\phi)\frac{\nabla\phi}{|\nabla\phi|} \cdot \nabla V_{\text{ext}} = 0. \tag{4.3}$$

The advantages of this approach is straight forward and easy to implement [102].

The level set equation is initially imposed to be equal to the signed
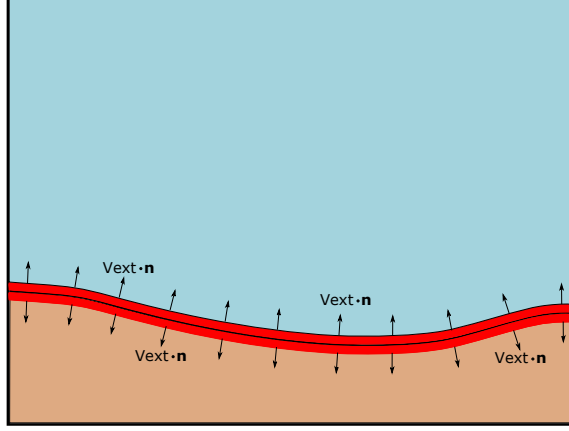
Figure 4.3: Schematic view of the extension of the external generated velocity fields that evolve the bed interface.

distance function ($|\nabla\phi| = 1$),

$$\phi = \begin{cases} +d, & \text{for } x \in \Omega_{\text{liquid}} \\ 0, & \text{for } x \in \Gamma_{\text{sed}} \\ -d, & \text{for } x \in \Omega_{\text{solid}} \end{cases}, \quad (4.4)$$

which provides the absolute minimum distance between the grid points and the bed interface. The main advantages of this representation are two. First the extension of the forces presented berofe is more accurate in case that the signed-distance function is used [123]. Secondly, the numerical approximation of the derivatives in regular grids where the grid spacing is constant is more precise if the gradient of ϕ is known and equal to $|\nabla\phi| = 1$ [38]. This choice is also beneficial for the immersed boundary methodology, as it will be shown in the next sections. However, solving the Hamilton-Jacobi equation (Eq. 4.1) is not possible to prevent the deviation of the function ϕ from the signed distance function [38]. Thus, a reinitialization procedure, activated periodically, is required during the simulations. Among the different reinitialization procedures encountered in literature, the one proposed by Sussman [134] is used in the present work. The reinitialization is operated by solving:

$$\phi_t + S(\phi_0)(|\nabla\phi| - 1) = 0, \quad (4.5)$$

where S is the smoothed sign function,

$$S(\phi_0) = \frac{\phi_0}{\sqrt{\phi_0^2 + \epsilon^2}}. \quad (4.6)$$

ϵ is a smoothing parameter with the same order of magnitude of the grid spacing and ϕ_0 is equal to $\phi(\mathbf{x}, t = 0)$. This choice is beneficial due to its simplicity and also because it is not necessary to explicitly find the zero-level set of the function ϕ.

4.2.1   Implementation of the level-set method

To reach the goal of the present work, which is the simulation of sediment transport processes, the level set formulation has to be coupled with the hydrodynamic model, which makes use of curvilinear coordinates. For this reason, the Eq. 4.1 is transformed in curvilinear coordinates as follows:

$$\frac{\partial(J^{-1}\phi)}{\partial t} + \frac{\partial(V_{\text{ext}}\phi)}{\partial \xi_m}. \tag{4.7}$$

To numerically solve the differential equations for the evolution and reinitialization of the level-set function (Eqs. 4.1 and 4.5), a forward Euler scheme is used for time discretization,

$$\phi_{i,j,k}^{n+1} = \phi_{i,j,k}^n - \Delta t \cdot R(\phi^n). \tag{4.8}$$

According to Min [80] the forward Euler scheme gives comparable results to the higher order accurate temporal descritization schemes. The forward Euler scheme is coupled with a second-order essentially non-oscillatory (ENO) scheme, for the spatial discretization in a curvilinear coordinate system. The idea of ENO schemes is to have a local adaptive stencil which obtains information from the smoothest region and avoids the discontinuities. Consequently, this method can provide high-order accuracy even in case of "shocks". This approach was presented by Harten et al. [47] for hyperbolic conservation laws and then was introduced to Hamilton-Jacobi equations by Shu [125].

The second-order derivatives in curvilinear coordinates are calculated as follows:

$$\phi_x^{(2)-} = \phi_x^{(1)-} + \frac{\Delta x^-}{2} \frac{\delta^2 \phi^-}{\delta x^2} \tag{4.9}$$

$$\phi_x^{(2)+} = \phi_x^{(1)+} + \frac{\Delta x^+}{2} \frac{\delta^2 \phi^+}{\delta x^2} \tag{4.10}$$

where $\phi_x^{(1)-}$ and $\phi_x^{(1)+}$ are calculated by a first order upwind scheme

$$\begin{aligned}
\phi_x^{(1)-} = {} & \frac{\partial \xi_1}{\partial x}(\phi_{i,j,k} - \phi_{i-1,j,k}) \\
& + \frac{\partial \xi_2}{\partial x}(\phi_{i,j,k} - \phi_{i,j-1,k}) \\
& + \frac{\partial \xi_3}{\partial x}(\phi_{i,j,k} - \phi_{i,j,k-1}),
\end{aligned} \tag{4.11}$$

$$\phi_x^{(1)+} = \frac{\partial \xi_1}{\partial x}(\phi_{i+1,j,k} - \phi_{i,j,k})$$
$$+ \frac{\partial \xi_2}{\partial x}(\phi_{i,j+1,k} - \phi_{i,j,k})$$
$$+ \frac{\partial \xi_3}{\partial x}(\phi_{i,j,k+1} - \phi_{i,j,k}), \tag{4.12}$$

and

$$\Delta x_i^- \equiv x_{i,j,k} - x_{i-1,j,k}, \Delta x_i^+ \equiv x_{i+1,j,k} - x_{i,j,k}. \tag{4.13}$$

The second-order locally-adaptive stencils are calculated as:

$$\frac{\delta^2 \phi^-}{\delta x^2} = \text{minmod}(\phi_1, \phi_2) \tag{4.14}$$

$$\frac{\delta^2 \phi^+}{\delta x^2} = \text{minmod}(\phi_2, \phi_3) \tag{4.15}$$

where ϕ_1, ϕ_2, and ϕ_3 are the central difference approximation of the operator:

$$\frac{\delta^2 \phi}{\delta x^2} \equiv \frac{\partial \xi_m \phi}{\partial x} \frac{\delta}{\delta \xi_m} \left(\frac{\partial \xi_n}{\partial x} \frac{\delta \phi}{\delta \xi_n} \right). \tag{4.16}$$

The minmod function is zero when the arguments have different sign and is equal to the argument value with minimum absolute value when they have the same sign,

$$\text{minmod}(a, b) = \begin{cases} \text{sign}(a) \min(|a|, |b|) & \text{if } a \cdot b > 0 \\ 0 & \text{otherwise} \end{cases} \tag{4.17}$$

Finally, to calculate the Hamiltonian $|\nabla \phi|$ the Godunov method is used [160],

$$|\nabla \phi| \simeq H_G(D_x^+ \phi, D_x^- \phi, D_y^+ \phi, D_y^- \phi, D_z^+ \phi, D_z^- \phi), \tag{4.18}$$

where

$$H_G(a, b, c, d, e, f) = \begin{cases} H_1 & \text{if } S(\phi) > 0 \\ H_2 & \text{if } S(\phi) < 0 \\ 0 & \text{otherwise} \end{cases} \tag{4.19}$$

and

$$H_1 = \sqrt{\max(a_+^2, b_-^2) + \max(c_+^2, d_-^2) + \max(e_+^2, f_-^2)}$$
$$H_2 = \sqrt{\max(a_-^2, b_+^2) + \max(c_-^2, d_+^2) + \max(e_-^2, f_+^2)}. \tag{4.20}$$

Note that,

$$a = \phi_x^{(2)-}, b = \phi_x^{(2)+},$$
$$c = \phi_y^{(2)-}, d = \phi_y^{(2)+},$$
$$e = \phi_z^{(2)-}, f = \phi_z^{(2)+}, \tag{4.21}$$

$$a_+ = \max(a, 0), a_- = \min(a, 0). \tag{4.22}$$

Regarding the extension of the externally-generated velocity field V_{ext} usually the accuracy of the numerical method is not an issue [102]. Thus, in this case the forward Euler time scheme is used coupled with a first-order upwind scheme for the spatial derivation,

$$V_{\text{i,j,k}}^{n+1} = V_{\text{i,j,k}}^n - \Delta t[(S(\phi_{i,j,k})n_{i,j,k}^x)^+(V_{\text{ext}})_x^{(1)-}$$
$$(S(\phi_{i,j,k})n_{i,j,k}^x)^-(V_{\text{ext}})_x^{(1)+} + (S(\phi_{i,j,k})n_{i,j,k}^y)^+(V_{\text{ext}})_y^{(1)-} +$$
$$(S(\phi_{i,j,k})n_{i,j,k}^y)^-(V_{\text{ext}})_y^{(1)+} + (S(\phi_{i,j,k})n_{i,j,k}^z)^+(V_{\text{ext}})_z^{(1)-} +$$
$$(S(\phi_{i,j,k})n_{i,j,k}^z)^-(V_{\text{ext}})_z^{(1)+}], \tag{4.23}$$

where $(x)^+ = \max(x, 0)$, $(x)^- = \min(x, 0)$. Moreover, n^x, n^y, and n^x are the components of the normal vector in streamwise, vertical, and spanwise direction, respectively. The first order derivatives, $(V_{\text{ext}})_x^{(1)-}$ and $(V_{\text{ext}})_x^{(1)+}$, are computed as $\phi_x^{(1)-}$ and $\phi_x^{(1)+}$ presented above.

Since the previous equations are advanced with an explicit scheme in time a time step condition should be applied to enforce numerical stability. Here, the chosen time step for the reinitialization equation and the extension of the forces is equal to [80]:

$$\Delta t = 0.45\min(\Delta x, \Delta y, \Delta z) \tag{4.24}$$

4.3   Immersed boundary method

The level-set approach presented in the previous sections is able to track the evolution of the bed interface. However, to set this topology as a flow boundary the IBM is necessary. The IBM is widely used in literature to simulate flows in complex geometrical domains using a structured grid. The main advantage of this method compared to body fitted approach is that the grid can remain unchanged, even for flows with moving boundaries. This feature renders the IBM a suitable tool for simulating bed deformation problems due to sediment transport.

In the IBM methodology, which was originally proposed by Peskin [103], the boundary interface is taken into account by a force field applied in the interior of the computational domain. There are two ways to calculate this force field. The first was proposed by Goldstein [37] and is called feedback forcing method. According to this approach the external force field is defined as a function of the difference between the calculated velocity at the boundary surface and the velocity of the boundary itself. The second apporach, so-called direct-forcing, was initially proposed by Mohd-Yusof [83] and applies a forcing term (f_i) at the right-hand side (RHS) of the Navier-Stokes

equations to impose the correct boundary conditions on the boundary interface. Both approaches make use of interpolation procedures to enforce the desired solution at the immersed boundaries since, most of the times, the position of the interface does not coincide with the computational grid. However, the main disadvantages of the feedback-forcing approach are that it requires the tuning of two flow-dependent constants and also that it is very restrictive with respect to the time step. LES-COAST model uses the direct-forcing immersed boundary technique, as described by Fadlun [28], and extended to non-orthogonal curvilinear grid as proposed by Roman [110]. It is worth noting that, in LES-COAST, the source/sink term on the continuity equation is neglected. It has been shown in the literature that considering the source/sink term only on the momentum equation provides satisfactory results [82]. Thus, the modified momentum equation (Eq. 4.25) in the curvilinear frame of reference can been written as:

$$
\frac{\partial (J^{-1}\overline{u}_i)}{\partial t} + \frac{\partial (U_m \overline{u}_i)}{\partial \xi_m} = -\frac{1}{\rho_0}\frac{\partial}{\partial \xi}\Big(\frac{\partial J^{-1}\xi_m}{\partial x_i}\overline{p}\Big) + \frac{\partial}{\partial \xi_m}\Big(\nu G^{mn}\frac{\partial \overline{u}_i}{\partial \xi_n}\Big) \\ - \frac{\Delta \rho}{\rho}J^{-1}\delta_{i,2} - \frac{\partial \tau_{ij}}{\partial \xi_m}\frac{\partial \xi_m}{\partial x_i} + J^{-1}f_i.
$$

(4.25)

Furthermore, the immersed boundary approach is based on the separation of the computational grid on solid and fluid regions by means of an interface. The grid points belonging to the fluid regions that have at least one neighbor in the solid region, are called immersed boundary (IB) points. There are different techniques to identify the solid and fluid nodes. In the present work, the level-set representation of the bed surface is exploited for this purpose. The grid points can be easily classified according to the sign of the implicit function $\phi(\mathbf{x}, t)$, $\phi < 0$, for $x \in \Omega_{\text{solid}}$ and $\phi > 0$, for $x \in \Omega_{\text{solid}}$.

In addition to the solid, fluid, and IB points, some additional points need to be specified when the IBM technique is used. Those points are presented in Fig. 4.4 and are:

▶ the IP points, which represent the intersection between the boundary interface and the normal line passing from the IB nodes.

▶ the PP points, which are fictitious points (they do not belong on the grid) lying on the line normal to the boundary passing from the IB point. These points are chosen to be as close as possible to the first fluid point.

As mentioned before, to estimate the forcing term f_i, on the RHS side of the Navier-Stokes equations interpolation techniques are used. In particular, the velocity of the IB point, u_{IB} should be known, in compatibility with the boundary conditions of the boundary interface. The procedure to
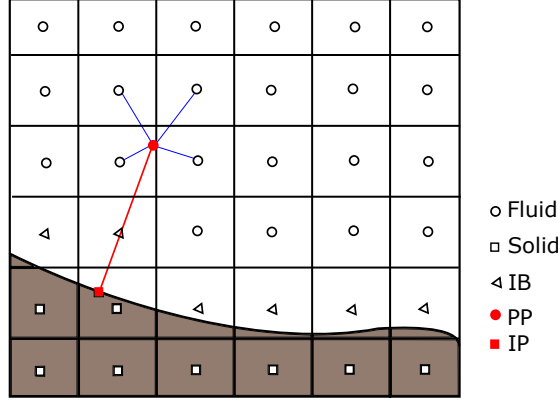
Figure 4.4: Node classification in 2D grid. The black circles denote the fluid nodes, the black squares the solid nodes inside the boundaries and the black triangles the IB points. The red lines represents the normal line on the interface passing from the IB points whereas the red circle is shows the PP point and the red square the IP point.

calculate the u_{IB} is the following. Initially, the velocity at the PP point is interpolated by the surrounding fluid nodes. Then, the bed shear velocity, u_*, is calculated using the law of the wall:

$$u_{\mathrm{PP}}^+ = \frac{u_{\mathrm{pp}}}{u_*} = \frac{1}{k} \log(d_{\mathrm{PP}}^+) + B, \qquad (4.26)$$

where $d_{\mathrm{PP}}^+ = d_{\mathrm{PP}} u_*/\nu$ represents the wall distance of the PP point from the boundary surface, k is the von Karman constant equal to 0.41, and B is a constant equal to 5.1. It is worth mentioning that considering the level-set representation of the bed, the normal vector to the boundary surface, for each grid point, can be easily approximated using the derivative approximations used for the level set function,

$$\mathbf{n} = \frac{\nabla \phi}{|\nabla \phi|}. \qquad (4.27)$$

Finally, since the wall distance between the surface and the IB points (d_{IB}^+) is known, u_{IB} can be calculated from the equation below:

$$u_{\mathrm{IB}}^+ = \begin{cases} \frac{1}{k} \log(d_{\mathrm{IB}}^+) + B & \text{if } d_{\mathrm{IB}}^+ > 11, \\ d_{\mathrm{IB}}^+ & \text{if } d_{\mathrm{IB}}^+ < 11. \end{cases} \qquad (4.28)$$

Additionally, the wall-normal velocity at IB nodes, v_{IB} is obtained by a parabolic interpolation. A more detailed description of the IB methodology can be found in (Roman2009a).

4.4 Coupling of the hydrodynamic and morphodynamic model

To simulate coupled hydro-morphodynamic sediment transport processes, the level-set method has been combined with the IBM and the LES-COAST solver as illustrated in Fig 4.5. It has to be mentioned that the level-set method is working separately from the LES-COAST model and their communication appears only through the IBM. Specifically, the initial bed interface defined by the implicit function ϕ is applied as boundary of the flow using the immersed boundaries and the governing equations of the flow are solved. At each time step, the calculated flow quantities, such as bed shear stress and sediment concentration, are used to evolve the bed interface through the advection equation Eq. 4.1. The new position of the bed interface is updated and used as the new boundary for the flow domain.

An important problem that arises from the coupling between the hydrodynamic and the morphodynamic models is the computational cost. In particular, the time step resulting from the CFL condition of the turbulent flow is usually prohibitively small. Thus, to update the bed interface with the same time step of the flow is very computational expensive [68, 117]. Considering that the flow field changes much faster than the bed interface due to sediment motion, two different time steps may be used. In work of Liang et al. [68] where they study scour below a pipeline the morphological time step is chosen to be $10\Delta t_{\text{flow}}$. The difference in time step depends on the speed at the bed interface changes at each specific problem.
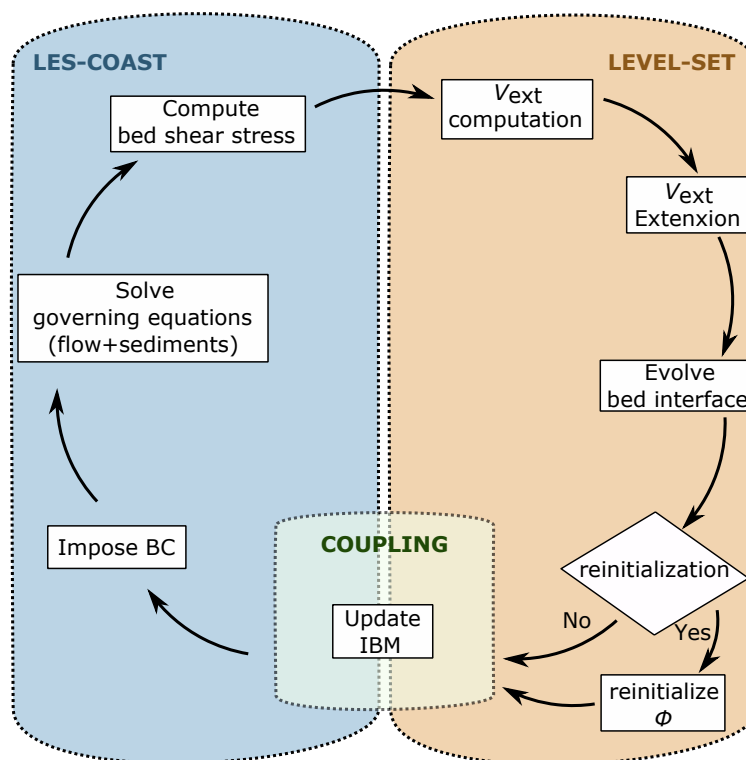
Figure 4.5: Flow chart of the overall coupling procedure.

Chapter 5

Assessment of the level-set method: Ripple migration

As described in the previous chapters the fluid motion over beds that are composed of loose sediment can lead to the entrainment of solid particles. The entrained material is then carried downstream and it may settles if the inertial forces acting on the sediment are small compared to gravitation, creating bed forms. In various circumstances (such as wave motion above sand beds), the interaction of the flow with the loose bed is followed by the creation of ripple-like structures, perpendicular to the flow [132]. As the flow evolves so do the bed structures while mantaining their shape [62]. In this chapter, large eddy simulation of suspended sediment transport above a ripple structure and the ripple migration are presented. In order to assess the implementation of morphodynamic model based on the level-set method proposed by Osher and Sethian [93], the work of Kraft et al. [62] is taken as reference. The study case is described in Sec. 5.1, while Sec. 5.2 presents the statistically stable velocity field and the suspended sediment concentration, before activating the mobile boundaries. Finally Sec. 5.3 shows the evolution of the ripple.

5.1 Study case

The numerical set-up used in this study mimics the one considered in the work of Kraft et al. [62]. The domain is 0.15 m long, 0.15 m deep, and 0.075 m wide and is discretized by a Cartesian grid that consists of $152 \times 128 \times 64$ cells, in the streamwise, vertical and spanwise direction, respectively. In the vertical direction the grid has been stretched in the vicinity of the loose boundaries in order to resolve all the relevant scales of the different flow quantities. It is worth noting that the resolution considered here is a bit higher than the one presented in [62].

The sediment interface is represented by the zero level-set and its initial
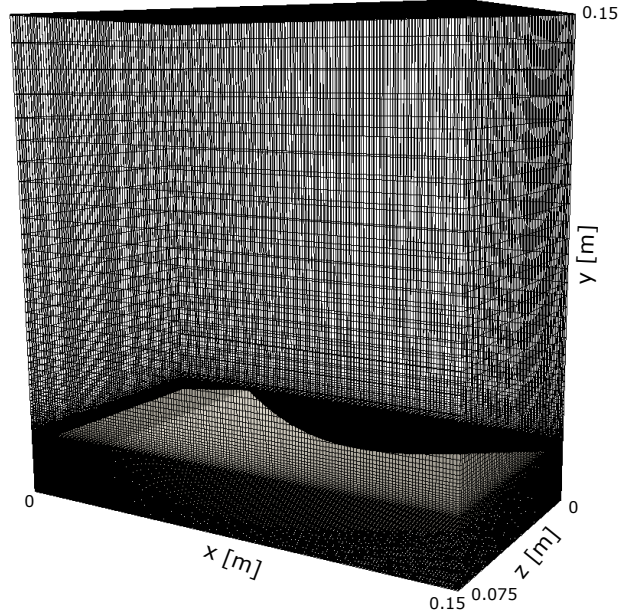
Figure 5.1: Numerical domain along with the grid and the bed interface.

configuration follows the ripple contour as proposed by Haslinger [48]:

$$\frac{y_k}{K} = 1 - 2.107\sin\left[1.15 \cdot \exp\left(\frac{2\pi x}{3L}\right) \cdot \sin\left(\frac{\pi x}{L}\right)\right], \qquad (5.1)$$

where K is the height of the ripple equal to 0.02, L represents the length of the domain, and x the stremwise position. This interface has been imposed as bottom boundary for the flow, using the immersed boundary methodology described in Sec 4.3. Fig. 5.1 illustrates the computational grid along with the immersed interface.

From the three different Reynolds numbers performed in Kraft et al. [62] the one that corresponds to mean velocity equal to $u_m = 0.4$ m/s is used in this work. The boundary conditions of the flow filed are periodic in the streamwise and the spanwise direction, no slip at the bottom wall, and free slip on the top boundary. Regarding the suspended sediment, a constant flux boundary condition has been implemented in order to reproduce the sediment exchange between the the flow and the bed. This flux is calculated according to Eq. 2.22. It is worth noting here that the direct calculation of sediment fluxes also eases the estimation of the propagation velocity of the sediment interface (see Eq. 4.3). For the estimation of the erosion rate, the approach of Van Rijn [145] is used (see Eq. 2.18) as proposed in Kraft et al. [62], to ease the comparison. The deposition rate is calculated using Eq. 2.19. The sediment diameter is equal to $d = 100$ μm and the critical

bed shear stress is $\tau_{cr} = 0.49$.

It should be noted that in the ripple migration problem the bed evolves
much slower to scouring. Therefore, in this work the time step used for
the evolution of the level set is equal to $50\Delta t_{flow}$, in order to reduce the
computational cost. This means that after each morphological update, 50
time steps of the flow field calculations are carried out and the averaged
value of the V_{ext} is then used the evolve the bed interface.

5.2 Velocity and sediment concentration filed above stationary boundaries

Since the evolution of the riple due to sediment transport is much slower
than the evolution of the flow field, Kraft et al. [62] assumed that, for each
instantaneous ripple contour the velocity and sediment concentration field
have arrived in a statistically quasi-steady state. Fig 5.2 shows the sta-
tistically steady velocity field, calculated in this study. The velocity field
indicates flow recirculation in the lead side of the ripple and the separation
point is located at the crest of the ripple at distance $x = 0.03$ m and the
reattachment point at the x-position around 0.1 m. These results agree well
with the observations made in [62].

An essential parameter for the incipient motion of sediment is the bed
shear stress distribution. In the regions where the bed shear stress exceeds
the critical value, the bed material starts to move and subsequently is en-
trained in the flow. The estimated spanwise-averaged bed shear stress over
the ripple bed is presented in Fig. 5.3 and is compared with the results of [62].
In wall resolved LES, the bed shear stress can be calculated by dividing the
velocity, at the closest grid-point to the interface, by its distance from the
interface. It is noteworthy to mention that the distance of each grid point
from the interface is directly obtained by the level-set representation of the
bed, since level-set function has been imposed to be equal to signed-distance
function (see Ch. 4). The distribution of the bed shear stress shows high
positive values on the stoss side of the ripple. At the crest of the ripple
that coincides with the seperation point of the flow, as well as at the reat-
tachement point, the bed shear stress drops to zero, as expected. At the lee
side of the ripple negative values of the bed shear stress are observed, with
lower absolute value than those detected on the upslope. In this region the
highest values are observed at the trough of the ripple. The negative sign
of the bed shear stress indicate that sediment is entrained in the opposite
direction of the flow. It worth noting that the bed shear stressed calculated
in this study are slightly higher than those observed in [62]. This can be
due to the different grid resolution.

After the velocity field has arrived in statistically steady state the sedi-
ment transport model is activated considering that the ripple is still station-
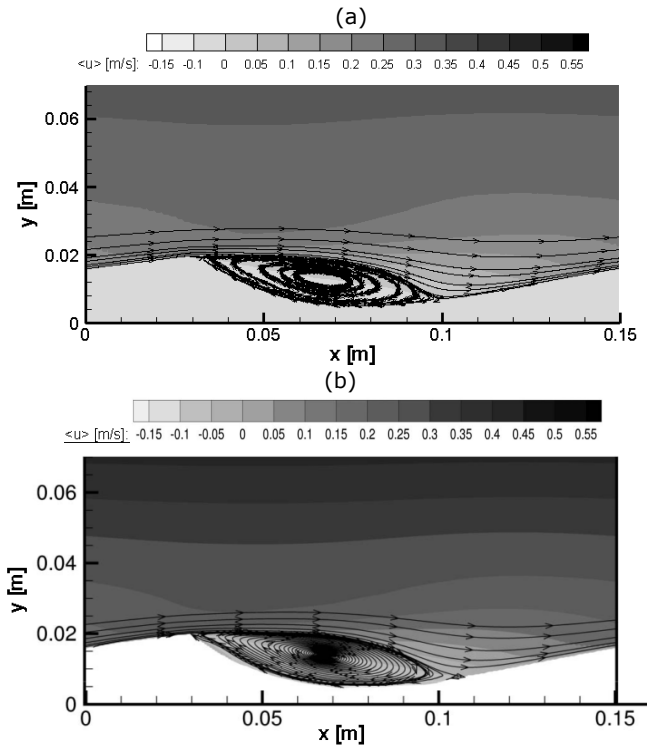
Figure 5.2: Statistically steady velocity field above the stationairy bed. a) numerical results obtained in the present study and b) results obtained in the work of Kraft[62].
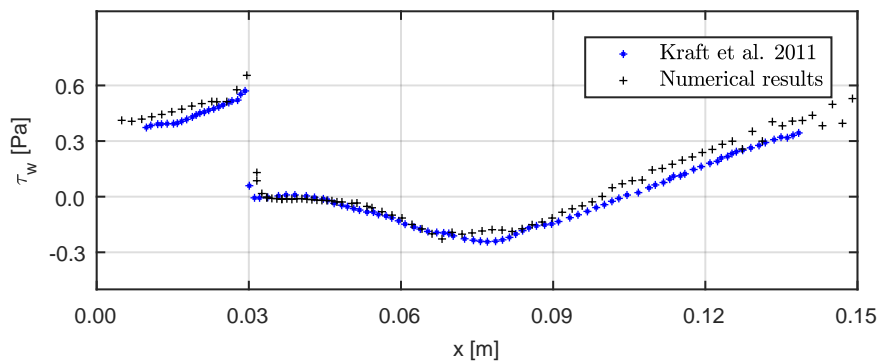
Figure 5.3: Statistically steady bed shear stress along the ripple baed compared wioth the results presented in [62].

ary. The transport of the suspended sediment concentration is simulated by the advection-diffusion equation (Eq. 3.12). In this sudy only suspended sediment is consider and the relative concentration is considered as a passive scalar. This means that density differences due to the presence of sediment are not taken into account in the momentum equation. As mentioned in Sec. 5.1, Van Rinj's approach is used to estimate the sediment pick-up. The distribution of the instantaneous spanwise-averaged suspended sediment concentration result of the application of the updated LES-COAST model at the time instant of 1 s is presented in Fig. 5.4. These results show that erosion mainly occurs in the stoss side of the ripple where the higher values of the bed shear stress are also observed. The entrained material is then transported downstream creating a finger-like shape, close to the separation point as reported in [62]. Additionally, entrainment is important at the trough of the ripple and downstream the reattachment point of the flow. In the region just after the separation point deposition seems to be more important. It is noteworthy that the tool used in this study captures correctly the main physics of sediment transport. However, some discrepancies can be observed compare to the results presented in [62] due to the different numerical models adopted.

5.3   Ripple migration

The velocity field and the suspended sediment distribution presented previously over a stationary boundary are used as initial conditions to simulate the migration of the ripple. The level-set method is used to track the bed interface evolution (see Eq. 4.7). In the case studied here, the externally-generated velocity filed is defined as in Eq. 4.3. As mentioned before, this velocity field is defined only in the vicinity of the ripple, so it has to be extended in the whole domain using Eq. 4.3.

The evolution of the ripples after $t = 60$ s is shown in Fig. 5.5 (green line) along with the initial position of the bed (red line). The erosion over the ripple structure is mainly present upstream the separation point and downstream the reattachment point of the flow, where the higher values of bed shear stress were observed. The deposition has a dominant role at the lee side of the ripple instead. This behaviour is in agreement with the one pbserved and reported in [62]. It should be noted here that, in this study, in order to decrease the computational cost of the simulations the bed interface is updated every 50 time steps which roughly corresponds to $t = 0.03$s. On the other hand Kraft et al. [62] have used the same time step for the flow and the morphodynamic model, a difference that may justify the small diversity in the ripple profile between the two figures.

Furthermore, as it has been also mentioned in [62], the constant threshold value of the wall shear stress prevents the periodic translation of the ripple
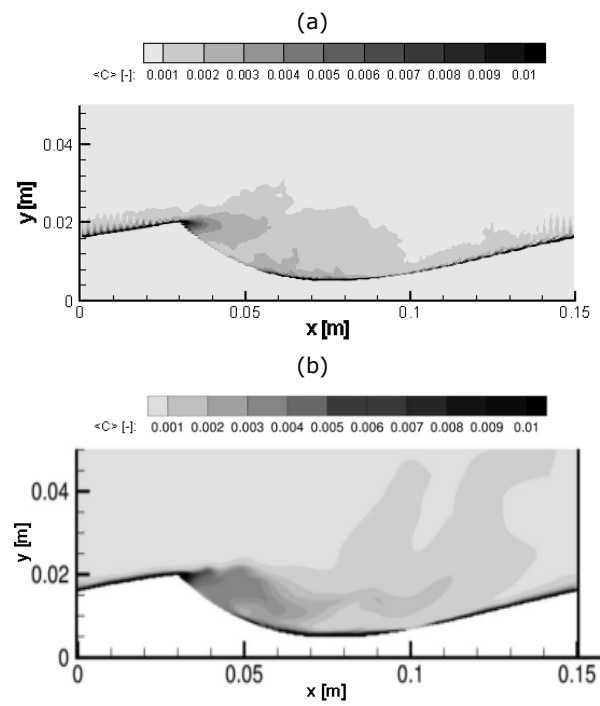
Figure 5.4: Spanwised-averaged suspended sediment concentration at the time instant around $t = 1$ s. a) numerical results of the present study and b) results presented in [62].
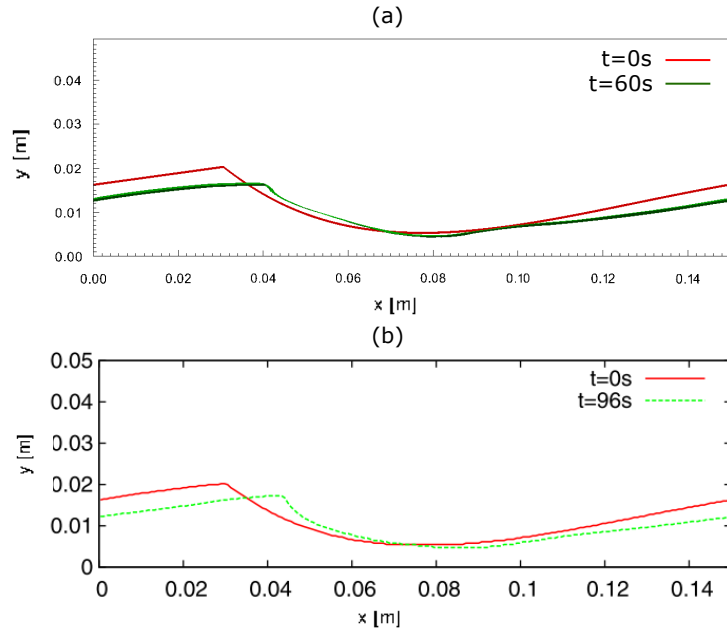
Figure 5.5: Bed evolution. The red line corresponds to the initial position of the bed and the green line to the evolved bed a) numerical results of the present study at the position at time $t = 60$ s and b) results presented in [62] at the position at time $t = 96$ s .

migration. In particular,in the regions in which the bed shear stress is close to zero, the assumption of a constant threshold does not allow the entrainment which is necessary for the periodic translation of the ripple. In order to overcome this problem, Kraft et al. [62] proposed to use Zanke's approach for the motion threshold (see Sec. 2.7). However, the scope of this chapter is the assessment of the morphodynamic model and not the detailed study of the ripple migration problem, so this theme will not be further investigated.

Chapter 6

Numerical simulations of sediment entrainment induced by gravity currents

This chapter deals with numerical simulations of the entrainment of sediment induced by the propagation of gravity currents over mobile beds. The sediment exchange between the flow and the bed is modeled by a flux boundary condition, which has been implemented, as part of this thesis, in the LES-COAST model. For sake of clearness, the bed deformation, for the cases studied in this chapter, are small enough so they can be considered negligible. Thus, the bottom boundary of the flow in the numerical simulations is considered stationary.

This study seeks to advance the knowledge on the main mechanisms that influence the sediment entrainment in buoyancy flows, by reporting and analyzing the results of high-resolution LES of salinity currents flowing over a mobile bed. For the simulations, it is considered currents with high Grashof number (10^4) driven by small density differences (less than 4%), so the boussinesq approximation holds true. The numerical outcome concerning the entrained material distribution is compared with experimental data. In particular, the main objectives are: 1) to numerically reproduce the entrainment and transport of particles induced by the passage of the current above the mobile bed, 2) to correlate the flow properties with the entrainment processes and to point out the control mechanisms of erosion 3) to identify the regions of the current that are the most active in terms of erosion 4) to estimate whether the entrained material influence the dynamics of the gravity current, and 5) to study the importance of the flow stratification on the distribution of the entrained material. For these reasons, two different current Grashof numbers and two different sediment diameters have been considered.

In this chapter, initially the study case is presented followed by a brief
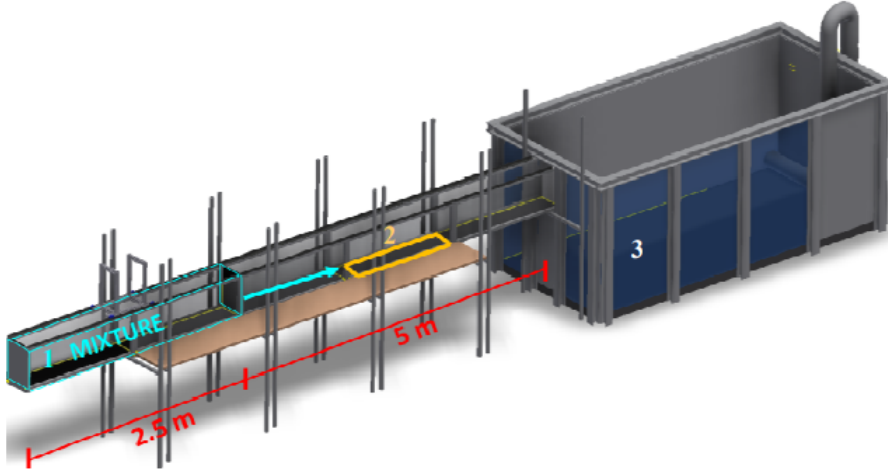
Figure 6.1: 3D view of the experimental set-up [165].

mathematical description and the used simulation parameters. Furthermore, the characteristics of the current, such as density profiles, velocity fields and the estimated bed shear stress are discussed. The final part of this chapter summarizes the results with respect to the sediment entrainment. First, the analysis of the sediment entrainment distribution, above the mobile bed, along with the comparison with experimental data are presented. Then, the correlations between the flow properties and the sediment entrainment, as well as the stability condition of the current are investigated. Finally, the main conclusions of this study are reported.

6.1   Description of the study case

The gravity currents that have been considered in this thesis are compositional, non-rotating, homogeneous, Boussinesq and of constant volume. The geometric configuration considered for studying the bed material entrainment is inspired by the similar experimental work performed by Zordan [165]. The experimental set-up is presented in Fig. 6.1. Specifically, it consists of a rectangular flume 7.48 m long, 0.2 m deep, and 0.275 m wide. Additionally, a big tank is located downstream of the flume, which serves for the dissipation of the current. Since the lock-exchange configuration has been used, the horizontal flume is divided in two volumes, each of which contains fluid with different densities due to salinity differences. These two volumes are separated by a movable lock-gate located at a distance $x_{\text{lock}} = 2.5$ m from the rear wall. In addition, at distance 2.5 m from the gate, there is a mobile bed 0.6 m long. In the experimental work, 3D instantaneous velocity measurements have been recorded using the 3D Acoustic Doppler Velocity Profiler (ADVP) [65, 31], exactly before the mo-
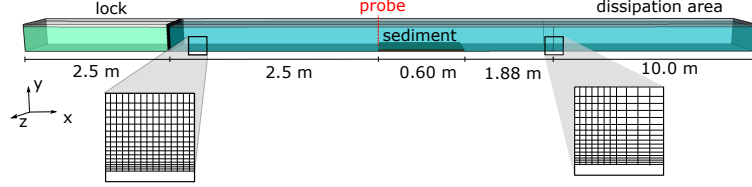
Figure 6.2: Conceptual model of the study case and mesh details (not scaled). The mesh at the dissipation part is coarser compared to the mesh of the rectangular flume.

bile reach of the bed. These velocity measurements have been done in such distance from the gate so they can be considered independent of the gate opening speed. Moreover, the lateral evolution of the flow above the mobile bed has been recorded by a high-speed camera SMX-160.

The numerical simulations reproduce the rectangular flume presented in the experiments. The tank has been replaced by an extra part 10.0 m long. This part allows the dissipation of the current and ensures that the numerical results are nor disturbed by return flow or reflection of the current at the end of the flume. In this work only full-depth release cases are considered and the initial aspect ratio of the lock fluid is kept constant, for all the cases, equal to $R = H/x_0 = 0.08 << 1$ (where H denotes the height of the flume). The bottom of the flume is considered fixed except of the small mobile section where sediment can be entrained. A conceptual model of the numerical set up is given in Fig. 6.2.

6.2 Simulation parameters

In the experimental work of [165] different test runs have been performed varying the initial salinity difference and the grain size of the bed material. To reproduce numerically the influence of the initial salinity difference, gravity currents with varying Grashof number, Gr, have been simulated. On the other hand, the differences on the bed material are simulated by adapting the settling velocity w_s and the Shields parameter θ_{cr}. The Gr is defined as:

$$\text{Gr} = \left(\frac{u_b H}{\nu}\right)^2, \tag{6.1}$$

where u_b is the buoyancy velocity of the current equal to:

$$u_b = \sqrt{g'H}. \tag{6.2}$$

Test	ρ_{lock}	g'	u_{b}	$\sqrt{\text{Gr}}$	d	u_*	d^+	θ_{cr}	w_{s}	Rouse
	$[\text{kg/m}^3]$	$[\text{m/s}^2]$	$[\text{m/s}]$	$[-]$	$[\text{m}]$	$[\text{m/s}]$	$[-]$	$[-]$	$[\text{m/s}]$	$[-]$
A	1040	0.39	0.28	56000	80×10^{-6}	0.012	1.10	0.15	5.5×10^{-4}	0.10
B	1040	0.39	0.28	56000	150×10^{-6}	0.012	2.10	0.09	17.4×10^{-4}	0.30
C	1048	0.47	0.31	61000	80×10^{-6}	0.011	1.00	0.15	5.5×10^{-4}	0.11
D	1048	0.47	0.31	61000	150×10^{-6}	0.011	1.80	0.09	17.4×10^{-4}	0.35

Table 6.1: Parameters of the lock-exchange simulations

and

$$g' = g \frac{\rho_{\text{lock}} - \rho_{\text{w}}}{\rho_{\text{w}}}. \tag{6.3}$$

In the latest equation ρ_{lock} represents the density at the lock. It should be noted here that the ambient fluid volume beyond the lock has always density ρ_{w}. The density of the current can be transformed into salinity concentration by the state equation:

$$\rho = \rho_w \left[1 + \beta \left(C_{\text{sal}} - C_{\text{sal}}^0 \right) \right], \tag{6.4}$$

where (C_{sal}^0) stands for the salinity of the ambient fluid and is equal to zero.

In the simulations Gr varies from 56000 to 61000 in order to investigate the influence of the initial salinity concentration. Additionally, the importance of the sediment size on the erosion procedure has been investigated by changing the bed material. The simulation parameters are summarized in the Table 6.1. It is worth noting that, in all cases, the size of the sediment is considered small enough to be transported directly into suspension and the bed load is neglected. This can be also justified by the Rouse number (see Sec. 2) presented in the Table 6.1. The non-dimensional grain size d^+ is defined as:

$$d^+ = \frac{du_*}{\nu}, \tag{6.5}$$

where d is the mean sediment diameter (d_{50}).

Moreover, for the cases studied here the St is calculated and presented in Table 6.2. These values indicate that an Euler-Euler single phase approach can be used for the simulation of the suspended sediment (see Sec. 2.3.2). The mathematical and numerical model of the simulations are presented in details in the next section.

6.3   Mathematical and numerical model

For the simulation of the gravity currents the scaled, non-dimensional Navier-Stokes equations have solved using the LES methodology (see Sec. 3.5). The scaled parameters used are the buoyancy velocity of the current, u_{b} and the

Test	η	St_{d}
	[m]	[-]
A	5.5×10^{-5}	0.11
B	5.5×10^{-5}	0.12
C	5.1×10^{-5}	0.24
D	5.1×10^{-5}	0.27

Table 6.2: Estimated Stoke numbers for all the cases studied in this work

height of the flume, H. Hence, the Navier-Stokes equations are written as:

$$\frac{\partial \bar{u}_i^*}{\partial t^*} + \frac{\partial \bar{u}_j^* \partial \bar{u}_i^*}{\partial x_j^*} = -\frac{\partial \bar{p}^*}{\partial x_i^*} + \frac{1}{\sqrt{\mathrm{Gr}}} \frac{\partial^2 \bar{u}_i^*}{\partial x_j^* \partial x_j^*} - \frac{\Delta \rho}{\rho_{\mathrm{lock}} - \rho_{\mathrm{w}}} \delta_{i,2} - \frac{\partial \tau_{ij}^*}{\partial x_j^*}, \qquad (6.6)$$

It is worth mentioning that the dimensionless time scale for the currents is $t^* = H/u_b$. The scalar equations for salinity and suspended sediment concentration are those shown in Sec. 3.5. The density variation in the dimensionless momentum equation due to both salinity and sediment is equal to:

$$\frac{\Delta \rho}{\rho_{\mathrm{lock}} - \rho_{\mathrm{w}}} = \frac{\rho - \rho_{\mathrm{w}}}{\rho_{\mathrm{lock}} - \rho_{\mathrm{w}}} = \frac{\bar{C}_{\mathrm{sal}}}{\bar{C}_{\mathrm{sal}}^1} + \frac{s}{\beta \bar{C}_{\mathrm{sal}}^1} \bar{C}_{\mathrm{sed}}. \qquad (6.7)$$

The Schmidt numbers, that represents the ratio of the molecular viscosity ν to the molecular diffusivities of the scalars is considered equal to 600 for salinity and for sediment equal to 1.

The dimensions of the scaled numerical domain are $L_1 = 87.4H$, $L_2 = H$, $L_3 = 1.375H$. However, only a length of $37.4H$ in x is used for data analysis that corresponds to the length of the experimental flume. The part which serves for the dissipation of the current is omitted. This work aims to perform wall resolved LES and avoid the use wall functions. In this regard, the grid has to be fine enough in the vicinity of the walls ($\Delta y_1^+ \sim 1$ and $\Delta z_1^+ \sim 1$) in order to correctly resolve the viscous sublayer of the flow [106]. In the streamwise direction to correctly capture the streaky structures of the flow $\Delta x+ \sim 60$ is set to be ~ 60 as proposed by Tolyay [140].

$$\Delta x^+ = \frac{u_*}{\nu} \Delta x, \qquad (6.8)$$

$$\Delta y^+ = \frac{u_*}{\nu} \Delta y, \qquad (6.9)$$

$$\Delta z^+ = \frac{u_*}{\nu} \Delta z, \qquad (6.10)$$

where u_* represents the maximum spanwise-averaged bed shear velocity obtained at specific time step (see Fig. 6.3). Given the unsteady nature of the gravity currents it is not possible to have one constant value of the bed
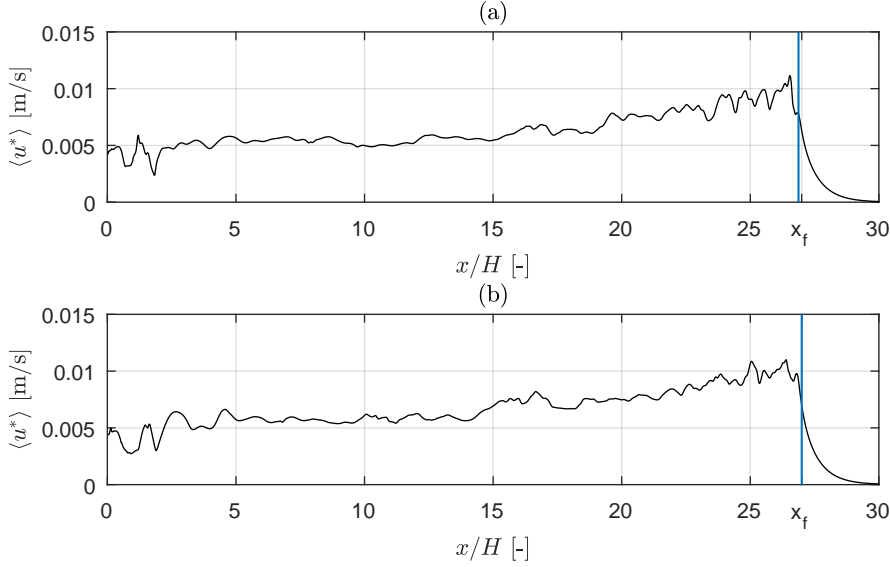
Figure 6.3: Instantaneous plots of the spanwise averaged bed shear velocity for case A and C.

shear velocity as for example in case of channel flows. It is obvious in Fig. 6.3 that the maximum value of the bed shear stress does not significantly vary with Gr. What differs is its distribution over the streamwise direction. In particular, the values of the bed shear stress, in case of higher Gr, remains relatively high for a longer distance upstream of the front of the current.

According to the aforementioned resolution restrictions, the computational grid used in this work is composed of $1336 \times 128 \times 80$ points in the main domain and 200 additional cells, gradually enlarged in the streamwise direction, for the region of the channel where the current is dissipated (see Fig 6.2). Furthermore, stretching has been applied on the vertical and spanwise directions following Vinokur's algorithm which uses an hyperbolic tangent law [152]. The grid spacing in the vicinity of the bottom and of the lateral walls is equal to $\Delta x_3 = \Delta x_2 = 0.0005H$, whereas away from the walls is equal to $0.01H - 0.04H$, similar to the one adopted in [92]. Table 6.3 shows the grid spacing in wall units. Moreover, the time step for the simulations is imposed equal to $\Delta t = 0.001t^*$.

The imposed boundary conditionas of the flow are no-slip at the walls in the spanwise and streamwise directions, as well as at the bottom of the channel. At the top surface of the flume a free-slip boundary condition is applied. Concerning salinity, a zero normal gradient is imposed at each boundary.

To reproduce the sediment exchange between the current and the bottom wall, a Neumann type boundary condition for the sediment concentration

Test	$\sqrt{\text{Gr}}$	Δx^+	Δy^+	Δz^+
A/B	56000	63	1	1
C/D	61000	62	1	1

Table 6.3: grid space in wall units in streamwise, vertical, and spanwise direction calculated for the two different Grashof numbers.

(see Sec. 2.3.4) has been implemented in the LES-COAST model in the framework of this thesis. The erosion rate is calculated by Eq. 2.17 whereas the deposition by Eq. 2.19. It is worth noting that the approach proposed by Luque and Van Beek [71] is adequate for particle diameter $d < 200 \ \mu m$ as the ones considered in this work.

The propagating salinity current, obtained by the LES simulations, is validated with experimental data in terms of the current shape and the time evolution of the front position above the mobile bed. The dynamics of the flow in terms of velocity field, bed shear stress distribution and turbulent structures have been evaluated before the currents starts propagating above the mobile section of the bed. It is worth noting, that the dynamics of the current have been studied upstream the mobile reach of the bed.

6.4 Results

In this section the numerical results obtained for the case A, B, C, and D are presented. These results have been compared with experimental data in terms of the current height, front position evolution and entrained sediment distribution.

6.4.1 Current evolution

In the non-dimensional simulations the density field of the salinity current is expressed as:

$$\rho' = \frac{\rho - \rho_w}{\rho_{\text{lock}} - \rho_w} \tag{6.11}$$

The ρ' has been initial imposed equal to 1 in the lock and zero in the rest of the flume. The evolution of the gravity current at three different time instants, before the current reach the mobile bed (case A/B), is presented in Fig. 6.4 using spanwise-averaged density contours. The symbol $(\langle \ \rangle)$ is used to illustrate spanwise-averaged quantities.

From the observation of the spanwised-averaged density field, it is possible to notice that, as the time advances, the Kelvin-Helmholtz instabilities created behind the front of the current loose their two-dimensionality and break in smaller eddies. In particular, in time $t = 8t^*$ 5 clearly 2D billows
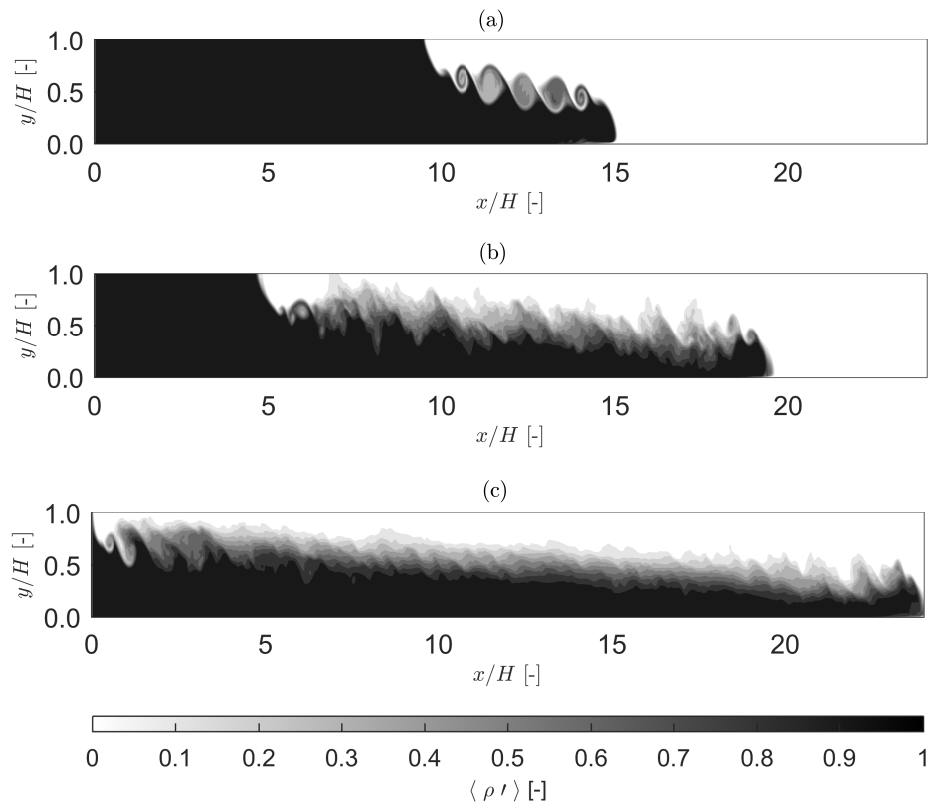
Figure 6.4: Spanwise averaged density contour of the gravity current with $\sqrt{\mathrm{Gr}} = 56000$ at time instant a) $t = 8t^*$, b) $t = 18t^*$, and c) $t = 28t^*$

.

can be observed behind the front. On the other hand, in time $t = 18t^*$, only the first two billows maintain their 2D character and at distance greater than $x/H \sim 1$ behind the front of the current the flow is highly three-dimensional.In this region, the Kelvin-Helmholtz instabilities are rapidly loose their coherence and break down into smaller turbulent eddies. The shedding of the billows lead to important mixing and a stable, slightly tilted stratified layer, extends in a long distance behind the front of the current. This behavior is in accordance with the one reported in the literature for gravity currents with high Grashof number [92, 19]. The mixing with the ambient fluid that takes place on the interface between the two fluids decreases the density of the current. This can be confirmed by the salinity distribution along the vertical. Specifically, the salinity concentration is higher in the lower part of the current and decreases as we are getting closer to the mixing interface.

6.4.2 Current height

In the lock-exchange configuration when the vertical gate that separates the two fluids is removed, a gravity current is created in the bottom boundary, whereas the ambient fluid forms a counter-current flowing in the opposite direction. Between the two fluids a mixing interface is created. The position of the mixing interface coincides with the height of the current. There are two ways to identify this position. The first approach, defines the height of the current based on the velocity measurements. Specifically, the interface is defined by the points where the streamwise velocity changes sign (see Fig. 6.5). The second approach determines the height of the current based on a density threshold [94, 43]. In the literature, different density iso-contours have been considered as threshold between the dense and the ambient fluid. In this work, the limit value, $\rho'_{\text{lim}} = 0.02$ as proposed by [94].

In this thesis, the first method is used only to compare the height of the current obtained numerically with the one defined in the experiments upstream the mobile bed. The reason is that in the experimental work only velocity measurements are available in this part. Thus, the spatial visualization of the shape of the current can be retrieved only by the time series of velocity measurements assuming that the frozen turbulence hypothesis holds true, and that the current is advected at nearly constant velocity. The velocity measurements have been recorded in the probe presented in Fig. 6.2 and t_{probe} denotes the time at which the current arrives at the probe. In the following sections, where the experimental results used for the validation of the model have been derived by video and image analysis, the first approach is considered more adequate.

The comparison between the numerical and experimental data with respect to the current height is presented in Fig. 6.6. To identify experimentally the position where the velocity is exactly zero is almost impossible.
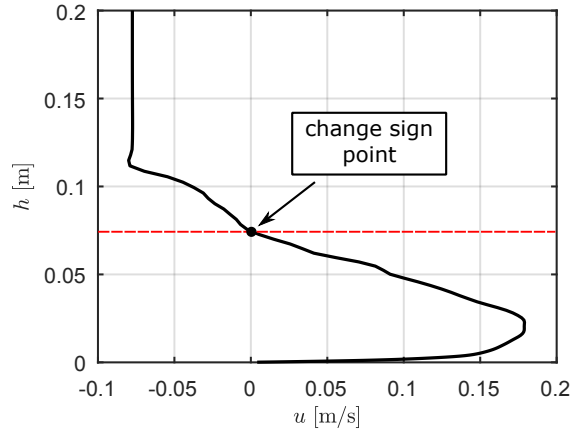
Figure 6.5: Vertical spanwise-averaged velocity profile at the head region of the head. The red dashed line indicates the height where the velocity change size

.

Therefore, the iso-velocity contour $u = 0.01$ m/s is chosen. It is noteworthy to mention that the error of the experimental measurements depends on the ADVP precision which is about ± 4.5mm. In particular, the total fluid height is divided in 44 equal spaced gates of about 4.5 mm each. The detection of the current height is therefore within this interval of error. Moreover, the experimental results are based on instantaneous velocity measurements. This may explain the differences that can be observed between the numerical and the experimental values. However, in a qualitative sense, the comparison gives a good agreement.

It can be observed in Fig. 6.6 that the height of the current is initially around $h \sim 0.1$ m and then remains constant equal to $h \sim 0.06$ m. The increase of the Grashof number does not seem to have any significant effect. The curve h presented in Fig. 6.6 can be also used to roughly estimated the head region of the current [90]. Specifically, the head region is extended until the first minima that follows after the maximum value of the height line. For both cases studied in this work, this minima is observed around $(t - t_{\mathrm{probe}})/t^* = 5$.

6.4.3 Front evolution

The temporal evolution of the front of the current for the cases B and C is presented in Fig. 6.7. In this figure, case B is represented by circles whereas case D by square markers. The dashed and solid lines stands for the fitting lines at each case respectively. The position of the front, x_{f} is calculated
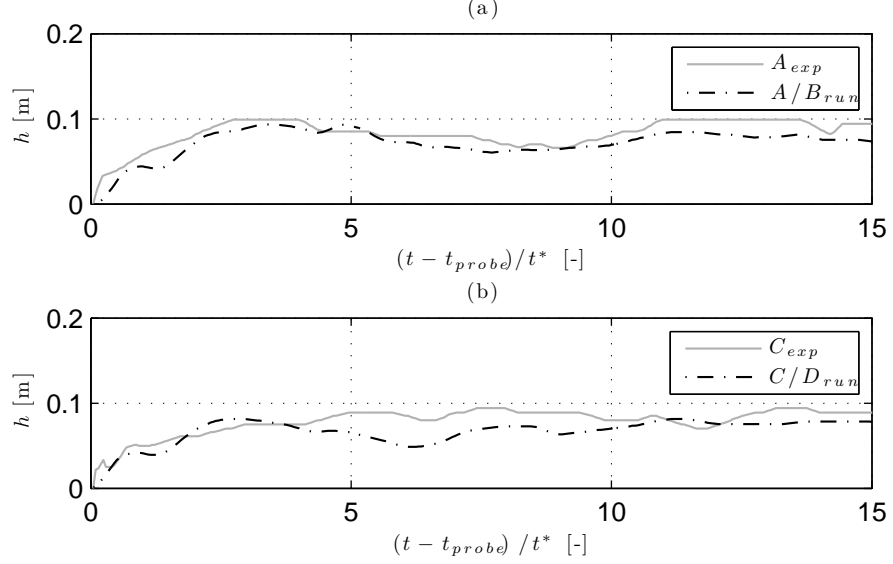
Figure 6.6: Representation of the current height. The numerical results (dashed line) are compared with experimental results (solid lines). a) correspond to $\sqrt{\mathrm{Gr}} = 56000$ and b) to $\sqrt{\mathrm{Gr}} = 61000$

.

with respect to the vertical gate,

$$x_{\mathrm{f}} = x - x_{\mathrm{lock}}, \tag{6.12}$$

where x_{lock} stands for the position of the lock gate. Numerically, the front position is identified by recording the evolution of the foremost point of the current located at height $y = 0.1H$ form the bottom of the flume [92]. The boundary of the current has been defined following the first approach described in the previous section. The influence of the Grashof number on the propagation of the current is obvious, as the slope of the line for case D is higher than the one of case B. The monotonically increase of the x_{f} over time indicates that the current is in the slumping phase. By definition, in this phase the front velocity of the current remains constant and can be calculated by the slope of the graph as:

$$u_{\mathrm{front}} = \frac{dx}{dt}. \tag{6.13}$$

The values of front velocity for each case are are about $0.45u_{\mathrm{b}}$ and are presented in Table 6.4.

The temporal evolution of the front of the current above the mobile reach of the bed are compared with the experimental results in the Fig. 6.7(b). Above the mobile reach of the bed, the identification of the current in the

Test	$\sqrt{\text{Gr}}$	u_{front} [m/s]	u_{b}[m/s]	Fr
A/B	56000	0.125	0.28	0.46
C/D	61000	0.14	0.31	0.45

Table 6.4: Froude numbers, calculated based on the channel height, for the two different Grashof numbers.

experiments was carried out by subtracting an initial image with ambient fluid to the images of the experiments. The precision of this method is in the order of the pixel resolution, i.e., 0.5 mm/pixel. The numerical results are presented by black color whereas the experimental results by gray. This comparison presumes a very good agreement between numerics and experiments. It is remarkable that the presence of entrained bed material, when the gravity current flows above the mobile section of the bed, does not influence the propagation of the current. Specifically, it can be observed in Figs. 6.7(a) and (b) that the slope of the lines does not change when the current is propagating over the mobile bed. The influence of the suspended sediment on the dynamic of the current is going to be studied in more details subsequently.

The front velocity of the current can be used to estimate the Froude number of the flow, Fr, with respect to the height of the channel,

$$\text{Fr} = \frac{u_{\text{front}}}{u_{\text{b}}}. \tag{6.14}$$

The calculated values are also presented in Table 6.4. These values are in the range of 0.45 ± 0.05, which is in agreement with what is reported in the literature for inviscid currents [6, 89]. This dimensionless quantity shows that, for all the cases, the currents can be considered sub-critical. This result justifies the use of the non-deformable slip boundary condition on the top of the flume. Furthermore, the values of the Froude number reflect the influence of the Grashof number on the propagation of the current. In particular, an increase in the Grashof number of the order of $8 - 10\%$ leads to a Froude number increase of approximately $2 - 3\%$.

6.4.4 Velocity fields

The numerical results of the streamwise and vertical velocity distribution as the gravity current passes from the probe, located upstream the mobile bed, are presented in Fig. 6.8. The propagation of the dense gravity current is illustrated by positive streamwise velocities at the lower part of the flume. The counter current that propagates in the opposite direction in the upper part of the flume, is characterized by negative streamwise velocities. The density difference across the interface between the two fluids, as well as the
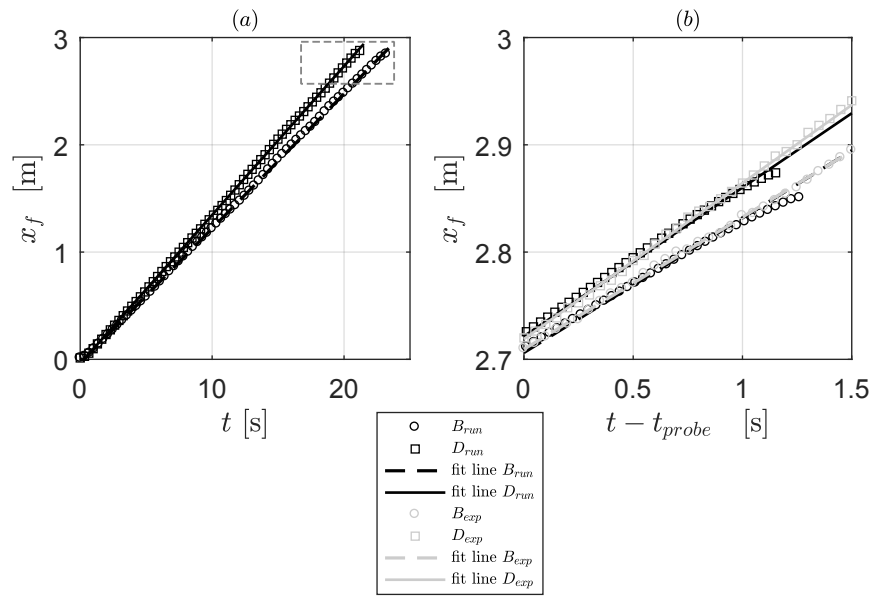
Figure 6.7: (a) Time evolution of the distance between the front and the lock for cases B and D. The dashed square indicates the time period that the current propagates above the mobile reach of the bed. (b) Time evolution of the front position above the mobile reach of the bed and comparison of numerical results with experimental data. t_{probe} indicates the time instant that the current arrives at the probe.
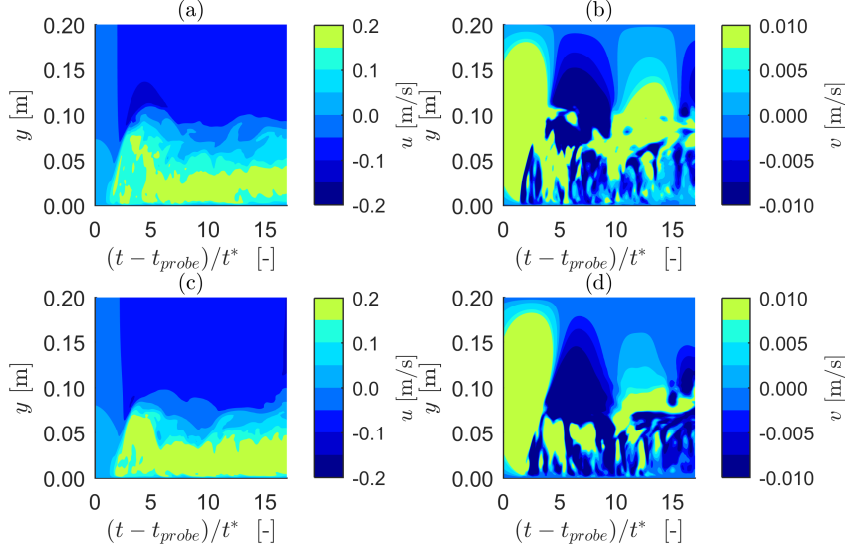
Figure 6.8: Numerical results of the instantaneous velocity contours. The measurements are taken in the Eulerian frame at the middle of the channel before the mobile section of the bed. The time is made dimensionless using $t^* = H/u_{\mathrm{b}}$. Plots (a) and (b) represent the streamwise and vertical velocities $\sqrt{\mathrm{Gr}} = 56000$, and (c) and (d) for $\sqrt{\mathrm{Gr}} = 61000$.

presence of velocities with different sign lead to the formation of a shear layer that induces the creation of Kelvin-Helmholtz instabilities. Furthermore, in Fig. 6.8(b) and (d) high positive values of the vertical velocities can be noticed. These values correspond to the upward movement of the ambient fluid which is displaced as the dense current arrives at the probe. The initial high positive values of the vertical velocities are followed by a sharp drop. This pattern repeats in the whole mixing area behind the head. It is worth mentioning that the periodic presence of vertical velocity stripes at the lower boundary of the current. It is assumed that these features will have an effect on the entrainment of bed material and they are going to be studied in detail in the next sections. The recirculation of the flow can been clearly seen in Fig. 6.9 that represents the instantaneous vector velocity field.

The streamwise velocities in the core of the gravity current are constantly higher than the estimated front velocities that have been presented in the previous section. This has been also reported in the works of [60, 4]. Moreover, the vertical profiles of the streamwise velocity at different parts of the currents are shown in Fig. 6.5. It can be observed that the max values of u are mainly observed at distance around $y = 25$mm from the bottom that roughly corresponds to $0.25 - 0.3$ of the current height. These results are in accordance with those reported in the literature for experimental gravity
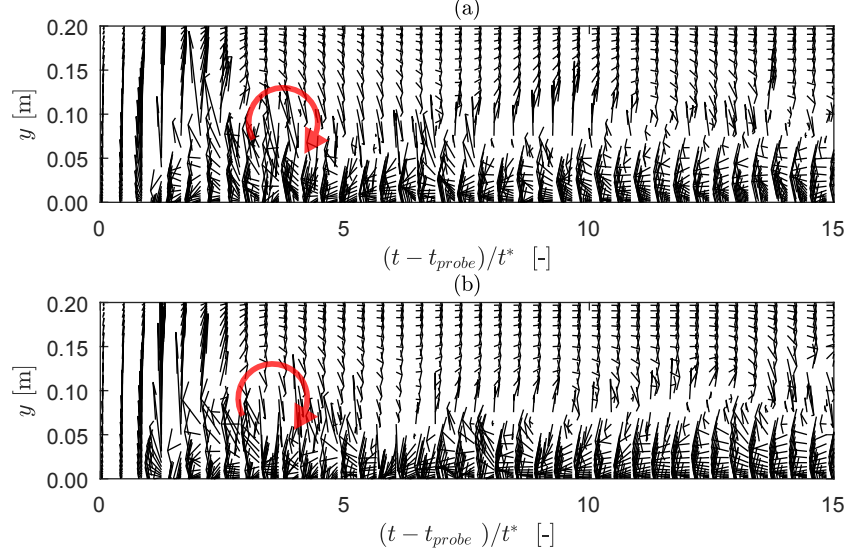
Figure 6.9: Instantaneous velocity vector field for $\sqrt{\mathrm{Gr}} = 56000$ and $\sqrt{\mathrm{Gr}} = 61000$. The red vector show the billows created behind the front of the current.

currents [59, 60]. Furthermore, it can be observe in Fig. 6.5 that the velocity profiles of a gravity current are similar to those observed in turbulent plane wall jets, as mentioned in work of Kneller [58]. Specifically, in both cases the profiles are characterized by an inner and outer region divided by the velocity maximum. In the inner region the velocity gradients are positive, whereas the outer region has negative velocity gradient.

The instantaneous velocity measurements, presented above, have been used to compute consecutive time-window averages $\langle U \rangle_t$ and $\langle V \rangle_t$. The size of the time window is chosen to be equal to $(t - t_{\mathrm{probe}})/t^* = 0.7$ according to [59, 4]. This time window has been chosen to avoid the the elimination of small frequency peaks and corresponds to 16 velocity recordings. The turbulent quantities, u_{rms} and v_{rms} computed as,

$$u_{\mathrm{rms}}(y) = \sqrt{\langle u'^2 \rangle_{\mathrm{t}}(y)} = \left[\frac{1}{n} \sum_{m=1}^{n} \left[u_{\mathrm{m}}(y) - \langle U \rangle_{\mathrm{t}}(y) \right]^2 \right]^{0.5}, \qquad (6.15)$$

$$v_{\mathrm{rms}}(y) = \sqrt{\langle v'^2 \rangle_{\mathrm{t}}(y)} = \left[\frac{1}{n} \sum_{m=1}^{n} \left[v_{\mathrm{m}}(y) - \langle V \rangle_{\mathrm{t}}(y) \right]^2 \right]^{0.5}, \qquad (6.16)$$

where n represents the number of points used for the time average, and u_m, v_m are the values of the streamwise and vertical velocity at each time instant
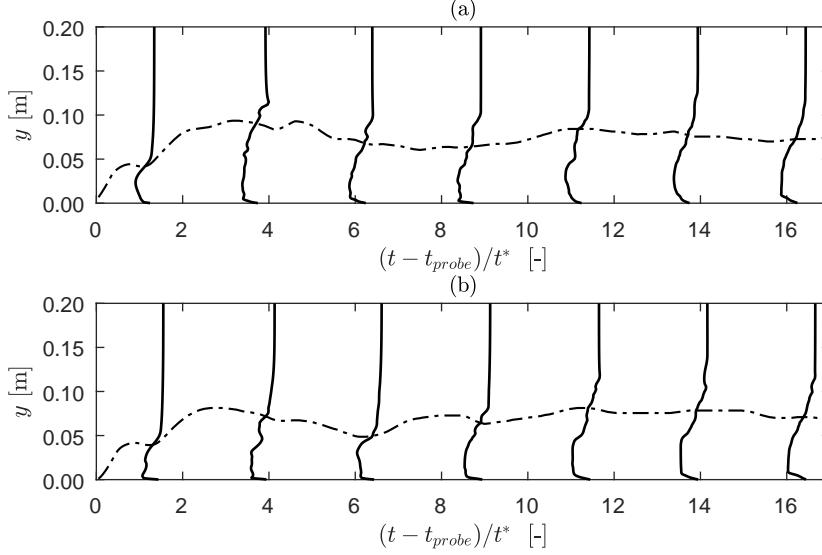
Figure 6.10: Instantaneous vertical velocity profiles at different positions plotted along with the shape of the current for $\sqrt{\mathrm{Gr}} = 56000$ and $\sqrt{\mathrm{Gr}} = 61000$.

m. The Reynolds stresses, τ_{Re} are also estimated as,

$$\tau_{\mathrm{Re}}(y) = -\rho \langle u'v' \rangle_{\mathrm{t}}(y), \tag{6.17}$$

where

$$\langle u'v' \rangle_{\mathrm{t}}(y) = \frac{1}{n} \sum_{m=1}^{n} \left[u_{\mathrm{m}}(y) - \langle U \rangle_{\mathrm{t}}(y) \right] \left[v_{\mathrm{m}}(y) - \langle V \rangle_{\mathrm{t}}(y) \right]. \tag{6.18}$$

Fig. 6.11 shows the averaged velocities $\langle U \rangle_t$ and $\langle V \rangle_t$ along with the turbulent quantities, u_{rms} and v_{rms}, and τ_{Re} for both Grashof numbers. The results are displayed at two different points in the vertical. One in the sublayer of the flow $y^+ = 11$ and one in the outer region of the flow $y^+ = 100$. The passage of the current from the probe is characterized by an abrupt increase of the streamwise and the vertical velocity. The mean streamwise velocity increases until $(t - t_{\mathrm{probe}})/t^* = 5$, where reaches the maximum value. As mentioned in Sec. 6.4.2 this region corresponds to the head of the current. After this point, the value of the mean streamwise velocity remains quasi constant since the flow has entered in the quasi-steady phase that characterised the body of the current [59]. On the other hand, the mean vertical velocity at the time period $(t - t_{\mathrm{probe}})/t^* = 0 - 5$ is characterized by a sequence of important upward and downward fluxes. These upward and
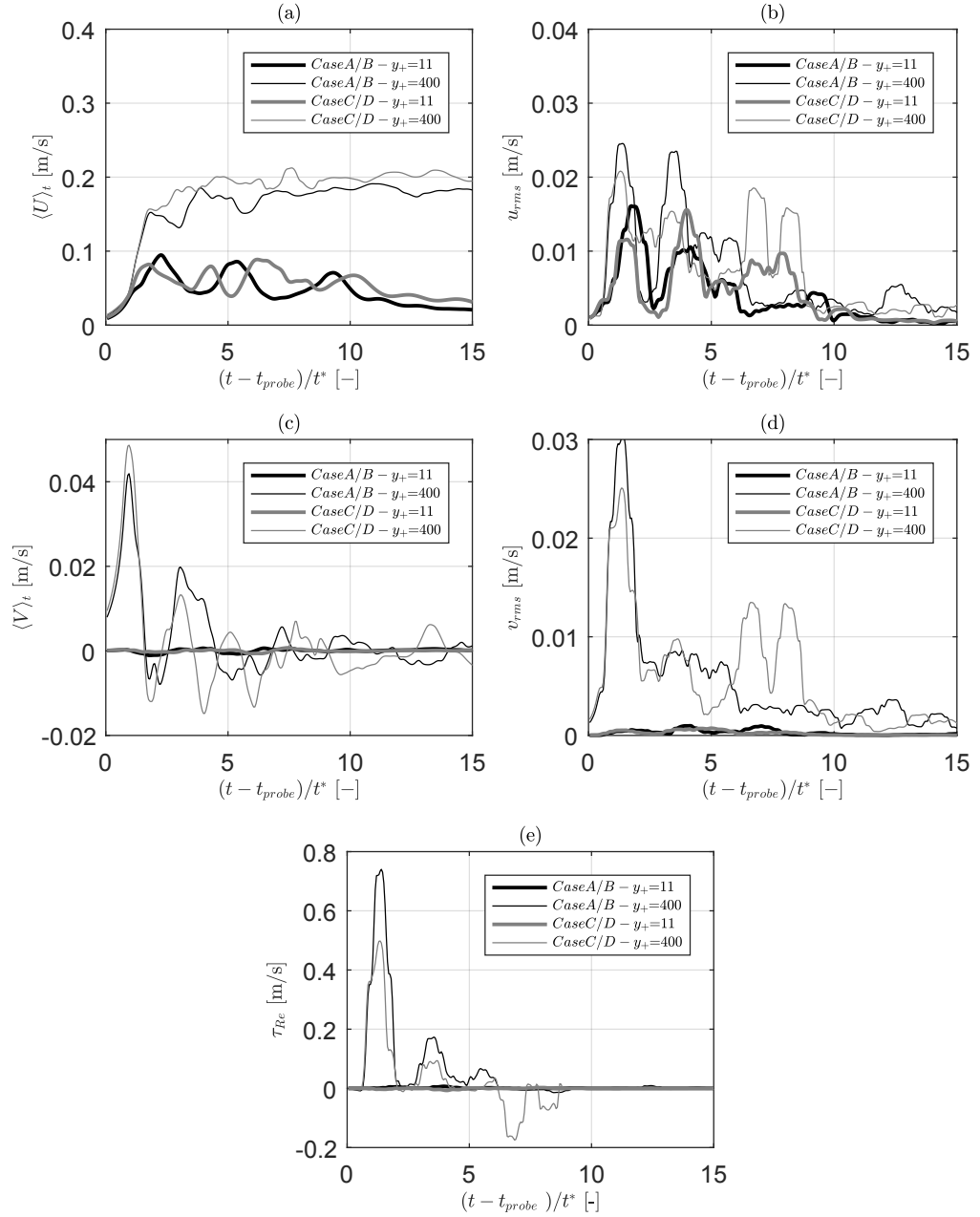
Figure 6.11: Time evolution of the (a) time averaged streamwise velocity $\langle U \rangle_t$, (b) streamwise velocity fluctuations u_{rms}, (c) time averaged vertical velocity $\langle V \rangle_t$, (d) vertical velocity fluctuations v_{rms}, and (e) Reynold shear stresses τ_{Re} at two different heights for $\sqrt{\text{Gr}} = 56000$, and $\sqrt{\text{Gr}} = 61000$.
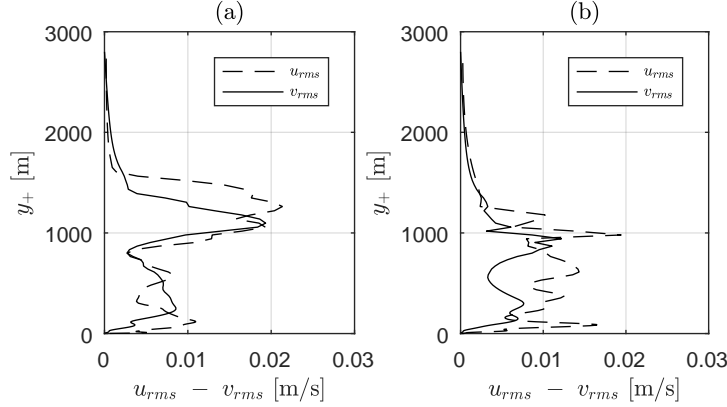
Figure 6.12: Vertical profiles of u_{rms} (dashed line) and v_{rms} (solid line) at the time instant $t = 1$s for a) $\sqrt{\mathrm{Gr}} = 56000$ and b) $\sqrt{\mathrm{Gr}} = 61000$.

downward flow movements continue also upstream of the front, but their amplitude its much lower.

The head of the current is strongly turbulent and is the region where the stronger mixing between the current and the ambient fluid occurs. This can be confirmed by the peaks of the $\langle U \rangle_t$ and $\langle V \rangle_t$ which are followed by peaks of u_{rms} and v_{rms} (see Figs. 6.11(b,d)). It is note worthy that in contrast to shear bounded flows, the higher u_{rms} and v_{rms} are recorded in the upper part of the current, away from the wall, Fig. 6.12. These values certify the fact that in gravity currents turbulence is mostly generated by the instabilities present at the upper boundary of the current.

In a turbulent flow, like the one reproduced in the present work, the total shear stresses can be modeled as the the sum of the Reynolds shear stresses, dominant in this case at the mixing layer created in the interface between the two fluids, and the viscous shear stresses, dominant at the vicinity of the wall. The Reynolds shear stresses, plotted in Figs. 6.11(e), are related to the instantaneous transfer of momentum in the current by the fluctuating field. Consequently, they follow the trends of u_{rms} and v_{rms} and their values decrease closer to the wall (see Figs. 6.12). On the other hand, the viscous shear stresses are related to the sharp velocity gradient in the viscous sublayer. Hence, their maximum is expected in the vicinity of the bottom wall. The bed shear stress distribution is studied in details in the following sections.

6.4.5 Turbulent structures

The Grashof number studied in this thesis is of order 10^4. For such high values of the Grashof number, the flow in the head of the current is expected
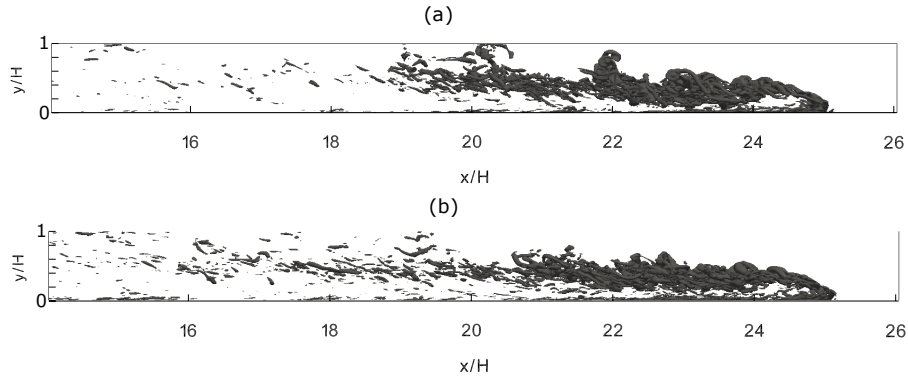
Figure 6.13: Turbulent structures in the current visualized by the λ_2 criterion, at time instant $(t - t_{\text{probe}})/t^* = 0$. The isosurface $\lambda_2 = -600$ is chosen. (a) $\sqrt{\text{Gr}} = 56000$ (b) $\sqrt{\text{Gr}} = 61000$.

to be strongly turbulent. Moreover, 3D coherent structures are expected to be created in the interface between the two fluids (front of the current and mixing interface) as well as at the turbulent boundary layer close to the bottom [11]. For the visualization of those turbulent structures, the λ_2 criterion [55] is used. This method identifies vortex cores as regions where high vorticity and pressure minima are present.

An instantaneous side view of the isosurface $\lambda_2 = -500$ for cases A and C is shown in Fig. 6.13. At the specific time instant, the front of the current is located exactly before the mobile bed. Four different regions can be identified according to different turbulent characteristics [11]. The first region is located in the upper boundary of the flow directly behind the front and it is dominated by two-dimensional turbulent structures. These area coincides with the part mentioned in Sec. 6.4.1 where the billows are still coherent. The second region includes the viscous sublayer in the bottom boundary of the flow. There, the flow is characterized by quasi-streamwise vortices and hairpin vortices inclined in the flow direction. The third region represents the area where the billows behind the front break down into smaller eddies and three dimensional structures are created. The turbulent structures in this region are slightly tilted, as it has also been mentioned previously for the mixing layer between the two fluids. Finally, the fourth region includes the remaining part of the flow, that devoid of strong turbulent structures. Increasing the Grashof number of the flow the first region becomes smaller. This means that turbulent structures loosing their coherence faster. Moreover, the three-dimensional structures of the third region are extended longer downstream. The presence of turbulent structures shown in Fig. 6.13 cinfirm the statement made in the previous section, according to which the head region is characterized by more intense turbulence compared to the body of the current.
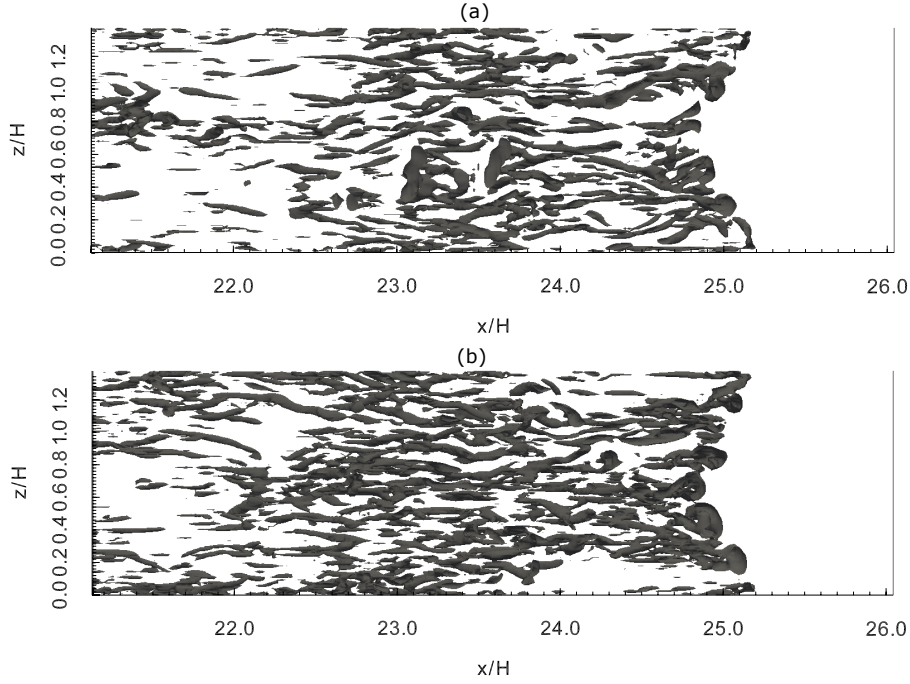
Figure 6.14: Top view of the isosurface $\lambda_2 = -200$ at wall turbulent layer, at time instant $(t - t_{\mathrm{probe}})/t^* = 0$. Only the region near the front is displayed. (a) $\sqrt{\mathrm{Gr}} = 56000$ (b) $\sqrt{\mathrm{Gr}} = 61000$.

Our interest in this thesis is focused on the turbulent structures of the second region. In Fig. 6.14 is displayed the top view of the turbulent structures in this region for both Grashof numbers. The majority of the quasi-streamwise vortices and hairpin vortices are concentrated at the head of the current ($x/H > 23$). Exactly on the front of the current the distribution of the structures can be associated with the lobes and clefts instabilities [11]. However, away of the front the structures loose their correlation with the lobes and their distribution is more dispersed. It is noteworthy that the spacing between the streamwise vortices decreases by increasing the Grashof number of the flow. It is known that these quasi-streamwise vortices and hairpin vortices, formed in the viscous sublayer, are associated with the streaky distribution of velocity in the vicinity of the wall [11].

6.4.6 Bed shear stress

The spatial and temporal distribution of the bed shear stress has a significant effect of the erosive capacity of the flow. Main years of research in the field of sediment transport have shown that bed material start to move when the bed shear stress exceed a critical value τ_{cr}. In nature and in laboratory experiments the exact estimation of the critical shear stress is a

very challenging task and is usually based in empirical estimations. However, in numerical simulations the sediment entrainment is imposed as function of the excess bed shear stress $\frac{\tau - \tau_{cr}}{\tau_{cr}}$. Therefore, an accurate estimation of the bed shear stress is of primary importance in the numerical modeling.

In this thesis, wall resolved LES have been performed. The grid has been stretched in the vicinity of the wall ($\Delta y^+ \sim 1$) to fully resolve the viscous sublayer of the flow. This allows to calculate the bed shear stress as:

$$\tau = \mu \frac{u_1}{y_1}, \tag{6.19}$$

where μ is the molecular viscosity of the fluid. y_1 and u_1 stands for the first grid point away from the wall and the velocity at this point respectively.

The top view of the instantaneous excess bed shear stress distribution for $\sqrt{\text{Gr}} = 56000$, exactly before the gravity current starts propagating above the mobile section of the bed, is shown in Fig. 6.15(a). In this figure, the read line indicates the position of the front of the current. It can be clearly observed the streaky pattern that follows the bed shear stress over the whole extend of the gravity current. Similar patterns have been also reported in the literature [92]. These streaks are related to the high and low streamwise velocities. High values of the excess bed shear stress are mainly located behind the front of the current at distance up to $x/h = 1.5$ away from the front. Further upstream, the values of the bed shear stress decrease but nevertheless the streaky pattern is maintained.

The temporal evolution of the excess bed shear stress at two different points in the spanwise direction is displayed in Fig. 6.15(b). Position z_1 corresponds to the middle of the channel, whereas position z_2 corresponds to a point located a quarter of the width away from the right lateral wall (see Fig. 6.15(a)). The bed shear stress have been recorded as the gravity current passes from the Eulerian framework located upstream the mobile reach of the bed. The differences between position z_1 and z_2 can be justified due to the presence of the streaks. It is remarkable that the initial high values of the excess bed shear stress, observed as the front of the current arrives on the probe, are followed by a sudden drop and then are increasing again. The position of the drop can be related to the position of the billows observed in Fig. 6.8. Thus, it can be assumed that the instabilities present at the mixing interface leave a footprint in the temporal evolution of the bed shear stress.

6.4.7   Flow sediment interaction

In the Sec. 1.2.1, it has been mentioned that the propagation of a gravity current over loose beds can trigger the transport of sediment. In this section, the innovation of the present work, which consists of the investigation of the bed material entrainment induced by salinity currents is presented.
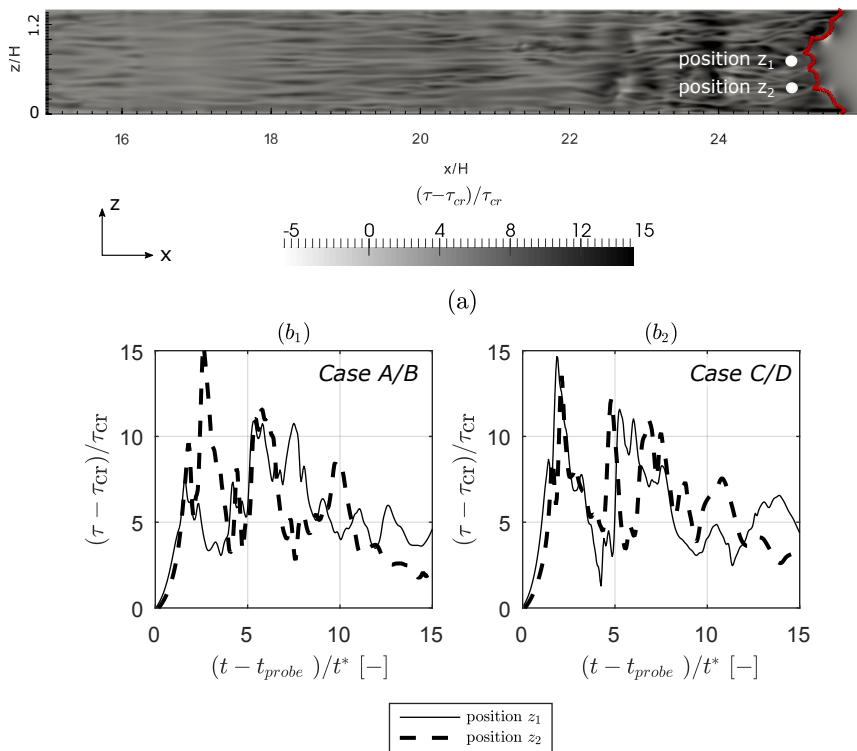
Figure 6.15: (a) Top view of the excess bed shear stress distribution at the bottom of the channel at time instant $(t-t_{\mathrm{probe}})/t^* = 0$ for $\sqrt{\mathrm{Gr}} = 56000$.(b) Time evolution of the excess bed shear stress for case A/B and C/D at two different points in the spanwise direction. Middle point (solid line,z_2) and a point located at a quarter of the width away from the right lateral wall (dashed line,z_1).

In particular, the entrained sediment distributions for two different Grashof numbers and two different sediment diameter is illustrated, compared with experimental data obtained by the work of Zordan [165]. Furthermore, the main mechanisms that lead to bed material entrainment are reported along with the influence of the suspended sediment on the dynamics and the stability of the current. It is worth noting that the deposition of the entrained material and the investigation of the bed forms, created downstream of the mobile reach of the bed, is out of the scope of this thesis.

Entrained sediment distributions

When the gravity currents, described in the previous sections, propagate over the mobile reach of the bed induces the transport of sediment into suspension. Snapshots of the spanwise-averaged suspended sediment concnetration, as result from the numerical simulations, are presented in Fig. 6.16. These snapshots are taken for a small interrogation window over the mobile bed. Each line in Fig. 6.16 corresponds to one of the cases A, B, C, and D. Moreover, each column illustrates a different time instant. The three time instants considered are $t_1 = (t - t_{\text{probe}})/t^* = 1$, $t_2 = (t - t_{\text{probe}})/t^* = 1.2$, and $t_3 = (t - t_{\text{probe}})/t^* = 1.4$. The shape of the current obtained numerically is illustrated by the grey solid line, whereas the sediment distribution is represented by the contour plot. L_{w} corresponds to the length pf the interrogation window and is equal to 0.24, whereas x_{w} stands for the streamwise position of the starting point of the interogation window, with respect to the position of the lock. This distance is equal to 2.7m.

The specific visualization of the numerical results is chosen in order to ease the comparison with the experimental data, which where taken by side view. It is noteworthy to mention that the experimental work of Zordan [165] does not provide exact measurements of suspended sediment concentration. Concentration measurements are a challenging task in the laboratory, especially in the case that two different substances are present (salinity and suspended sediment). This is one of the reasons that motivated this numerical work, to compliment the experimental results and investigate the aspects that cannot be addressed in the laboratory.

In the experiments, the propagation of the current above the mobile bed is recorded by a high-speed camera with acquisition frequency 25 Hz and resolution of 500×180 pixels. The obtained images are converted to greyscale matrices and subtracted by an the initial image that contains only the ambient fluid. Following this procedure the current and the ambient fluid can be separated by a sharp interface. Furthermore, the limit between the current and sediment is identified by an analysis of the recorded shades. This method is based on the fact that the current corresponds to a high luminescence whereas the sediment forms darker areas. However, a threshold for the identification of the pixels needed to be estimated. Therefore, the

pixel value associated to the sediment is annotated, at the beginning of the experiments, and used as reference to identify pixels characterized by the presence of sediment. It is important to mention that the precision of this method is based on the pixel resolution, i.e., 0.5 mm/pixel. The outlines of the regions covered by the current and sediment, obtained in the laboratory by the aforementioned procedure, are also illustrated in Fig. 6.16 by a grey and black line with circles, respectively. The red line plotted in Fig. 6.16 represents the iso-contour $C_{\mathrm{th}} = 2.0 \times 10^{-6}$ of the numerical data and is used to ease the comparison. The presented results show a qualitatively good agreement between the numerical and the experimental data. The bed material is mainly entrained in the head region of the current and diffuses over the whole current height. In the vicinity of the wall the concentration of the suspended sediment is higher due to the high shear present in this region. Moreover, it is noted that the suspended sediment distribution obtains a shape similar to the head recirculation. The exact prediction of the sediment region in the experiments is becoming more challenging in the upper boundary of the current. This is due to the intense mixing, present in this region, that leads to low luminescence in the experimental images. This can explain the discrepancy between the numerical and experimental data, that mainly occurs at the upper boundary. Nevertheless, the upward movement of the entrained material behind of the front of the current is also captured in the experiments to some extend.

The validation of the numerical results with respect to the bed material entrainement has been done also quantitatively by comparing the time evolution of the total area covered by sediment. The challenge of this procedure is the determination of a threshold value for the spanwise-averaged concentration, that marks the boundary above which the sediments are visible in the experimental images. The identification of this concentration threshold, C_{th}, requires calibration and is one of the main limitations of this study. To avoid this limitation, a relation that could connect the image luminescence to the concentration should exist. Unfortunately, this is not the case. The threshold value used in this work is $C_{\mathrm{th}} = 2.0 \times 10^{-6}$. This value is chosen to obtain an agreement with the physical evidence of the experiments. Apart of the sediment, the time evolution of the total area covered by the current is also calculated. However, the visible threshold, Sal_{th}, in this case is chosen to be equal to 0.02 as proposed in [94].

The total areas covered by the sediment as function of time is calculated by the following procedure. Once the threshold value has been determined, the cells on the xy plane that contain a spanwise-averaged suspended sediment concentration higher than the threshold parameter are identified and added. The same procedure is adopted to calculate the total area covered
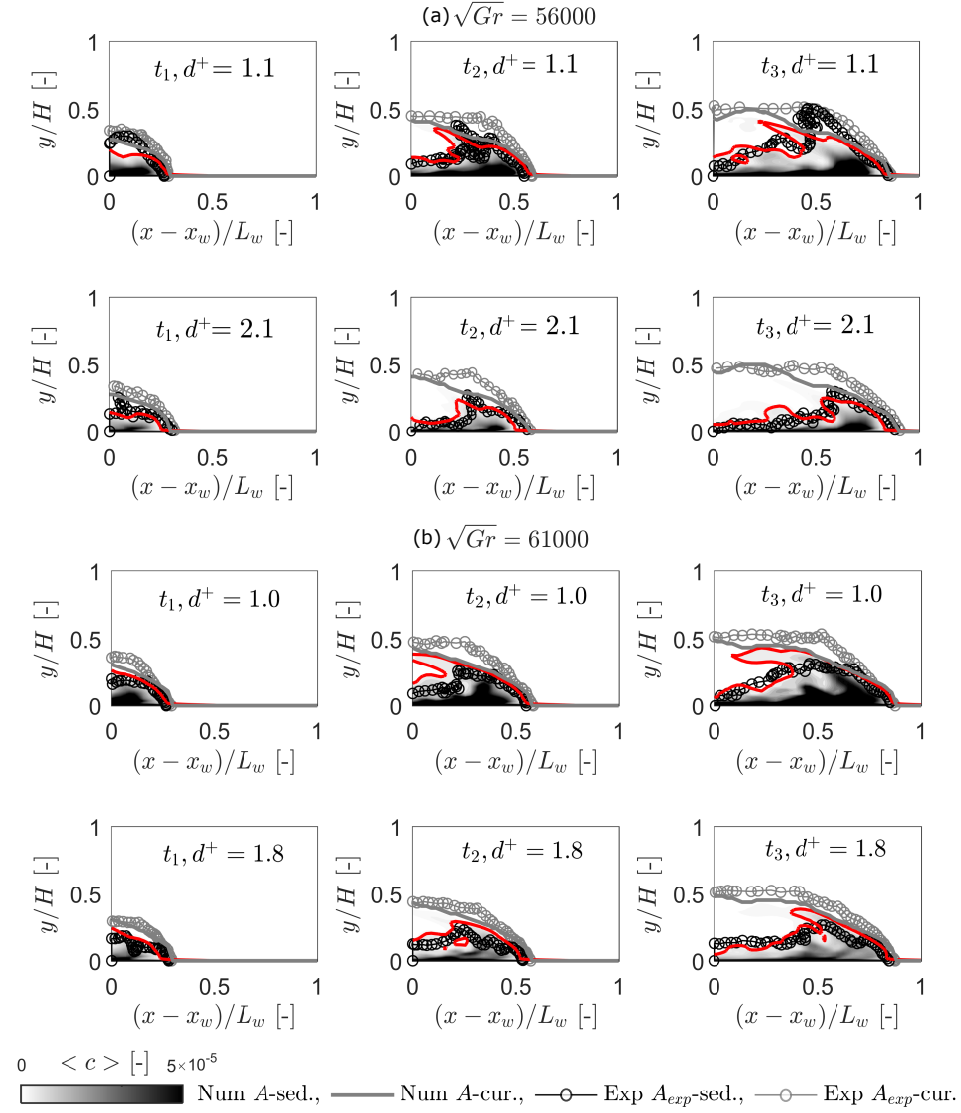
Figure 6.16: Numerical and experimental sediment concentration and current shape at different time instants. The black solid lines shows the the shape of the current, and the contour plots illustrate the spanwise-averaged sediment concentration, both calculated numerically. The experimental shape of the current and area covered by sediment are shown with gray and black circles, respectively. The read solid line illustrates the iso-contour $C_{\text{th}} = 2 \times 10^{-6}$ of the numerical data. Each line of figures correspond to the cases A, B, C, and D, respectively.

by the current. This procedure is expressed mathematically as:

$$A_{\text{sed}}(t) = \sum_{i}^{M} \Delta x_i \Delta y_i \zeta_i(t), A_{\text{sal}}(t) = \sum_{i}^{M} \Delta x_i \Delta y_i \xi_i(t), \qquad (6.20)$$

where M corresponds to the number of the cells, and Δx_i and Δy_i are the size of each cell in the streamwise and vertical direction, respectively. Moreover,

$$\zeta_i(t) = \begin{cases} 1 & \text{if } \langle C_{\text{sed,i}}(t) \rangle \geq C_{\text{th}} \\ 0 & \text{otherwise}, \end{cases} \quad \xi_i(t) = \begin{cases} 1 & \text{if } \langle C_{\text{sal,i}}(t) \rangle \geq Sal_{\text{th}} \\ 0 & \text{otherwise}. \end{cases} \qquad (6.21)$$

The calculated areas are presented in Fig. 6.17 and are compared with experimental data. The areas have been made dimensionless using the area of the interrogation window ($L_{\text{w}} = 0.24$ m $\times H_{\text{w}} = 0.2$ m). These results illustrate that, the time instant that the current enters in the interrogation window A_{sal} starts to increase. The same time corresponds to the moment that the current arrives the mobile section of the bed. Thus, bed material is entrained due to erosion and A_{sed} is also increased. Moreover, it is observed that after $(t - t_{\text{probe}})/t^* = 5$ the A_{sal} remains constant. This period correspond to the time that the front needs to cross the interrogation window and can be calculated by the front velocity of the current, presented in Sec. 6.4.3, and the length of the window. The area covered by the sediment starts to increase a bit after the moment in which the current appears in the interrogation window. This area exhibits its peak value when the front of the current is still inside the window. At $(t - t_{\text{probe}})/t^* > 2.5$ the area covered by the sediment start to decrease and for $(t - t_{\text{probe}})/t^* > 5$, when the front exits the window, this area is almost dropped to zero. These results lead to the conclusion that the entrained sediment is advected downstream by the head of the current. The aforementioned results are in good agreement with the experimental data.

Mechanisms that influence sediment entrainment

Ooi [91] studying the bed shear stress distribution of high Grashof gravity currents assumed that such flows are able to entrained sediments over a large distance behind the front. However, the results presented in this work have shown that sediment entrainement into suspension mainly occurs in the head region of the current. The entrainment of the bed material into suspension requires the action of three different mechanisms. Initially, the material is set in motion due to shear. Secondly, the sediment is detached from the bed due to turbulent structures formed in the vicinity of the bed. Finally, upward turbulent fluxes move the particles away of the bed and keep them into suspension. Those mechanisms can be associated to the bed
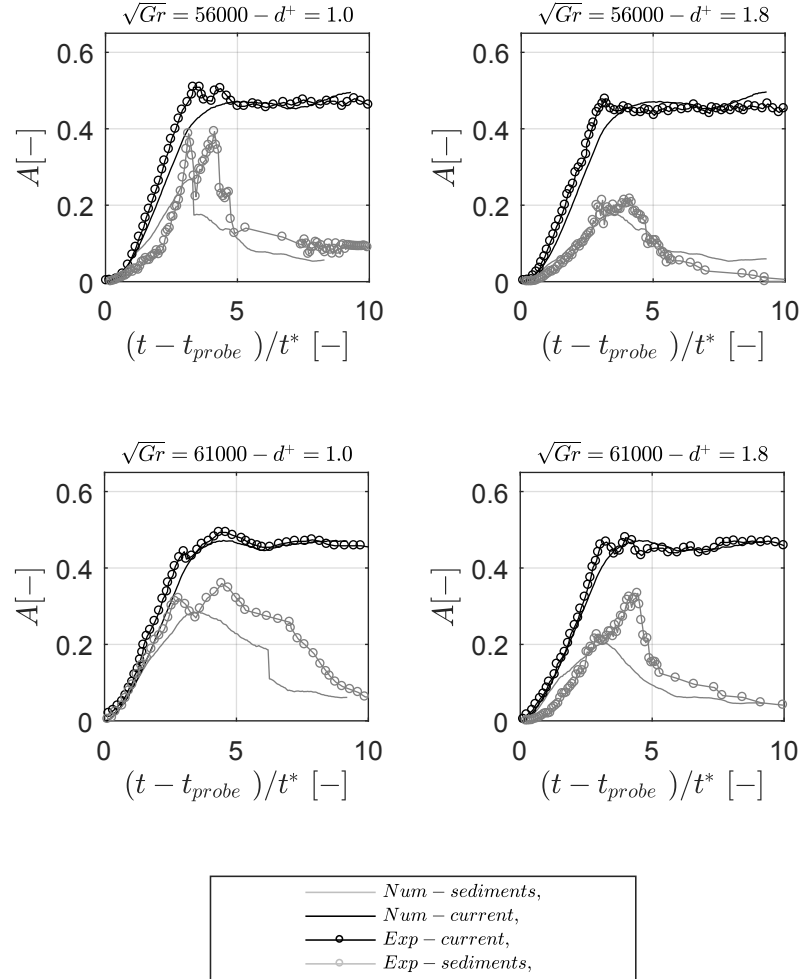
Figure 6.17: Time evolution of the cumulative areas covered by the gravity current (black) and the sediment (gray) for cases A, B C, and D. The numerical results are compared with experimental data: black circles for the gravity current and gray circles for the sediment.

shear stress, vertical velocity, vertical velocity fluctuations, and Reynolds stresses.

The streamwise distribution of the spanwised-averaged of those parameters is presented in Figs. 6.18 and 6.19, for both Grashof numbers, respectively. The position of the front of the current is also indicated by a vertical blue line. The excess bed shear stress, for both cases, takes values higher than 1 (that correspond to the initiation of motion) in an area that roughly corresponds to half the length of the current. However, the remaining quan-

tities are significant only in small area behind the front. Confronting these results with the suspended sediment distribution, it is confirmed that sediment is transported into suspension only in the regions of the flow that the high values of bed shear stress, vertical velocity, vertical velocity fluctuations, and Reynolds stresses coexist. In case of gravity current, the head is the region where this requirement is fulfilled. The body of the current is less powerful in terms of upward turbulence. In this region, the sediment may move within the small shear layer in the vicinity of the wall.

This Fig. 6.20 displays the top view of the excess bed shear stress distribution, for case A (at the time instant t_3 mentioned above) along with the top view of the sediment concentration very close to the bed. It is clearly observed that the sediment follows closely the excess bed shear stress distribution and forms the same streaky pattern that has been mentioned in Sec. 6.4.6. The results for the other cases are following the same pattern. It is worth noting that the dominant process in this stage is erosion and settling does not influence the sediment distribution.

After the bed material has been set to motion, due to the bed shear stress, it is expected to be trapped by the quasi-streamwise and hairpin vortices, present in the vicinity of the bed, and detached from the bottom boundary. This behavior has been already observed in channel flows [88]. To investigate this interaction, the top view of the near bed concentration isocontour equal to 0.0005 is presented, in Fig. 6.21 for case A. The created patters in this Figure are comparable with the turbulent structures presented in Fig. 6.14. Specifically, in the area behind the front, the sediment isocontour follow the hairpin vortices and is inclined versus the outer region of the flow. This indicates the tendency of the sediment to move upward. Moreover, farther upstream the sediment correlate with the quasi-stream wise vortices until those vortices loose their coherence. As mentioned in Sec. 6.4.5 the majority of the quasi-streamwise vortices is observed at distance $x/H = 0.2$ behind the front. The same happens for the sediment.

Additionally, the influence of the upward flow movements and the turbulent fluctuations on the transport of the sediment is investigated. For this purpose, the time-signals of v, v_{rms}, and τ_{Re} presented in Fig. 6.11 are used. In Sec 6.4.4 it has been mentioned that these signals vary over the vertical. To obtain a unique signal over the height of the current a depth average of those quantities has been calculated. Following this procedure the peak values at the upper and bottom boundary of the current are smoothed out. Once the depth averaged time-signal have been calculated, the contribution of each of those quantities on the sediment transport is estimated by calculating its correlation, $R_{A_{sed}\phi}(lag)$, with the time evolution of the total area
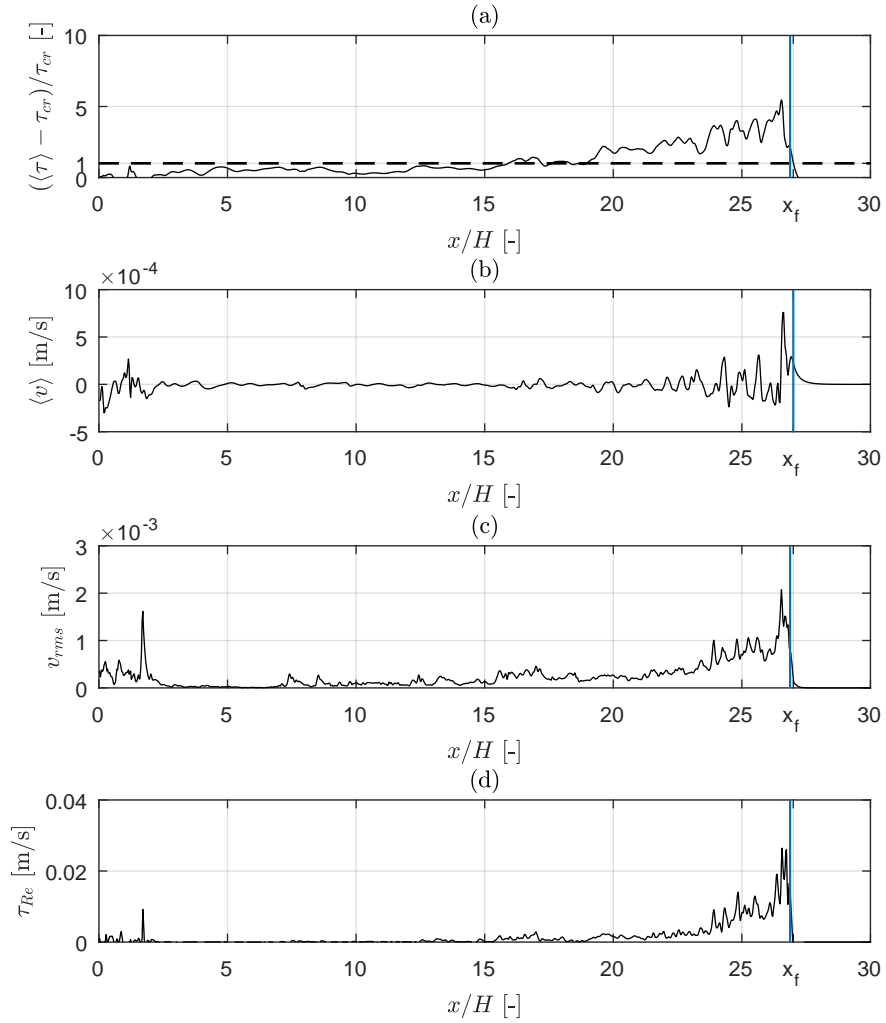
Figure 6.18: Instantaneous plots for case A, at time instant $t_3 = (t - t_{\text{probe}})/t^* = 1.4$, of (a) spanwise averaged bed shear stress, (b) spanwise-averaged vertical velocity at height $y^+ = 11$, (c) vrms at height $y^+ = 11$ and (d) Reynolds shear stresses at height $y^+ = 11$.
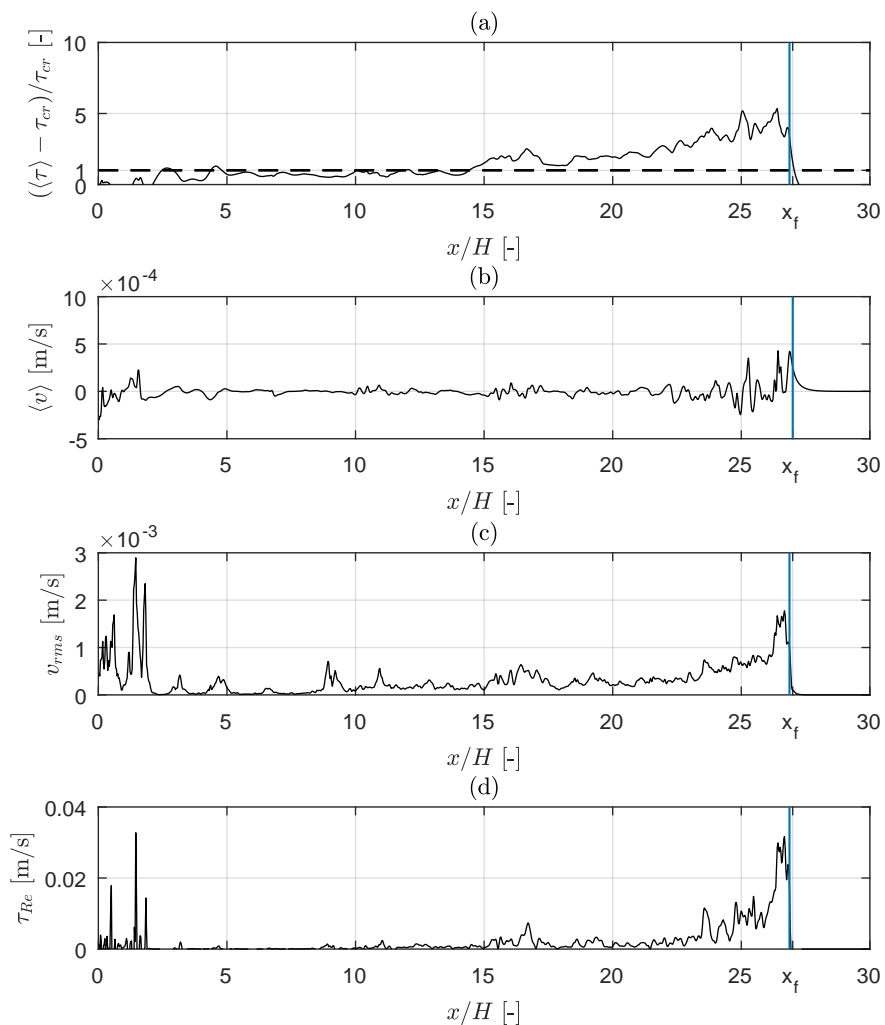
Figure 6.19: Instantaneous plots for case C, at time instant $t_3 = (t - t_{\text{probe}})/t^* = 1.4$, of (a) spanwise averaged bed shear stress, (b) spanwise-averaged vertical velocity at height $y^+ = 11$, (c) vrms at height $y^+ = 11$ and (d) Reynolds shear stresses at height $y^+ = 11$.
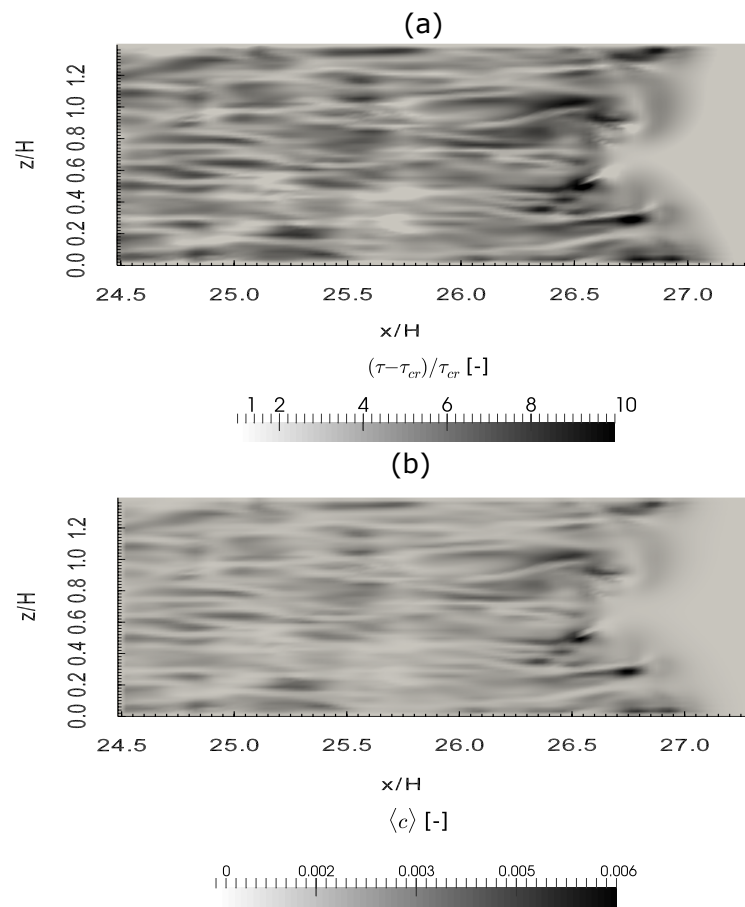
Figure 6.20: (Top view of (a) the excess bed shear stress and (b) the suspended sediment concentration above the mobile bed for case A (at the time instant t_3 mentioned in Sec. 6.4.7).
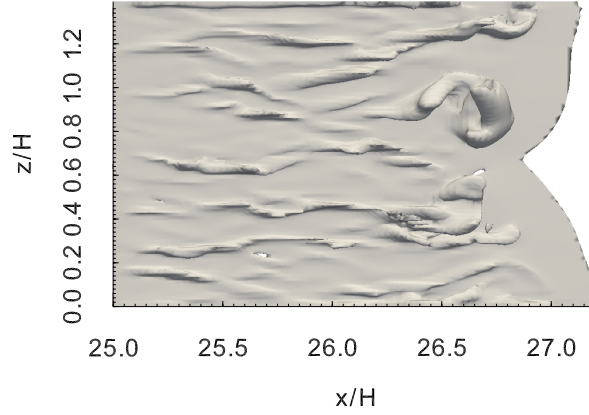
Figure 6.21: Top view of the suspended sediment concentration, isocontour
$c = 0.0005$, for case A. Only the region above the mobile bed is displayed,
at the time instant t_3 mentioned in Sec. 6.4.7.

covered by the sediment, A_{sed}. The cross correlation is calculated as:

$$
R_{A_{\text{sed}}\phi} = \begin{cases} \sum\limits_{n=0}^{N-m-1} (A_{\text{sed}})_{n+m}\phi_n, & \text{if } m \geq 0 \\ R_{A_{\text{sed}}\phi}(-m), & \text{if } m < 0, \end{cases} \tag{6.22}
$$

where N stands for the total time steps, m is the time lag, and ϕ represents
the signal that is correlated with the sediment area. The values of the
correlation are normalized so that the autocorrelation at the zero lag to be
equal to 1, obtaining R_norm. This normalized correlation, for all the cases,
is presented in Fig. 6.22. Such normalization eliminates the influence of the
numerical values of the signals and allows the correlation coefficient, R_norm
to vary between 1 and -1.

Using the aforementioned correlations, the integral quantity of the sus-
pended sediment concentration, over the whole interrogation window, A_{sed}
is related to time-signals recorded in the probe located before the mobile
reach of the bed (see Fig. 6.2). Different signals in various streamwise posi-
tion have been investigated, and it has been concluded that every x-position
inside the window is expected to register an equivalent signal. The correla-
tion presented in Fig. 6.22 reveal an important relation between the sediment
and the investigated quantities (v, v_{rms}, and τ_{Re}). However, a time lag of
$t_{\text{lag}}/t^* = 2$ is noted. This time lag is also observed in Fig. 6.17, where it was
mentioned that A_{sed} starts to increase a bit later than A_{sal}. Moreover, it is
observed in Fig. 6.11 that, $(t - t_{\text{probe}})/t^* = 2$ corresponds to the moment
when the first billow as well as the first group of large peaks of v_{rms} and
τ_{Re} have entered in the interrogation window. Consequently, it is the mo-
ment in which the sediment experiences the quickest diffusion upwards. It is
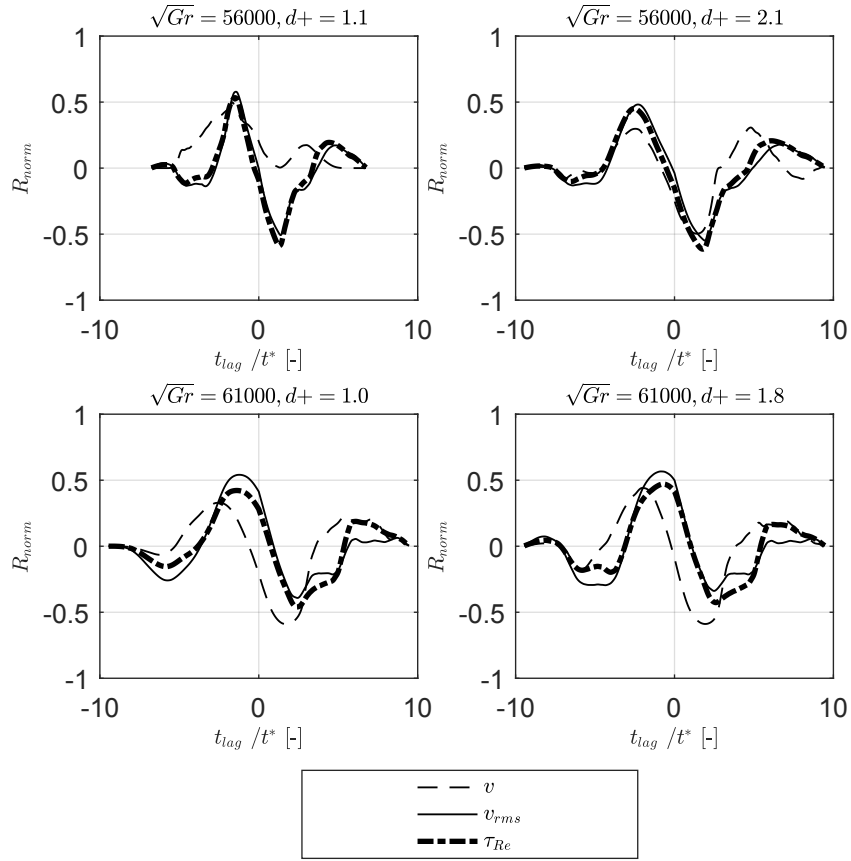
Figure 6.22: Cross-correlations between the time signals of the hydrodynamic variables, v, v_{rms} and τ_{Re}, and the time evolution of the cumulative area covered by sediment for cases A, B, C, and D, respectively.

noteworthy to mention that the initially important increase of the vertical velocities is followed by equally important drop. Therefore, negative correlations observed in Fig. 6.22. These negative correlations illustrate that, the sediment continuous to increase even if the upward movements are not important anymore. This can be explained by the fact that the head of the current is still inside the interrogation window so the strong upward diffusion is still active.

Stability conditions of the gravity current

As mentioned in Sec. 6.4.7 the presence of suspended sediment in the fluid column may influence the dynamics of the flow by creating density variation over the vertical. However, Fig. 6.7 shows that the evolution of the front does not change as the gravity current passes over the mobile reach of the bed.

This is an indication that the concentration of the entrained material is not strong enough to alter the dynamics of the current. To farther investigate this aspect the gradient Richardson number for both salinity and suspended sediment is calculated.

However, the suspended sediment concentration is not homogeneously distributed inside the body of the current (the entrainment is higher in the head of the current compared to the body). Thus, a layer Richardson number (see [157]) at different cross sections in the streamwise direction is calculated as:

$$\mathrm{Ri}_{gx} = \frac{-\frac{g}{\rho_w}\frac{\partial \langle \rho_k \rangle}{\partial y}}{(\frac{\partial \langle u_k \rangle}{\partial y})^2},\tag{6.23}$$

where k denotes each cross section in the streamwise direction.

The values of Ri_{gx} are shown in Fig. 6.23, for all the cases studied. The first column corresponds to the Ri_{gx} calculated based only to density differences due to salinity. The second column shows the Ri_{gx} only for suspended sediment and the third column illustrate Ri_{gx} taking into account both salinity and suspended sediment.

A gravity current flow can be characterized by poorly stratified regions (in the vicinity of the wall) and stable stratified regions (in the mixing interface) [58]. These areas are highlighted in the first column of Fig. 6.23. In particular, in the upper region of the current where intense mixing occurs the values of Ri_{gx} are higher than 0.25. It is worth noting that close to the velocity maximum of the current, the gradient of the velocity is almost zero thus the Richardson number goes to infinity. In the vicinity of the wall the negative values of the salinity Richardson number indicate the presence of unstable density gradients with active concective overturning.

As regards the sediment Richardson number it can be observed that Ri_{gx} obtains values higher than 0.25 only locally and mainly in case A. This leads to the conclusion that, due to the small suspended sediment concentration induced by the gravity currents the stratification effects due to sediments can be considered negligible. This conclusion is also confirmed by the total Richardson number, plotted in the last column, which does not show any particular difference with respect to the first column. However, the presence of suspended sediment may contribute to the reduction of the convection observed a the lower part of the current.

It is assumed that, the stratified conditions observed in the gravity current flow have an influence of the distribution of the suspended sediment over the vertical. Specifically, Turner [141] has stated that, in case where $Ri > 0.25$ there is not vertical transport. As mentioned before, in case of the gravity currents stable stratification is observed in the vicinity of the mixing interface between the current and the ambient fluid. Therefore, the dispersion of the suspended particles is suppressed and enclosed into the

height of the current. The limit on the distribution of the sediment, for each case, is defined by the gray solid line plotted in Fig. 6.16.
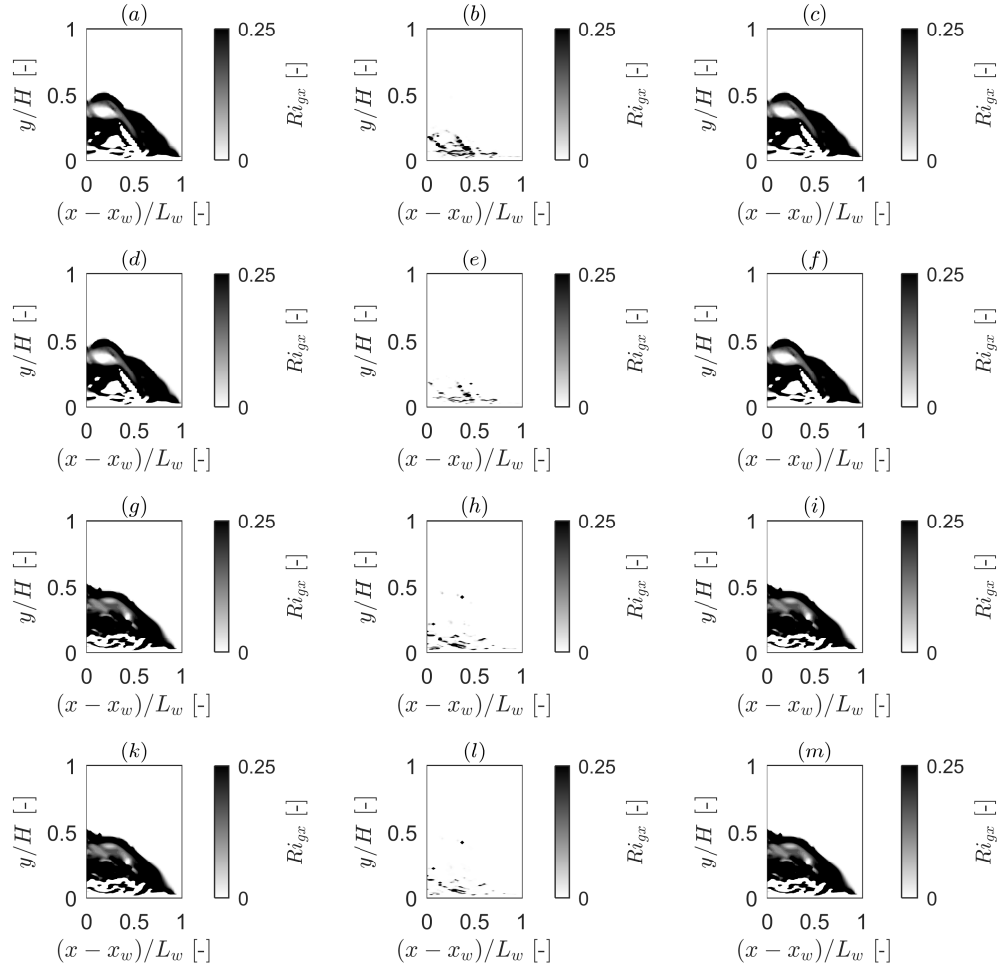
Figure 6.23: Gradient Richardson number at different streamwise positions, at the time instant t_3 mentioned in Sec. 6.4.7. The first column correspond to the gradient Richardson number Ri_{gx} based on salinity, for cases A, B, C, and D, respectively. The second column corresponds to the Ri_{gx} based on the suspended sediment, for the same cases. The third column corresponds to the Ri_{gx} based on both salinity and suspended sediment.

6.5   Conclusions

In this chapter the results of three-dimensional LES for high Grashof salinity currents flowing over a mobile bed are shown and discussed. Four different numerical simulations have been performed varying the Grahof number of

the flow and the sediment size on the mobile reach of the bed. These results aim to improve our knowledge on what concerns the interaction of gravity current with the bed material and the transport of sediment into suspension. In particular, the net fluxes of entrained bed material induced by gravity currents are presented and the flow features that involve into the sediment pick-up are investigated. Furthermore, the influence of the entrained sediment in the stability conditions of the current is examined along with the role of the stratification condition of the current on the distribution of the suspended sediments.

The description of the current and the analysis of the flow dynamics are presented in the first part of this chapter. The main features of the flow, such as the current height and the evolution of the front, are also compared with experimental data obtained by the work of Zordan [165], showing a good agreement. The velocity filed, the bed shear stress distribution, and the turbulent structures formed at the vicinity of the wall are studied in order to determined the region of the flow where strong turbulence is present. From those results, its is observed that the region called head of the current is characterized by high peaks of velocity fluctuations, Reynolds stresses, and excess bed shear stress as well as strong quasi-streamwise and hairpin vortices. Thus, it is assumed that bed material is transported in to suspension mainly in this region. In the body of the current the observed upward diffusion is weak. Thus, the sediment that has been set into motion in this area may move within a thin layer close to the bottom.

In the second part of the chapter, the spanwise-averaged suspended sediment distribution, in an interrogation window located above the mobile reach of the bed, are presented. Additionally, the total areas covered by the current and sediment in the same interrogation window are plotted versus time. These results confirm the aforementioned assumption. Specifically, suspended sediment mainly appears just behind the front of the current and there is almost no suspended load further upstream. Moreover, it has been indicated that the bed material entrained above the mobile bed is advected downstream by the head of the current, and settling seems to have a minor role in this stage of the flow. Bed forms may created downstream the mobile bed but their investigation is out of the scope of the present study.

The combination of the results obtain by the study of the flow dynamics and the suspended sediment distributions highlights the main mechanisms that contribute to the sediment entrainment in gravity currents. In particular, the bed material set in motion due to the excess bed shear stress, which is higher than 1 in an area that corresponds to the half of the current length. However, high values of excess bed shear stress do not imply that the sediment will be moved to the outer region of the flow. Particles detach from the bottom due to turbulent structures formed in the viscous sublayer as shown in Fig. 6.21. Once the sediment is detached, it is transported in the outer region of the flow due to upward turbulent fluxes that are able

to counteract its settling velocity. The specific contribution of the upward flow movements and turbulent fluctuations is also investigated. In order to quantify this effect, the time-evolution of the areas covered by sediment, in the interrogation window, are correlated with the time-signals of v, v_{rms}, and tau_{Re}. These correlations show that all three variables plays an important role in the sediment suspension. However, a time lag equal to $t_{\mathrm{lag}}/t^* = 2$ is observed.

Finally, the feedback of the suspended sediment on the dynamic of the current is examined. The observation of the front evolution upstream and above the mobile reach of the bed illustrates that the entrained material does not influence the propagation of the current. This aspect is further investigated by calculating the Richardson number of the flow due to both salinity and sediment. The results show that the presence of the suspended sediment is not strong enough to alter the stability condition of the current. On the other hand, it is indicated that the stable stratification conditions, that appear in the upper boundary of the current, inhibit the transfer of suspended sediment in the ambient fluid. In other words, the diffusion of the sediment over the vertical is confined by the current height.

Chapter 7

Numerical simulation of bed forms generated by gravity currents

The study presented in the previous chapter analyzes the sediment entrainment induced by gravity currents. in that case, the bed deformation due to erosion and deposition processes is considered small compared to the scale of the model. Thus, a stationary bottom boundary has been imposed as boundary condition in the numerical simulations. However, this assumption does not always hold true in nature. In particular, it has been reported in literature that multiple events of strong gravity currents can lead to important bed deformations which in turn may influence the dynamics of the flow. The aim of this chapter is to reproduce numerically and study the bed forms generated at the mobile reach of the bed by similar gravity currents. This is accomplished using the coupled hydro-morphodynamic model presented in Ch. 4. Moreover, the deposition patterns directly downstream of the mobile reach of the bed are analyzed. The numerical domain used in this study is described in Sec. 7.1 and the results are presented in Sec. 7.2.

7.1 Case study for the investigation of bed forms

Similarly to the previous chapter, a 3D large eddy simulation of a gravity current flowing over a partially mobile bed is simulated using the lock-exchange configuration. However, there are three main differences between the two cases. First, the gravity current simulated here has higher erosive capacity (the Grashof number is almost double than those considered in the previous chapter). Second, the length of the lock and the entire domain is smaller. Third, the mobile reach of the bed is located closer to the lock gate. Specifically, the dimensions of the scaled domain are $L_1 = 17H$, $L_2 = H$, $L_3 = 0.67H$. The lock-gate is located at a distance $x_{\text{lock}} = 2.67/H$ from
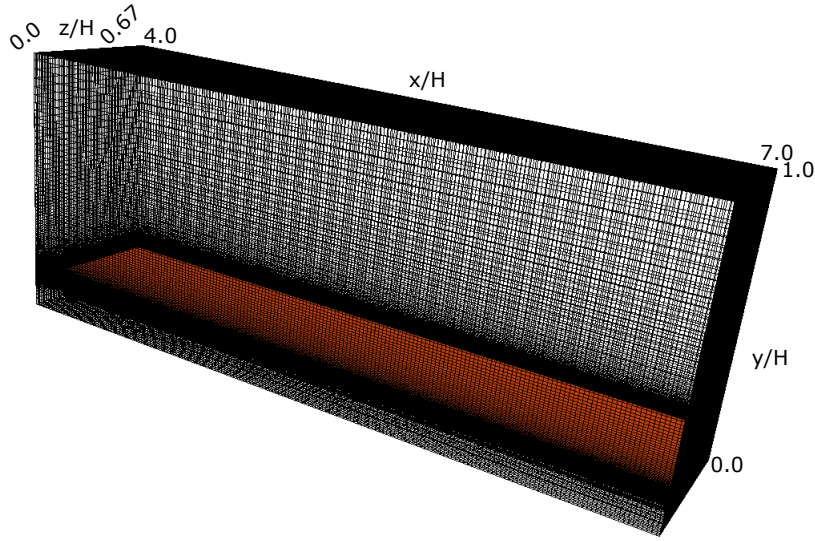
Figure 7.1: Zoom-in of the computational grid along with the initial bed interface.

the rear wall and the mobile reach of the bed is at distance $2.53/H$ from the gate and is $2/H$ long. It is worth noting here that the mobile reach of the bed has the same length as in the previous study. This domain has been discretized by a Cartesian grid that consists of $1024 \times 128 \times 64$ grid cells. The grid has been stretched in the vertical direction around the bed interface in order to fully resolve the viscous sublayer of the flow.

The bed interface is initially considered flat and is tread by the immersed boundary methodology. The evolution of the bed interface is tracked by the level-set method. It should be mentioned that, in this case, the hydro-morphodynamic model is fully coupled. In other words, the Δt used for the morphodynamic model is the same with the Δt of the flow. A zoom-in of the computational grid and the bed interface is presented in Fig. 7.1.

A Full-depth release is considered in this numerical study and the initial aspect ratio of the lock fluid is equal to $R = H/x_0 = 0.4$. The Grashof number is equal to 115000 and the sediment characteristics are the same with those considered for case A in Table 6.1.

7.2 Results

According to the conclusion drawn in the previous chapter, the propagation of the gravity current above a mobile bed leads to the bed material entrainment. This process is expected to generate bed deformations due to scour, when the gravity current flows over the mobile bed. On the other hand,

downstream the mobile bed, bed forms are expected to be generated due
to deposition of the entrained material. In this section, the instantaneous
bed contours, above and downstream the mobile reach of the bed are pre-
sented. Furthermore, the feedback of the bed deformation on the flow field
is analyzed.

7.2.1 Scouring

The bed contour at two different time instants, in which the head of the
current is propagating over the mobile bed are illustrated in Fig. 7.2. These
contours have been amplified for visualization purposes and t_{probe} illustrates
the time instant in which the front of the current arrives at the mobile bed.
The observed bed forms follow a streaky pattern similar to that discussed in
Sec. 6.4.6. As it has been mentioned, this pattern correlates with the lobes
and clefts instabilities present in the front of the current. Moreover, these
results show that the evolution of the current above the mobile reach of the
bed increases the observed scour, however the shape of the bed deformation
does not change significantly. Fig. 7.2 can also confirmed the assumption
made in the previous chapter according to which the particle deposition plays
a minor role above the mobile reach of the bed. In particular, the positive
elevation of the bed in this section is almost two orders of magnitude lower
than scour. Thus, the sediment is entrained above the mobile reach of the
bed then advected downstream by the flow.

The time evolution of the bed profile in the zy plane for a specific stream-
wise position is plotted in Fig. 7.3. The chosen streamwise position is equal
to $x/H = 6$, that roughly corresponds to the middle length of the mobile
bed. $t' = 0$ corresponds to the time instant when the front of the current
arrives in this position. At that moment the bed is flat. As the current
propagates downstream, scour streaks start to appear and this scour pat-
tern does not changes significantly with time. What is changing is the total
elevation of the profile. However, it is worth noting that the bed is eroded
faster in the time period $0 - 4$ than in the time period $4 - 6$. Thus, ac-
cording to the conclusions drawn in the previous chapter, it can be assumed
that in the time period $0 - 4$ the head of the current passes over the loca-
tion $x/H = 6$. The maximum scour observed in Fig. 7.3 at time $t' = 6$ is
around $\Delta y/H = 0.004$ that corresponds to the 0.4% of the total height of the
flume. It should be noted here that at time instant $t' = 6$ the current is still
propagating above the mobile bed. This means that the scour may slightly
increase. However, as it has been mentioned above, the body of the current
does not significantly change the bed deformation. Assuming that the height
of the current is roughly equal to $0.5H$, then the maximum scour observed
corresponds to 0.8% of the current height. At the same section and at the
same time instant the average value of the scour is about $\Delta y/H = 0.0025$
that corresponds to 0.5% of the current height. These results indicate that
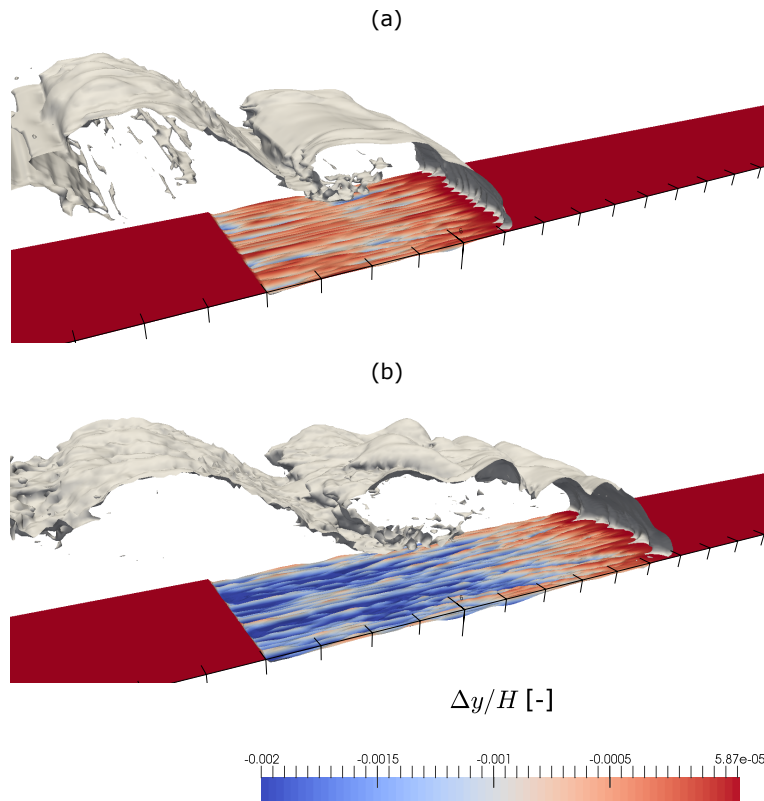
Figure 7.2: Bed deformation at two different time instants when the head of the current propagates above the mobile bed. a) corresponds to time instant $(t - t_{\text{probe}})/t^* = 2$ s and b) to $(t - t_{\text{probe}})/t^* = 4$ s
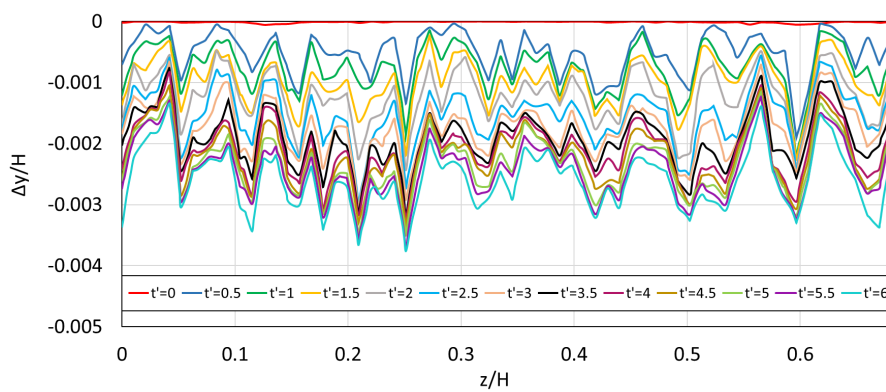
Figure 7.3: Time evolution of the bed profile, in the zy plane, at the streamwise position equal to $x/H = 6$. The time instant $t' = 0$ correspond to the moment that the front of the current arrives in this position.
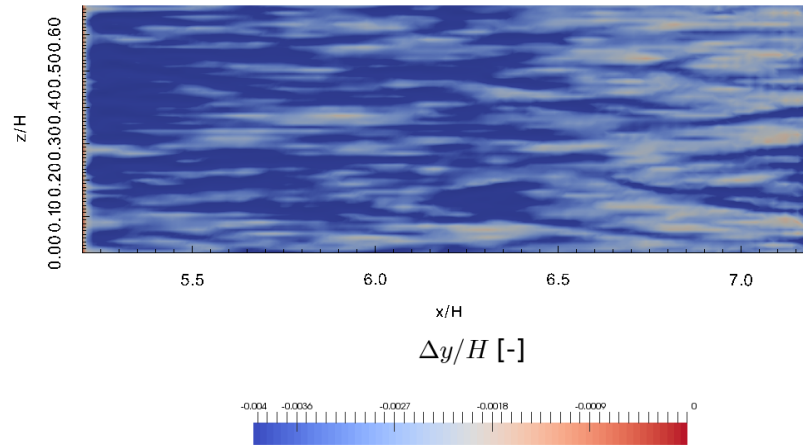
Figure 7.4: Bed deformation at the time instant equal to $t - t_{\text{probe}}/t^* = 10$ that the head of the current has passed the mobile reach of the bed.

the scour generated by a single event is relatively small and it is expected to have no influence on the flow field. This matter is going to be studied in the following section.

Finally, the bed contour of the mobile reach of the bed at time instant $t - t_{\text{probe}}/t^* = 10$ is presented in Fig. 7.4. Although the gravity current has not passed through the mobile reach of the bed, the morphology presented in Fig. 7.4 can be considered in equilibrium. This is due to the fact that, the part of the current that plays an important role on the bed scouring has already passed this region.

7.2.2   Flow field above the deformed bed

As mentioned before, the scour observed in the mobile reach of the bed due to the propagation of a single current is relatively small compared to the height of the flow and it is expected to not have any significant feedback on the coherence of the flow. To confirm this assumption the turbulent structures formed at the viscous sublayer above the mobile reach of the bed are shown in Fig. 7.5. These results indicate that there is not any visible difference between the structures formed above and upstream the mobile reach of the bed. This means that the slight deformation of the mobile bed offers little modulation on the flow structures. This is in accordance with the observations of [121].

Moreover, the velocity field over the deformed bed is plotted in Fig. 7.6. In this case, it can be noted that the velocity distribution is modulated by the presence of the scour and the streamwise streaks of high and low velocity have been shortened. However, overall picture has not changed.

Figure 7.5: Turbulent structures in the flow sublayer above the mobile reach of the bed at the time instant $t - t_{\mathrm{probe}}/t^* = 4$.

Figure 7.6: Streamwise velocity contour above the mobile reach of the bed at the time instant $t - t_{\mathrm{probe}}/t^* = 4$.

7.2.3 Deposition

In this section the bed deformation due to the sediment deposition downstream to the mobile reach of the bed is analyzed. The bed elevation is presented in Fig. 7.7(a). Higher values of positive bed elevation that covers the who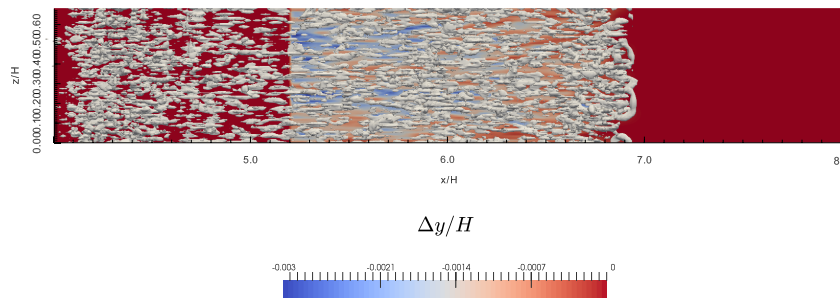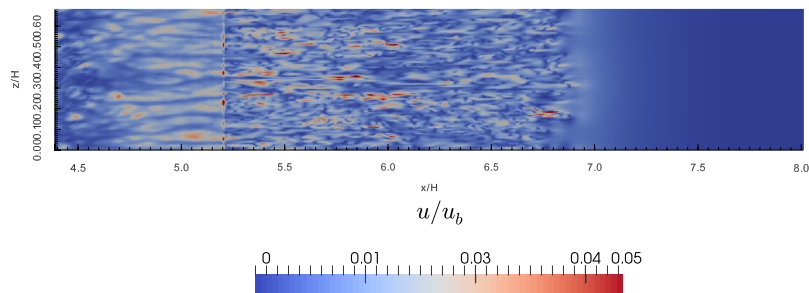le width of the channel are observed in the region directly downstream of the mobile bed (from $x/H = 7.2$ to $x/H = 7.5$). This is due to the small jump between the eroded section and the flat bed. After this region the sediment deposition also follows a streaky pattern. It is noteworthy to mention that also in this part the bed deformation due to sediment deposition is quite small. As it has been mentioned in Ch. 1.2.1, gravity currents are able to transport sediment at considerable distances from their initial location.

The sediment deposition downstream of the streamwise position $x/H = 7.5$ can be related to low-speed streaks of streamwise velocity. The contour plot of the instantaneous streamwise velocity distribution close to the bed is shown in Fig. 7.7(b). To ease this comparison the bed elevation has been plotted in Fig. 7.8 along with the streamwise velocity iso-contours equal to $u/u_{\mathrm{b}} = 0.02$. Specifically, these iso-contours enclose the areas where the streamwise velocity is higher than $u/u_{\mathrm{b}} = 0.02$. In these low-speed regions the velocity conditions can not counteract the falling velocity of the particles, so sediment deposition occurs.

Finally, Fig. 7.9 shows the streamwise vorticity close to the of the bed downstream of the mobile reach. The black lines shown in the same figure correspond to the bed isoypses. These results indicate that bed valleys are correlated to positive vorticity, whereas mountains are related to negative vorticity. As shown in Fig. 7.10 negative vorticity is connected to clockwise motion of the flow and positive vorticity to anticlockwise motion. Thus, in the regions where the vorticity obtains negative values the suspended sediment are forced by the flow to move downwards and are deposited in the low-speed region. On the other hand, in regions that vorticity is positive the sediment are moving upwards into suspension.

7.2.4 Conclusions

In this chapter a three-dimensional LES of a high Grashof salinity current propagating over a deformable bed has been performed, using the fully coupled hydro-morphodynamic model implemented in this thesis. Bed deformation due to erosion is allowed only over a part of the bed, whereas in the remaining domain bed deformation is created only due to deposition. The aim of this simulation is to provide a detailed description and analysis of the different processes (scour and deposition) induced by such flows. Moreover, the flow field above the deformed bed is presented.

The first part of the chapter deals with the scour of the mobile reach
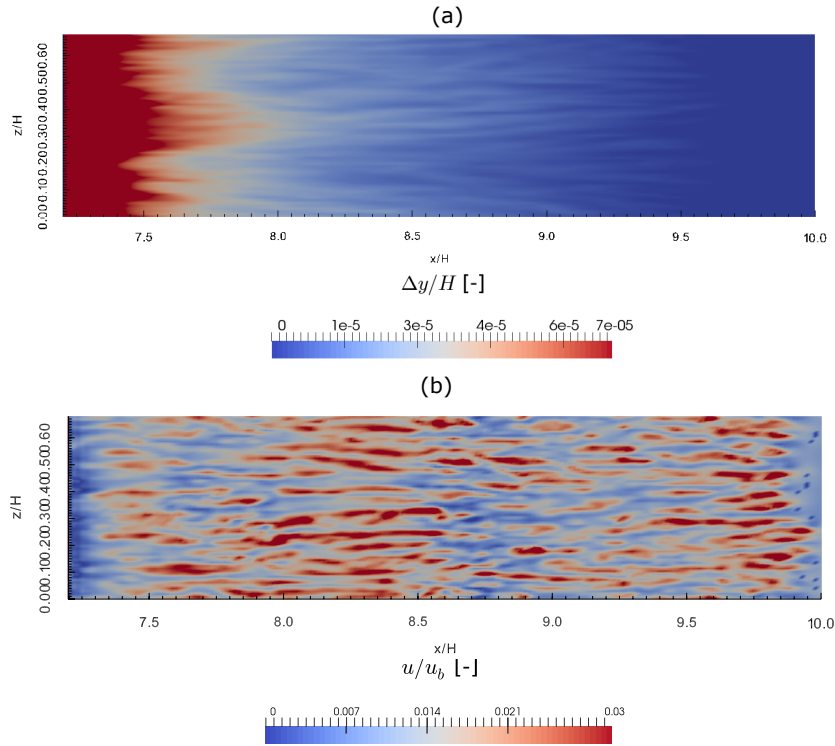
Figure 7.7: (a) Bed elevation and (b) Streamwise velocity contour on the bed interface, at the part downstream the mobile reach of the bed at the time instant equal to $t - t_{\mathrm{probe}}/t^* = 10$.
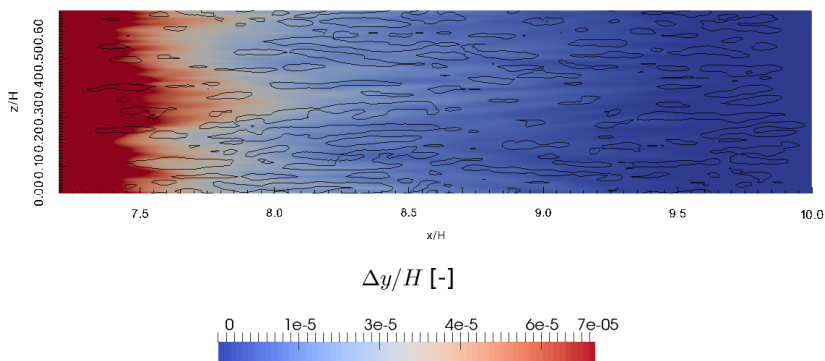
Figure 7.8: Bed elevation along with the streamwise velocity iso-contour equal to $u/u_{\mathrm{b}} = 0.02$ at the part downstream the mobile reach of the bed at the time instant equal to $t - t_{\mathrm{probe}}/t^* = 10$.
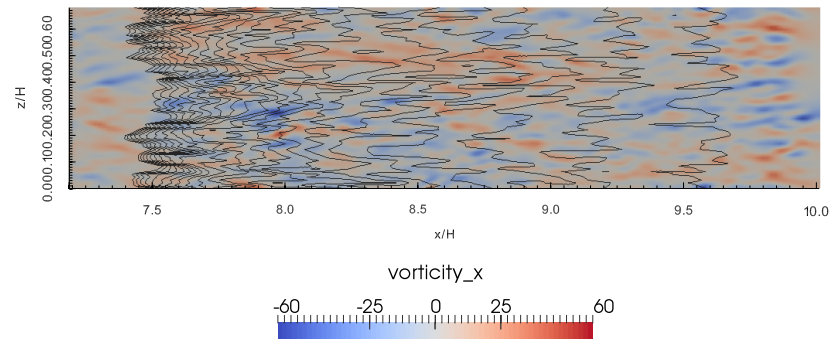
Figure 7.9: Streamwise vorticity contour in the part downstream the mobile section of the bed, at the time instant $t - t_{\text{probe}}/t^* = 10$. The solid lines indicate the bed isohypses.
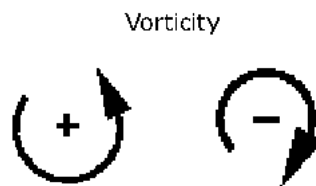
Figure 7.10: Sketch that demonstrate the meaning of positive and negative vorticity.

of the bed. Instantaneous contour plots of the bed elevation and the time evolution of the bed deformation in a specific section are presented. These results indicate that the scour patter correlates with the lobe and clefts instabilities of the front of the current and follows a streaky distribution. Moreover, it is observed that the mobile reach of the bed is mainly deformed by the head of the current while the body of the current does not significantly change the bed elevation. This observation is in accordance with the conclusions drawn in the previous chapter. The turbulent structures formed in the viscous sublayer of the flow point out that the bed deformation is small compared to the scale of the flow and does not influence the coherence of the flow. This conclusion enforce the assumption made in the previous chapter with respect to the fixed boundary condition.

In the second part of the chapter, the sediment deposition downstream of the mobile reach of the bed is examined. The areas where deposition is observed are characterized by low-speed velocity and negative streamwise vorticity. Specifically, particles are forced to move downstream due to the negative vorticity of the flow and settle in the areas in which the flow conditions are not able to counteract their settling velocity. It is worth-noting that the bed deformation due to deposition is relatively small, which means that the flow is able to carry sediment into suspension for long distances.

Chapter 8

Conclusions

This thesis is focused on the numerical simulation of sediment transport processes induced by gravity currents propagating over erodible beds. The objective is to improve the understanding of flow-sediment and flow-bed interaction in buoyancy driven flows. The numerical model used stems from the coupling between the Large Eddy Simulation and the Level-set method, and is able to reproduce suspended sediment transport problems with both stationary and moving boundaries. For the approximate representation of complex bed forms as flow boundaries the immersed boundary method is used, whereas the sediment exchange between the flow and the bed is represented by a Neumann boundary condition.

The implemented level-set method is numerically integrated using the forward Euler scheme in time and the space derivatives described in the curvilinear coordinate system, are linearized with a second order essentially non-oscillatory (ENO) scheme. To assess this implementation, the coupled hydro-moprhodynamic model is used to simulate the ripple migration problem, and the obtained results are compared with those reported in the work of Kraft et al. [62].

The first case studied in this thesis deals with the sediment entrainment induced by gravity currents. In particular, large eddy simulations of salinity currents propagating over a partially mobile bed have been performed. Four different simulations have been done varying the Grashof number of the current and the sediment diameter. However, the bed deformation of the mobile bed due to erosion and deposition processes for those cases has been considered negligible and stationary bottom boundaries have been used. The results obtained in this study have been validated against experimental data taken for the dynamics of the current and the sediment entrainement.

It was observed that sediment entrainment mainly occurs when the head of the current is propagating above the mobile section of the bed, whereas the body of the current is less important in terms of erosion. The entrained material is then advected downstream by the head. An analysis of the flow

field indicates that the features that are responsible for the motion of the bed material and its transport in the outer region of the flow are the highly intermittent vertical velocities, the excess bed shear stress peaks, and the increasing mixing provided by the turbulent structures formed close to the bed, behind the front of the current. The influence of the entrained sediment on the stability condition of the current is also studied. These results show that the suspended sediment concentration is relatively small and does not affect the current stratification. However, the stability conditions provided by the gravity current play an important role on the sediment distribution. Specifically, the stable stratification observed in the mixing interface between the heavier and the ambient fluid constrain the vertical distribution of the entrained material.

To analyze the evolution of the bed forms generated by gravity currents and examined their influence on the dynamic of the flow an additional case is simulated. This case makes use of the coupled hydro-morphodynamic model developed in this work. The simulated gravity current is considered to have a higher erosive capacity than the one considered in the previous study. Nevertheless, the characteristics of the sediment material are the same of the studied in Ch. 6. The time evolution of the deformable bed show that, at the mobile reach of the bed, settling plays a minor role and most of the deformation is due to erosion. The observed scour follows a streaky pattern that correlates with the lobe and cleft instabilities present in the front of the current. As expected, scour increases when the head of the current propagates above the mobile reach of the bed. The body of the current does not significantly influence the bed deformation. In this study, the bed deformation due to deposition is also studied downstream of the mobile reach of the bed. Although the bed elevation due to deposition is quite small, the generated bed forms can be related to low-speed velocity streaks and negative streamwise vorticity. Finally, it is indicated that the flow coherence is not strongly perturbed by the bed deformation induced by a single gravity current. These results confirm the assumption on the stationary boundaries made in the first study, that was also characterized by a lower Grashof number.

The results presented in this thesis aim to encourage the further exploration of sediment-laden flows over moving boundaries. It is worth noting here that the results presented in Ch. 7 are the first steps towards a deeper understanding of bed forms created by gravity currents. However, a wider range of simulations and longer simulation time could provide a better insight of the observed phenomena. Moreover, future work can be dedicated to the influence of the entrained material on the dynamic of the gravity current. This can be accomplished by simulating the propagation of the current over a mobile reach much longer than the one considered in this study and by changing the sediment characteristics (e.g. density, diameter). Another aspect that may be interesting to be further studied is the

bed deformation generated by gravity currents and its influence on the flow field after the occurrence of multiple events. Furthermore, the developed hydro-morphodynamic model works in a parallel environment, and therefore may be applied to study the topological changes due to sediment transport processes in large-scale systems, like river and lakes. With respect to the level-set method, the implementation of a higher order temporal discretization scheme (e.g., the Runge–Kutta method) can be considered in the future numerical developments.

Bibliography

[1] R. J. Angulo, M. C. Souza, and M. R. Lamour. Coastal Erosion Problems Induced by Dredging Activities in the Navigation Channel of Paranaguá and São Francisco do Sul Harbor , Southern Brazil. *Journal of Coastal Research*, 2004(39):1801–1803, 2006. ISSN 0749-0208.

[2] V. Armenio. Large Eddy Simulation in Hydraulic Engineering: Examples of Laboratory-Scale Numerical Experiments. *Journal of Hydraulic Engineeringau*, 143(11):1–19, 2017. doi: 10.1061/(ASCE)HY. 1943-7900.0001357.

[3] V. Armenio and S. Sarkar. An investigation of stably stratified turbulent channel flow using large-eddy simulation. *Journal of Fluid Mechanics*, 459(May):1–42, 2002. ISSN 0022-1120. doi: 10.1017/S0022112002007851.

[4] J. H. Baas, W. D. McCaffrey, P. D. W. Haughton, and C. Choux. Coupling between suspended sediment distribution and turbulence structure in a laboratory turbidity current. *Journal of Geophysical Research: Oceans*, 110(11):1–20, 2005. ISSN 21699291. doi: 10.1029/2004JC002668.

[5] R. A. Bagnold. *The Physics of Blown Sand and Desert Dunes Book by*. Courier Corporation, 1941.

[6] T. B. Benjamin. Gravity Currents and Related Phenomena. *Journal of Fluid Mechanics*, 31(2):209–248, 1967. ISSN 0022-1120. doi: 10.1017/S0022112068000133.

[7] F. Blanchette, M. Strauss, E. Meiburg, B. Kneller, and M. E. Glinsky. High-resolution numerical simulations of resuspending gravity currents: Conditions for self-sustainment. *Journal of Geophysical Research: Oceans*, 110(12):1–15, 2005. ISSN 21699291. doi: 10.1029/2005JC002927.

[8] R. T. Bonnecaze, H. E. Huppert, and J. R. Lister. Particle-driven gravity currents. *Journal of Fluid Mechanics*, 250:339–369, 1993.

[9] M. Burkow and M. Griebel. A full three dimensional numerical simulation of the sediment transport and the scouring at a rectangular obstacle. *Computers and Fluids*, 125(1307):1–10, 2014.

[10] R. Canelas, J. Murillo, and R. Ferreira. Two-dimensional depth-averaged modelling of dam-break flows over mobile beds. *Journal of Hydraulic Research*, 51(4):392–407, 2013.

[11] M. I. Cantero, S. Balachandar, Marcelo H. García, and David Bock. Turbulent structures in planar gravity currents and their influence on the flow dynamics. *Journal of Geophysical Research: Oceans*, 113(8): 1–22, 2008. ISSN 21699291. doi: 10.1029/2007JC004645.

[12] M. I. Cantero, S. Balachandar, A. Cantelli, C. Pirmez, and G. Parker. Turbidity current with a roof: Direct numerical simulation of self-stratified turbulent channel flow driven by suspended sediment. *Journal of Geophysical Research: Oceans*, 114(3):1–20, 2009. ISSN 21699291. doi: 10.1029/2008JC004978.

[13] M. I. Cantero, S. Balachandar, and Gary Parker. Direct numerical simulation of stratification effects in a sediment-laden turbulent channel flow. *Journal of Turbulence*, 10(November 2014):1–28, 2009. ISSN 14685248. doi: 10.1080/14685240903159197.

[14] C. Chan-braun. *Turbulent open channel flow , sediment erosion and sediment transport*. KIT Scientific Publishing, 2012. ISBN 9783866449008.

[15] Y .C. Chang, T. Y. Hou, B. Merriman, and S. Osher. A Level set formulation of Eulerian interface capturing methods for incompressible fluid flows. *Journal of Computational Physics*, 124(2):449–464, 1996. ISSN 0021-9991. doi: http://dx.doi.org/10.1006/jcph.1996.0072.

[16] Y. S. Chang and A. Scotti. Modeling unsteady turbulent flows over ripples: Reynolds-averaged Navier-Stokes equations (RANS) versus large-eddy simulation (LES). *Journal of Geophysical Research C: Oceans*, 109(9):1–16, 2004. ISSN 01480227. doi: 10.1029/2003JC002208.

[17] A. J. Chorin. A numerical method for solving incompressible viscous flow problems. *Journal of Computanional Physics*, 2(12), 1967.

[18] Y. Chou and O. B. Fringer. Modeling dilute sediment suspension using large-eddy simulation with a dynamic mixed model. *Physics of Fluids*, 20(11):1–13, 2008. ISSN 10706631. doi: 10.1063/1.3005863.

[19] G. Constantinescu. LES of lock-exchange compositional gravity currents: A brief review of some recent results. *Environmental Fluid Mechanics*, 14(2):295–317, 2014. ISSN 15677419. doi: 10.1007/s10652-013-9289-0.

[20] R. Cossu and M. G. Wells. A comparison of the shear stress distribution in the bottom boundary layer of experimental density and turbidity currents. *European Journal of Mechanics, B/Fluids*, 32(1): 70–79, 2012. ISSN 09977546. doi: 10.1016/j.euromechflu.2011.09.006.

[21] M. Dallali and V. Armenio. Large eddy simulation of two-way coupling sediment transport. *Advances in Water Resources*, 81(December):33–44, 2015. ISSN 03091708. doi: 10.1016/j.advwatres.2014.12.004.

[22] Deltares. *Delft3D-Flow User's Manual*. Deltares, 2014.

[23] B. Dewals, F. Rulot, S. Erpicum, Archambeau P., , and M. Pirotton. *Advanced Topics in Sediment Transport Modelling: Non-alluvial Beds and Hyperconcentrated Flows*. In Sediment Transport. InTech., 2011. ISBN 9789537619824. doi: 10.5772/50570.

[24] DHI. *MIKE 21 short description*. 1993.

[25] I. Eames, A. J. Hogg, S. Gething, and S. B. Dalziel. Resuspension by saline and particle-driven gravity currents. *Journal of Geophysical Research-Oceans*, 106(7):14,14–95,111, 2001. ISSN 21699291. doi: 10.1029/2000jc900146.

[26] S. Elghobashi and G. C. Truesdell. Direct simulation of particle dispersion in a decaying isotropic turbulence. *Journal of Fluid Mechanics*, 242:655–700, 1992. ISSN 0022-1120. doi: 10.1017/S0022112092002532.

[27] C. Escauriaza and F. Sotiropoulos. Initial stages of erosion and bed form development in a turbulent flow around a cylindrical pier. *Journal of Geophysical Research: Earth Surface*, 116(3):1–24, 2011. ISSN 21699011. doi: 10.1029/2010JF001749.

[28] E. A. Fadlun, R. Verzicco, P. Orlandi, and J. Mohd-Yusof. Combined Immersed-Boundary Finite-Difference Methods for Three-Dimensional Complex Flow Simulations. *Journal of Computational Physics*, 161(1): 35–60, 2000. ISSN 00219991. doi: 10.1006/jcph.2000.6484.

[29] R. M. Ferreira, M. A. Hassan, and C. Ferrer-Boix. Principles of bedload transport of non-cohesive sediment in open-channels. In *Rivers–Physical, Fluvial and Environmental Processes*, pages 323–372. Springer, Cham, 2015.

[30] A. T. Fragoso, M. D. Patterson, and J. S. Wettlaufer. Mixing in gravity currents. *Journal of Fluid Mechanics*, 734:R2, 2013. ISSN 0022-1120. doi: 10.1017/jfm.2013.475.

[31] M. J. Franca and U. Lemmin. Eliminating velocity aliasing in acoustic Doppler velocity profiler data. *Measurement Science and Technology*, 17(2):313–322, 2006. ISSN 0957-0233. doi: 10.1088/0957-0233/17/2/012.

[32] M. García. Sedimentation Engineering. *ASCE Manual of Practice*, 54 (110):1–1179, 2008. ISSN 07347685. doi: 10.1061/9780784408230.

[33] M. Garcia and G. Parker. Entrainment of bed sediment into suspension. *Journal of Hydraulic Engineering*, 117(4):414–435, 1991.

[34] M. Garcia and G. Parker. Experiments on the entrainment of sediment into suspension by a dense bottom current. *Journal of Geophysical Research*, 98:4793, 1993. ISSN 0148-0227. doi: 10.1029/92JC02404.

[35] M. Germano. Turbulence: the filtering approach. *Journal of Fluid Mechanics*, 238:325, 1992. ISSN 0022-1120. doi: 10.1017/S0022112092001733.

[36] M. Germano, U. Piomelli, P. Moin, and W. H. Cabot. A dynamic subgrid-scale eddy viscosity model. *Phys. Fluids A Fluid Dyn.*, 3(7): 1760, 1991. ISSN 08998213. doi: 10.1063/1.857955.

[37] D. Goldstein, R. Handler, and L. Sirovich. Modeling a No-Slip Flow Boundary with an External Force Field, 1993. ISSN 00219991.

[38] J. Gomes and O. Faugeras. Level Sets and Distance Functions. In *Computer Vision-ECCV*, pages 588–602., 2000.

[39] E. Gonzalez-Juez, E. Meiburg, T. Tokyay, and G. Constantinescu. Gravity current flow past a circular cylinder: forces, wall shear stresses and implications for scour. *Journal of Fluid Mechanics*, 649:69–102, 2010. ISSN 0022-1120. doi: 10.1017/S002211200999334X.

[40] W. H. Graf. *Hydraulics of sediment transport*. Water Resources Publication, 1984.

[41] B. P. Greimann and F. M. Holly. Two-phase flow analysis of concentration profiles. *Journal of Hydraulic Engineering*, 127(September): 753–762, 2001.

[42] B. P. Greimann, M. Muste, and F. M. Holly. Two-phase formulation of suspended sediment transport. *Journal of Hydraulic Research*, 37(4): 479–500, 1999. ISSN 0022-1686. doi: 10.1080/00221686.1999.9628264.

[43] J. Hacker, P. F. Linden, and S. B. Dalziel. Mixing in lock-release gravity currents. *Dynamics of Atmospheres and Oceans*, 24:183–195, 1996. ISSN 03770265. doi: 10.1016/0377-0265(95)00443-2.

[44] J. Hacker, P. F. Linden, and S. B. Dalziel. Mixing in lock-release gravity currents. *Dynamics of Atmospheres and Oceans*, 24(2013): 183–195, 1996. ISSN 03770265. doi: 10.1016/0377-0265(95)00443-2.

[45] M. A. Hallworth, H. E. Huppert, J. C. Phillips, and R. S. J. Sparks. Entrainment into two-dimensional and axisymmetric turbulent gravity currents. *Journal of Fluid Mechanics*, 308(1996):289–311, 1996. ISSN 00221120. doi: 10.1017/s0022112096001486.

[46] C. Härtel, E. Meiburg, and F. Necker. Analysis and direct numerical simulation of the flow at a gravity-current head. Part 1. Flow topology and front speed for slip and no-slip boundaries. *Journal of Fluid Mechanics*, 418:189–212, 2000. ISSN 00221120. doi: 10.1017/S0022112000001221.

[47] A. Harten, B. Engquist, S. Osher, and S. Chakravarthy. Uniformly high-order accurate essentially non-oscillatory schemes. *Journal of Computanional Physics*, 71:231–303, 1987.

[48] W. Haslinger. *Berechnung der turbulenten Strömung in einem welligen, offenen Gerinne mit Hilfe eines Mehrschichtenmodells.* PhD thesis, Technische Hochschule Darmstadt, Darmstadt, Germany, 1993.

[49] G. Hoffmann, M. M. Nasr-Azadani, and E. Meiburg. Sediment Wave Formation Caused by Erosional and Depositional Turbidity Currents: A Numerical Investigation. *Procedia IUTAM*, 15:26–33, 2015. ISSN 22109838. doi: 10.1016/j.piutam.2015.04.005.

[50] F. M. Holly and J.-L. Rahuel. New numerical/physical framework for mobile-bed modelling. *Journal of Hydraulic Research*, 28(4):401–416, 1990. ISSN 0022-1686. doi: 10.1080/00221689009499057.

[51] H. E. Huppert and J. E. Simpson. The slumping of gravity currents. *Journal of Fluid Mechanics*, 99(04):785, 1980. ISSN 0022-1120. doi: 10.1017/S0022112080000894.

[52] A. Iafrati, A. Di Mascio, and E. F. Campana. A level set technique applied to unsteady free surface flows. *International Journal for Numerical Methods in Fluids*, 35(3):281–297, 2001. ISSN 02712091. doi: 10.1002/1097-0363(20010215)35:3⟨281::AID-FLD91⟩3.0.CO;2-V.

[53] D. L. Inman, C. E. Nordstrom, and R. E. Flick. Currents in submarine canyons: An air-sea-land interaction. *Annual Review of Fluid Mechanics*, 8:275–310, 1976.

[54] M. Ito and T. Saito. Gravel Waves in an Ancient Canyon: Analogous Features and Formative Processes of Coarse-Grained Bedforms in a Submarine-Fan System, the Lower Pleistocene of the Boso Peninsula, Japan. *Journal of Sedimentary Research*, 76(12):1274–1283, 2006. ISSN 1527-1404. doi: 10.2110/jsr.2006.093.

[55] J. Jeong and F. Hussain. On the identification of a vortex. *Journal of Fluid Mechanics*, 285:69–94, 1995. doi: 10.1017/S0022112095000462.

[56] A. Khosronejad and F. Sotiropoulos. Numerical simulation of sand waves in a turbulent open channel flow. *Journal of Fluid Mechanics*, 753:150–216, 2014. doi: 10.1017/jfm.2014.335.

[57] A. Khosronejad, S. Kang, I. Borazjani, and F. Sotiropoulos. Curvilinear immersed boundary method for simulating coupled flow and bed morphodynamic interactions due to sediment transport phenomena. *Advances in Water Resources*, 34(7):829–843, 2011. ISSN 03091708. doi: 10.1016/j.advwatres.2011.02.017.

[58] B. Kneller and C. Buckee. The structure and fluid mechanics of turbidity currents: A review of some recent studies and their geological implications. *Sedimentology*, 47(SUPPL. 1):62–94, 2000. ISSN 00370746. doi: 10.1046/j.1365-3091.2000.047s1062.x.

[59] B. C. Kneller, S. J. Bennett, and W. D. McCaffrey. Velocity and turbulence structure of density currents and internal solitary waves: potential sediment transport and the formation of wave ripples in deep water. *Sedimentary Geology*, 112(3-4):235–250, 1997. ISSN 00370738. doi: 10.1016/S0037-0738(97)00031-6.

[60] B. C. Kneller, S. J. Bennett, and W. D. McCaffrey. Velocity structure, turbulence and fluid stresses in experimental gravity currents. *Journal of Geophysical Research*, 104(C3):5381, 1999. ISSN 0148-0227. doi: 10.1029/1998JC900077.

[61] J. Kowalski and J. N. McElwaine. Shallow two-component gravity-driven flows with vertical variation. *Journal of Fluid Mechanics*, 714: 434–462, 2013. ISSN 0022-1120. doi: 10.1017/jfm.2012.489.

[62] S. Kraft, Y. Wang, and M. Oberlack. Large Eddy Simulation of Sediment Deformation in a Turbulent Flow by Means of Level-Set Method. *Journal of Hydraulic Engineering*, 137(11):1394–1405, 2011. doi: 10.1061/(ASCE)HY.1943-7900.0000439.

[63] Y. Kubo and T. Nakajima. Laboratory experiments and numerical simulation of sediment-wave formation by turbidity currents. *Marine Geology*, 192(1-3):105–121, 2002. ISSN 00253227. doi: 10.1016/S0025-3227(02)00551-0.

[64] A. Landsberg, A. Chtchelkanova, C. Lind, J. Boris, and T. Young. FAST3D user and programmer reference manual. Technical report, University of Karlsruhe, 1998.

[65] U. Lemmin and T. Rolland. Acoustic velocity profiler for laboratory and field studies. *Journal of Hydraulic Engineering*, 123(12):1089–1098, 1997.

[66] B. P. Leonard. A stable and accurate convective modelling procedure based on quadratic upstreaminterpolation. *Computer methods in applied mechanics and engineering*, 19:59–98, 1979.

[67] A. Leonardi, F. K. Wittel, M. Mendoza, and H. J. Herrmann. Coupled DEM-LBM method for the free-surface simulation of heterogeneous suspensions. *Computational Particle Mechanics*, 1(1):3–13, 2014. ISSN 2196-4378. doi: 10.1007/s40571-014-0001-z.

[68] D. Liang, L. Cheng, and F. Li. Numerical modeling of flow and scour below a pipeline in currents. Part II. Scour simulation. *Coastal Engineering*, 52(1):43–62, 2005. ISSN 03783839. doi: 10.1016/j.coastaleng.2004.09.001.

[69] D. K. Lilly. A proposed modification of the Germano subgrid-scale closure method. *Physics of Fluids A: Fluid Dynamics*, 4(3):633–635, 1992. ISSN 0899-8213. doi: 10.1063/1.858280.

[70] X. Liu and M. H. García. Three-Dimensional Numerical Model with Free Water Surface and Mesh Deformation for Local Sediment Scour. *Journal of Waterway, Port, Coastal, and Ocean Engineering*, 134(4):203–217, 2008. ISSN 0733-950X. doi: 10.1061/(ASCE)0733-950X(2008)134:4(203).

[71] F. R. Luque and R. Van Beek. Erosion And Transport Of Bed-Load Sediment. *Journal of Hydraulic Research*, 14(October 2014):127–144, 1976. ISSN 0022-1686. doi: 10.1080/00221687609499677.

[72] R. Manica. Sediment Gravity Flows: Study Based on Experimental Simulations. *Hydrodynamics - Natural Water Bodies cdn.intechopen.com*, page 286, 2012. ISSN 978-953-307-893-9. doi: 10.5772/1352.

[73] M. Mattioli, J. M. Alsina, A. Mancinelli, M. Miozzi, and M. Brocchini. Experimental investigation of the nearbed dynamics around a submarine pipeline laying on different types of seabed: The interaction between turbulent structures and particles. *Advances in Water Resources*, 48:31–46, 2012. ISSN 03091708. doi: 10.1016/j.advwatres.2012.04.010.

[74] P. McLaren and D. I. Little. The effects of sediment transport on contaminant dispersal: An example from Milford Haven. *Marine Pollution Bulletin*, 18(11):586–594, 1987. ISSN 0025326X. doi: 10.1016/0025-326X(87)90278-5.

[75] E. Meiburg and B. Kneller. Turbidity Currents and Their Deposits. *Annual Review of Fluid Mechanics*, 42(1):135–156, 2010. ISSN 0066-4189. doi: 10.1146/annurev-fluid-121108-145618.

[76] E. Meiburg, S. Radhakrishnan, and M. Nasr-Azadani. Modeling Gravity and Turbidity Currents: Computational Approaches and Challenges. *Applied Mechanics Reviews*, 67(4):040802, 2015. ISSN 0003-6900. doi: 10.1115/1.4031040.

[77] C. Meneveau, T.S. Lund, and W.H. Cabot. A Lagrangian dynamic subgrid-scale model of turbulence, 1996.

[78] E. Meyer-Peter and R. Muller. Formulas for bed-load transport. In *IAHSR 2nd meeting, Stockholm, appendix 2. IAHR*, 1948.

[79] G. V. Middleton and J. B. Southard. *Mechanics of sediment movement*. Society of Economic Paleontologists and Mineralogists, 1984.

[80] C. Min. On reinitializing level set functions. *Journal of Computational Physics*, 229(8):2764–2772, 2010. ISSN 00219991. doi: 10.1016/j.jcp.2009.12.032.

[81] B. Minh Duc, T. Wenka, and W. Rodi. Depth-averaged numerical modeling of flow and sediment transport in Elbe river. In *Erd International conference on Hydrosience and Engineering, Berlin*, 1998.

[82] R. Mittal and G. Iaccarino. Immersed Boundary Methods. *Annual Review of Fluid Mechanics*, 37(1):239–261, 2005. ISSN 0066-4189. doi: 10.1146/annurev.fluid.37.061903.175743.

[83] J. Mohd-Yusof. *Combined immersed boudaries/B-splines methods for simulations in complex geometries*. CTR Annual Research Briefs, NASA Ames, 1997.

[84] M. Muste, K. Yu, I. Fujita, and R. Ettema. Two-phase versus mixed-flow perspective on suspended sediment transport in turbulent channel flows. *Water Resources Research*, 41(10), 2005. ISSN 00431397. doi: 10.1029/2004WR003595.

[85] F. Necker, C. Härtel, L. Kleiser, and E. Meiburg. High-resolution simulations of particle-driven gravity currents. *International Journal of Multiphase Flow*, 28(2):279–300, 2002. ISSN 03019322. doi: 10.1016/S0301-9322(01)00065-9.

[86] F. Necker, C. Härtel, L. Kleiser, and E. Meiburg. Mixing and dissipation in particle-driven gravity currents. *J. Fluid. Mech.*, 545(-1): 339–372, 2005. ISSN 0022-1120. doi: 10.1017/S0022112005006932.

[87] Y. Niño and M. García. Using Lagrangian particle saltation observations for bedload sediment transport modelling. *Hydrological Processes*, 12(8):1197–1218, 1998. ISSN 08856087. doi: 10.1002/(SICI) 1099-1085(19980630)12:8⟨1197::AID-HYP612⟩3.0.CO;2-U.

[88] Y. Niño and M. H. Garcia. Experiments on particle-turbulence interactions in the near-wall region of an open channel flow: implications for sediment transport. *Journal of Fluid Mechanics*, 326:285–319, 1996. ISSN 0022-1120. doi: 10.1017/S0022112096008324.

[89] H. I. S. Nogueira, C. Adduce, El. Alves, and M. J. Franca. Analysis of lock-exchange gravity currents over smooth and rough beds. *Journal of Hydraulic Research*, 51(4):417–431, 2013. ISSN 0022-1686. doi: 10.1080/00221686.2013.798363.

[90] H. I.S. Nogueira, C. Adduce, E. Alves, and M. J. Franca. Dynamics of the head of gravity currents. *Environmental Fluid Mechanics*, 14 (2):519–540, 2014. ISSN 15677419. doi: 10.1007/s10652-013-9315-2.

[91] S. K. Ooi. *High resolution numerical simulations of lock- exchange gravity-driven flows.* PhD thesis, University of Iowa, 2006.

[92] S. K. Ooi, G. Constantinescu, and L. Weber. Numerical simulations of lock-exchange compositional gravity current. *Journal of Fluid Mechanics*, 635(2009):361, 2009. ISSN 0022-1120. doi: 10.1017/ S0022112009007599.

[93] S. Osher and J. A. Sethian. Fronts propagating with curvature-dependent speed: Algorithms based on Hamilton-Jacobi formulations. *Journal of Computational Physics*, 79(1):12–49, 1988. ISSN 10902716. doi: 10.1016/0021-9991(88)90002-2.

[94] L. Ottolenghi, C. Adduce, R. Inghilesi, F. Roman, and V. Armenio. Mixing in lock-release gravity currents propagating up a slope. *Physics of Fluids*, 28(5), 2016. ISSN 10897666. doi: 10.1063/1.4948760.

[95] L. Ottolenghi, C. Adduce, F. Roman, and V. Armenio. Analysis of the flow in gravity currents propagation up a slope. *Ocean Modelling*, 115:1–13, 2017.

[96] A. Papanicolaou, A. Bdour, and E. Wicklein. A numerical model for the study of sediment transport in steep mountian streams. *Journal of Hydraulic Research*, 42(4):357–366, 2004.

[97] A. N. Papanicolaou and B. D. Barkdoll. *Sediment Dynamics upon Dam Removal.* American Society of Civil Engineers, 2011. ISBN 9780784411360.

[98] A. N. Papanicolaou, G. Krallis, and J. Edinger. Sediment Transport Modeling Review — Current and. *Journal of Hydraulic Engineering*, 134(January):1–14, 2008.

[99] G. Parker, Y. Fukushima, and M. H. Pantin. Self-accelerating turbidity currents. *J. Fluid. Mech.*, 171:145–181, 1986.

[100] G. Parker, M. Garcia, Y. Fukushima, and W. Yu. Experiments on turbidity currents over an erodible bed Experiments on turbidity currents over an erodible bed. *Journal of Hydraulic Research*, 25(February): 123–147, 1987. ISSN 0022-1686. doi: 10.1080/00221688709499292.

[101] J. Parsons and M. Garcia. Similarity of gravity current fronts. *Physics of Fluids*, 10(12):3209–3213, 1998. ISSN 10706631.

[102] D. Peng, B. Merriman, S. Osher, H. Zhao, and M. Kang. A PDE-Based Fast Local Level Set Method. *Journal of Computational Physics*, 155 (2):410–438, 1999. ISSN 00219991. doi: 10.1006/jcph.1999.6345.

[103] C. S. Peskin. Numerical analysis of blood flow in the heart. *Journal of computational physics*, 25(3):220–252, 1977.

[104] U. Piomelli. Large-eddy and direct simulation of turbulent flows. Technical report, Lecture series-van Kareman Institute for fluid dynamics, 2000.

[105] D. J. W. Piper and B. Savoye. Processes of late Quaternary turbidity current flow and deposition on the Var deep-sea fan, northwest Mediterranean Sea. *Sedimentology*, 40(3):557–582, 1993. ISSN 13653091. doi: 10.1111/j.1365-3091.1993.tb01350.x.

[106] S.B. Pope. *Turbulent flows.* Cambridge univeristy press, 2000. ISBN 0521598869. doi: 10.1017/CBO9780511840531.

[107] L. J. Prendergast and K. Gavin. Journal of Rock Mechanics and Geotechnical Engineering A review of bridge scour monitoring techniques. *Journal of Rock Mechanics and Geotechnical Engineering*, 6 (2):138–149, 2014. ISSN 1674-7755. doi: 10.1016/j.jrmge.2014.01.007.

[108] J. F. Richardson and W. N. Zaki. The sedimentation of a suspension of uniform spheres under conditions of viscous flow. *Chemical Engineering Science*, 3(2):65–73, 1954.

[109] W. Rodi. Comparison of LES and RANS calculations of the flow around bluff bodies. *Journal of Wind Engineering and Industrial Aerodynamics*, 69-71:55–75, 1997. ISSN 01676105. doi: 10.1016/ S0167-6105(97)00147-5.

[110] F. Roman, E. Napoli, B. Milici, and V. Armenio. An improved immersed boundary method for curvilinear grids. *Computers and Fluids*, 38(8):1510–1527, 2009. ISSN 00457930. doi: 10.1016/j.compfluid.2008. 12.004.

[111] F. Roman, G. Stipcich, V. Armenio, R. Inghilesi, and S. Corsini. Large eddy simulation of mixing in coastal areas. *International Journal of Heat and Fluid Flow*, 31(3):327–341, 2010. ISSN 0142727X. doi: 10. 1016/j.ijheatfluidflow.2010.02.006.

[112] J. W. Rottman and J. E. Simpson. Gravity currents produced by instantaneous releases of a heavy fluid in a rectangular channel. *Journal of Fluid Mechanics*, 135:95–110, 1983. ISSN 00221120. doi: 10.1017/S0022112083002979.

[113] H. Rouse. Modern Conceptions of the Mechanics of Fluid Turbulence. *Trans. ASCE*, 102:463–543, 1937.

[114] A. Ruffman and V. Hann. The Newfoundland Tsunami of November 18 , 1929 : An Examination of the Twenty-eight Deaths of the " South Coast Disaster ". *Newfoundland and Labrador Studies*, 21(1): 1719–1726, 2006.

[115] A. A. Salehi Neyshabouri, A. M. Ferreire Da Suva, and R. Barron. Numerical simulation of scour by a free falling jet. *Journal of Hydraulic Research*, 41(5):533–539, 2003. ISSN 0022-1686. doi: 10.1080/00221680309499998.

[116] M. A. Santo, M. Toffolon, G. Zanier, L. Giovannini, and V. Armenio. Large eddy simulation (LES) of wind-driven circulation in a peri-alpine lake: Detection of turbulent structures and implications of a complex surrounding orography. *Journal of Geophysical Research : Oceans*, 122:2050–2068, 2017. ISSN 21699275. doi: 10.1002/2016JC012115. Received.

[117] M. Saud Afzal, H. Bihs, A. Kamath, and O. A. Arntsen. Three-Dimensional Numerical Modeling of Pier Scour Under Current and Waves Using Level-Set Method. *Journal of Offshore Mechanics and Arctic Engineering*, 137(3):032001, 2015. ISSN 0892-7219. doi: 10. 1115/1.4029999.

[118] J. Savioli and P. Justesen. Sediment in oscillatory flows over a plane bed. *Journal of Hydraulic Research*, 35(2):37–41, 1997. ISSN 0022-1686. doi: 10.1080/00221689709498425.

[119] A. J. Schleiss, M. J. Franca, C. Juez, and G. De Cesare. Reservoir sedimentation. *Journal of Hydraulic Research*, 54(6):595–614, 2016. ISSN 0022-1686. doi: 10.1080/00221686.2016.1225320.

[120] M. W. Schmeeckle. Numerical simulation of turbulence and sediment transport of medium sand. *Journal of Geophysical Research: Earth Surface*, 119(6):1240–1262, 2014. ISSN 21699011. doi: 10.1002/2013JF002911.

[121] O. E. Sequeiros, B. Spinewine, R. T. Beaubouef, T. Sun, M. H. García, and G. Parker. Characteristics of Velocity and Excess Density Profiles of Saline Underflows and Turbidity Currents Flowing over a Mobile Bed. *Journal of Hydraulic Engineering*, 136(7):412–433, 2010. ISSN 0733-9429. doi: 10.1061/(ASCE)HY.1943-7900.0000200.

[122] O. E. Sequeiros, B. Spinewine, R. T. Beaubouef, T. Sun, M. H. Garcia, and G. Parker. Bedload transport and bed resistance associated with density and turbidity currents. *Sedimentology*, 57(6):1463–1490, 2010. ISSN 00370746. doi: 10.1111/j.1365-3091.2010.01152.x.

[123] J. A. Sethian and P. Smereka. Level set methods for fluid interfaces. *Annual Review of Fluid Mechanics*, 35(1):341–372, 2003. ISSN 0066-4189. doi: 10.1146/annurev.fluid.35.101101.161105.

[124] A. Shields. *Application of Similarity Principles and Turbulence Research to Bed-Load Movement*. PhD thesis, California Institute of Technology, 1936.

[125] C. Shu. Efficient implementation of essentially non-oscillatory shock capturing schemes. *Journal of Computanional Physics*, 83:32–78, 1989.

[126] J. E. Simpson. Effects of the lower boundary on the head of a gravity current. *Journal of Fluid Mechanics*, 53(04):759–768, 1972. ISSN 0022-1120. doi: 10.1017/S0022112072000461.

[127] J. E. Simpson. Gravity currents in the laboratory, atmosphere, and ocean. *Annual Review of Fluid Mechanics*, 14(Hoult 1972):213–234, 1982. ISSN 0066-4189. doi: 10.1146/annurev.fl.14.010182.001241.

[128] J. E. Simpson. *Gravity currents: In the environment and the laboratory*. Campridge university press, 1997.

[129] J. E. Simpson and R. E. Britter. Dynamics of the Head of a Gravity Current Advancing Over a Horizontal Surface. *Journal of Fluid Mechanics*, 94(pt 3):477–495, 1979. ISSN 0022-1120. doi: -.

[130] J. D. Smith and S. R. McLean. Spatially Averaged Flow Over a Wavy Surface. *Journal of Geophysical Research*, 82(12), 1977.

[131] S. Soares-Frazo, R. Canelas, Z. Cao, L. Cea, H. M. Chaudhry, Andres Die Moran, Kamal El Kadi, R. Ferreira, I. F. Cadórniga, N. Gonzalez-Ramirez, M. Greco, W. Huang, J. Imran, J. Le Coz, R. Marsooli, A. Paquier, G. Pender, M. Pontillo, J. Puertas, B. Spinewine, C. Swartenbroekx, R. Tsubaki, C. Villaret, W. Wu, Z. Yue, and Y. Zech. Dam-break flows over mobile beds: Experiments and benchmark tests for numerical models. *Journal of Hydraulic Research*, 50(4): 364–375, 2012. ISSN 00221686. doi: 10.1080/00221686.2012.689682.

[132] A. Soldati and C. Marchioli. Sediment transport in steady turbulent boundary layers: Potentials, limitations, and perspectives for Lagrangian tracking in DNS and LES. *Advances in Water Resources*, 48: 18–30, 2012. ISSN 03091708. doi: 10.1016/j.advwatres.2012.05.011.

[133] B. Spinewine, O. E. Sequeiros, M. H. Garcia, R. T. Beaubouef, T. Sun, B. Savoye, and G. Parker. Experiments on Wedge-Shaped Deep Sea Sedimentary Deposits in Minibasins and/or on Channel Levees Emplaced by Turbidity Currents. Part II. Morphodynamic Evolution of the Wedge and of the Associated Bedforms. *Journal of Sedimentary Research*, 79(8):608–628, 2009. ISSN 1527-1404. doi: 10.2110/jsr.2009.065.

[134] M. Sussman, P. Smereka, and S. Osher. A Level Set Approach for Computing Solutions to Incompressible Two-Phase Flow, 1994. ISSN 00219991.

[135] D. V. Swenson and A. R. Ingraffea. The collapse of the Schoharie Creek Bridge : a case study in concrete fracture mechanics. *International Journal of Fracture*, 51:73–92, 1991.

[136] R. Temam. Remark on the pressure boundary condition for the projection method. *Theoretical and Computational Fluid Dynamics 3.3*, pages 181–184, 1991.

[137] W.A. Thomas and A.I. Prashum. Mathematical model of scour and deposition. *Journal of hydraulic division*, 110(11):1613–1641, 1977.

[138] P. D. Thome, A. G. Davies, and P. S. Belll. Observations and analysis of sediment diffusivity profiles over sandy rippled beds under waves. *Journal of Geophysical Research: Oceans*, 114(2):1–16, 2009. ISSN 21699291. doi: 10.1029/2008JC004944.

[139] S. Tjerry and J. Fredsøe. Calculation of dune morphology. *Journal of Geophysical Research: Earth Surface*, 110(4), 2005. ISSN 21699011. doi: 10.1029/2004JF000171.

[140] T. Tokyay, G. Constantinescu, and E. Meiburg. Lock-exchange gravity currents with a low volume of release propagating over an array of obstacles. *Journal of Geophysical Research: Oceans*, 119(5):2752–2768, 2014. ISSN 21699291. doi: 10.1002/2013JC009721.

[141] J. S. Turner. *Buoyancy effects in fluids.* Cambridge at the univeristy press, 1973.

[142] M. Ungarish. *An Introduction to Gravity Currents and Intrusions.* CRC press, 2009. ISBN 978-1-58488-903-8. doi: 10.1201/9781584889045.

[143] L. C. Van Rijn. Sediment transport part I: bed load transport. *Journal of Hydraulic Engineering*, 110(10):1431–1456, 1984. ISSN 0733-9429. doi: 10.1061/(ASCE)0733-9429(1987)113:9(1187).

[144] L. C. Van Rijn. Sediment transport part II: Suspended load transport. *Journal of Hydraulic Engineering*, 11:1613–1641, 1984.

[145] L. C. Van Rijn. pick-up functions.pdf. *Journal of Hydraulic engineering*, 110(10):1494–1502, 1984.

[146] L. C. van Rijn. Mathematical Modeling of Morphological Processes in the Case of Suspended Sediment transport, 1987.

[147] L. C. Van Rijn. The State of the Art in Sediment Transport Modeling, 1989.

[148] L. C. Van Rijn. *Principles of sediment transport in rivers, estuaries, and coastal seas.* Aqua publications, 1993.

[149] Leo C. van Rijn. Sediment Transport, Part III: Bed forms and Alluvial Roughness, 1984. ISSN 0733-9429.

[150] V. A. Vanoni. *Sedimentation Engineering.* ASCE Task Committee for the Preparation of the Manual on Sedimentation of the Sedimentation Committee of the Hydraulics Division Published, 1975. ISBN 0784408238.

[151] C. Villaret, J. M. Hervouet, R. Kopmann, U. Merkel, and A. G. Davies. Morphodynamic modeling using the Telemac finite-element system. *Computers and Geosciences*, 53:105–113, 2013. ISSN 00983004. doi: 10.1016/j.cageo.2011.10.004.

[152] M. Vinokur. On One-Dimensional Stretching Functions for Finite Difference Calculations. *Journal of Computational Physics*, 50(2):215–234, 1983. doi: 10.1016/0021-9991(83)90065-7.

[153] T. Von Kármán. The engineer grapples with nonlinear problems. *Bulletin of the American Mathematical Society*, 46(8):615–683, 1940. ISSN 02730979. doi: 10.1090/S0002-9904-1940-07266-0.

[154] D. J. R. Walstra, L. C. Van Rijn, and S. G. J. Aarninkhof. Sand Transport at the middle and lower shoreface of the Dutch coast: Simulations of SUTERNCH-model and proposal for large-scale laboratory tests. Technical report, Delft Hydraulics, 1998.

[155] R. D. Winn and R. H. Dott. Large-scale traction-produced structures in deep-water fan-channel conglomerates in southern Chile. *Geology*, 5(1):41–44, 1977. ISSN 00917613. doi: 10.1130/0091-7613(1977)5⟨41: LTSIDF⟩2.0.CO;2.

[156] W. Wu, W. Rodi, and T. Wenka. 3D Numerical modeling of flow and sediment transport in open channels. *Journal of Hydraulic Engineering*, 126, 2000.

[157] X. Xu, Y. S. Chang, H. Peters, T. M. Özgökmen, and E. P. Chassignet. Parameterization of gravity current entrainment for ocean circulation models using a high-order 3D nonhydrostatic spectral element model. *Ocean Modelling*, 14(1-2):19–44, 2006. ISSN 14635003. doi: 10.1016/j.ocemod.2006.02.006.

[158] M. S. Yalin. *Mechanics of sediment transport.* 2nd Ed., Pergamon, Oxford, UK, 1977.

[159] A. Yeganeh-Bakhtiary, M. H. Kazeminezhad, A. Etemad-Shahidi, J. H. Baas, and L. Cheng. Euler-Euler two-phase flow simulation of tunnel erosion beneath marine pipelines. *Applied Ocean Research*, 33(2):137–146, 2011. ISSN 01411187. doi: 10.1016/j.apor.2011.01.001.

[160] W. Yue, C. Lin, and V. C. Patel. Numerical simulation of unsteady multidimensional free surface motions by level set method. *International Journal for Numerical Methods in Fluids*, 42(8):853–884, 2003. ISSN 02712091. doi: 10.1002/fld.555.

[161] Y. Zang, R. L. Street, and J. R. Koseff. A Non-staggered Grid, Fractional Step Method for Time-Dependent Incompressible Navier-Stokes Equations in Curvilinear Coordinate. *Journal of Computanional Physics*, 114:18–33, 1944.

[162] G. Zanier, A. Petronio, and V. Armenio. The effect of Coriolis force on oil slick transport and spreading at sea. *Journal of Hydraulic Research*, 55(3):409422, 2017.

[163] U. C. E. Zanke. Berechnung der sinkgeschwindigkeiten von sedimenten. Technical report, Tech. Rep. 42, Mitteilungen des Franziusinstituts fur wasserbau, Technische Universitat Hannover, 1977.

[164] U. C. E. Zanke. On the influence of turbulence on the initiation of sediment motion. *International Journal of Sediment Research*, 18(1): 17–31, 2003. ISSN 10016279.

[165] J. Zordan, C. Juez, A. J Schleiss, and M. J Franca. Experimental Results on Sediment Entrainment By Gravity Currents. In *Proceedings of the 37th IAHR World Congress*, volume EPFL-CONF-, pages 1453–1458, 2017.